

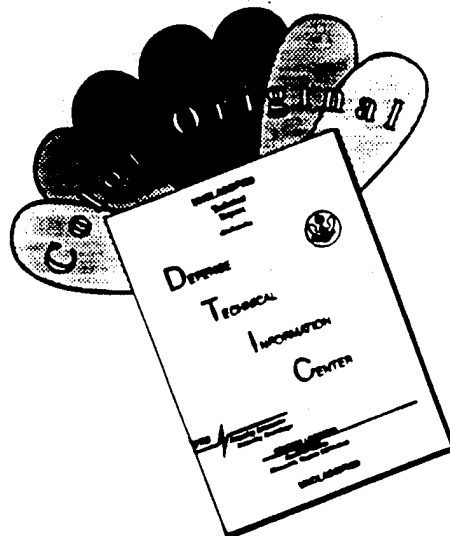
REPORT DOCUMENTATION PAGE

Form Approved
OMB No. 0704-0188

Public reporting burden for this collection of information is estimated to average 1 hour per response, including the time for reviewing instructions, searching existing data sources, gathering and maintaining the data needed, and completing and reviewing the collection of information. Send comments regarding this burden estimate or any other aspect of this collection of information, including suggestions for reducing this burden, to Washington Headquarters Services, Directorate for Information Operations and Reports, 1215 Jefferson Davis Highway, Suite 1204, Arlington, VA 22202-4302, and to the Office of Management and Budget, Paperwork Reduction Project (0704-0188), Washington, DC 20503.

1. AGENCY USE ONLY (Leave blank)	2. REPORT DATE	3. REPORT TYPE AND DATES COVERED
		JAN 96
4. TITLE AND SUBTITLE		5. FUNDING NUMBERS
6. AUTHOR(S) <i>Dave Pruitt</i>		95-1-0146 2307/45
7. PERFORMING ORGANIZATION NAME(S) AND ADDRESS(ES) <i>College of William & Mary</i>		AFOSR-TR-96 0155
9. SPONSORING/MONITORING AGENCY NAME(S) AND ADDRESS(ES) <i>Air Force Office Of Scientific Research Aerospace & Materials Sciences Directorate 110 Duncan Avenue, Suite B-115 Bolling AFB DC 20332-0001 Dr. Len Sakell</i>		NA
10. SPONSORING/MONITORING AGENCY REPORT NUMBER		
11. SUPPLEMENTARY NOTES		
12a. DISTRIBUTION/AVAILABILITY STATEMENT <i>APPROVED FOR PUBLIC RELEASE DISTRIBUTION IS UNLIMITED</i>		12b. DISTRIBUTION CODE <i>19960404 073</i>
13. ABSTRACT (Maximum 200 words) Specifically, progress to date has proceeded on three fronts, each of which expands existing DNS capabilities in the direction of "configuration DNS" stated in general objective 1 above. Previous experimental and numerical work on the elliptic-cone problem by others has shown that crossflow instabilities, rather than first- or second-mode instabilities, are likely to dominate the transition process when the eccentricity of the cross-sectional ellipse is moderate to large. Thus, the problem is particularly difficult for two reasons: 1) existing DNS capabilities must be expanded in terms of configuration (complex geometry), and 2) little or no experience exists in the simulation of crossflow instability for high-speed flows. Because of the difficulty of the problem, it was deemed best to proceed incrementally, from the current state of the art, along three fronts: 1) simulation of transition on a flared, axisymmetric cone in hypersonic flow, 2) simulation of crossflow instability on a supersonic swept wing, and 3) simulation of a transitional hypersonic flow on a cone with an elliptical		
14. SUBJECT TERMS <i>DNS, Transition</i>		15. NUMBER OF PAGES <i>68</i>
17. SECURITY CLASSIFICATION OF REPORT		18. SECURITY CLASSIFICATION OF THIS PAGE
19. SECURITY CLASSIFICATION OF ABSTRACT		20. LIMITATION OF ABSTRACT <i>Unclassified</i>

DISCLAIMER NOTICE



**THIS DOCUMENT IS BEST
QUALITY AVAILABLE. THE COPY
FURNISHED TO DTIC CONTAINED
A SIGNIFICANT NUMBER OF
COLOR PAGES WHICH DO NOT
REPRODUCE LEGIBLY ON BLACK
AND WHITE MICROFICHE.**

15 January 1996

Department of Mathematics
James Madison University
Harrisonburg, VA 22807
(540) 568-6227 dpruett@math.jmu.edu

Dr. Leonidas Sakell
AFOSR/NA
110 Duncan Avenue, Suite B-115
Bolling AFB DC 20332-0001

Dear Len,

Please find enclosed three copies of the final report for AFOSR Grant F49620-95-1-0146 entitled "Spatial Direct Numerical Simulation of Transition in Hypersonic Flows."

The sections on the supersonic swept wing and elliptic cone have not changed appreciably since the interim report was issued in September 95. However, the discussion regarding the first-year objective to simulate transition on a flared cone has changed substantially to reflect the completion and documentation of this work. The results are quite interesting in that there are obvious qualitative differences between the straight-cone (Pruett and Chang, 1995) and flared-cone cases.

I have a question as to the status of my account on WES at the termination of the grant period. It is my hope that I could maintain access to the data for some months; I believe that the flared-cone results are sufficiently novel to warrant publication. Also, should the work continue under a grant to High Technology Corporation, the current data should be made available to them.

It has been a pleasure to work with you. Best wishes and please stay in touch.

Sincerely yours,

Dave Pruett
Dave Pruett
Jan 6 a

Final Report for AFOSR Grant F49620-95-1-0146

Spatial Direct Numerical Simulation of Transition in Hypersonic Flows

Principal Investigator: Dr. C. David Pruett

PRESENT ADDRESS
Dept. of Applied Science
The College of William and Mary
Williamsburg, VA 23187-8795
(804) 221-1755
dpruett@woksape.appsci2.wm.edu

FUTURE ADDRESS-EFFECTIVE JAN. 1996 ✓

Department of Mathematics
James Madison University
Harrisonburg, VA 22801
(540) 568-6227
dpruett@math.jmu.edu

Grant Period: 1 Feb. 1995 through 31 Jan. 1996

Progress Report for AFOSR Grant F49620-95-1-0146

Spatial Direct Numerical Simulation of Transition in Hypersonic Flows

Principal Investigator: Dr. C. David Pruett
Dept. of Applied Science
The College of William and Mary

Grant Period: 1 Feb. 1995 through 31 Jan. 1996

1 Objectives

The general objectives of this effort, originally envisioned as a three-year project, are the following:

1. To advance the state-of-the-art of direct numerical simulation (DNS) toward the ultimate goal of configuration DNS.
2. To study the physics of transition in hypersonic wall-bounded flows. In particular, to identify likely instability modes and paths to transition and to assess the effects on transition of adverse pressure gradient, wall cooling, and body asymmetry.
3. To develop a transitional-flow data base for hypersonic flows that can be used 1) to extract transition physics through postprocessing and computational flow imaging (CFI) and 2) to develop and refine transition models (not part of this effort).
4. To begin development of a configuration large-eddy simulation (LES) capability for high-speed transitional flows with benchmark DNS calculations against which future LES data can be compared. (LES work *per se* not currently part of this effort.)

It was proposed that these general objectives be met by considering two specific test problems.

1. In the first year, the laminar-turbulent transition of the boundary layer along an axisymmetric flared-cone in Mach 6 flow was considered. The intent was to study the

effects on transition of concave surface curvature and adverse streamwise pressure gradient.

2. The specific goal for the two follow-on years was to simulate a transitional hypersonic boundary-layer flow along on a cone with an elliptical cross-section at zero angle of attack. Such a configuration is of particular interest because it represents the prototype forebody for future hypersonic flight vehicles (e.g., the National Aerospace Plane (NASP)).

2 Status of Project

The specific first-year objective was met and significant progress was made toward the specific and general objectives intended for the second and third years of the project.

Specifically, progress to date has proceeded on three fronts, each of which expands existing DNS capabilities in the direction of "configuration DNS" stated in general objective 1 above. Previous experimental and numerical work on the elliptic-cone problem by others has shown that crossflow instabilities, rather than first- or second-mode instabilities, are likely to dominate the transition process when the eccentricity of the cross-sectional ellipse is moderate to large. Thus, the problem is particularly difficult for two reasons: 1) existing DNS capabilities must be expanded in terms of configuration (complex geometry), and 2) little or no experience exists in the simulation of crossflow instability for high-speed flows. Because of the difficulty of the problem, it was deemed best to proceed incrementally, from the current state of the art, along three fronts: 1) simulation of transition on a flared, axisymmetric cone in hypersonic flow, 2) simulation of crossflow instability on a supersonic swept wing, and 3) simulation of a transitional hypersonic flow on a cone with an elliptical cross section. Simulation 1) was completed and is thoroughly documented below. Problem 2) was addressed, is largely completed, and is also documented thoroughly. Problem 3) remains in the formative stages, but important groundwork was laid. The specific accomplishments for each of these problems are discussed below.

3 Accomplishments

3.1 DNS of Instability and Transition on a Flared Cone

INTRODUCTION: The computation documented in the recent papers of Pruett et al. [15] (Attachment 1), Pruett and Chang [16], and Pruett and Zang [17], represents the first attempt to numerically simulate the transition of a high-speed boundary-layer flow for Reynolds numbers and configurations of engineering interest. Specifically, their work examined the

laminar breakdown of a Mach 8 boundary-layer flow on an axisymmetric sharp cone in the absence of streamwise pressure gradient. The computation approximately simulated the sharp-cone experiment of Stetson et al. [21] and was motivated by the hope that, when experiment and computation are both brought to bear on the same physical problem, the results will be more enlightening than when either approach alone is used. In the present paper, we extend the capability for “configuration DNS” to a flared-cone configuration.

Recently, Wilkinson and Anders [24], Lachowicz et al. [9], and Kimmel [8] have each conducted hypersonic wind-tunnel experiments on axisymmetric flared-cone models to assess the direct and indirect effects on transition of streamwise surface curvature. We consider here only the case of concave curvature. A concave flare induces several effects: an adverse (positive) streamwise pressure gradient, a decrease in mean edge Mach number, an increase in mean wall temperature, a reversal of boundary-layer growth, and Goertler instability. The conventional wisdom, based largely on experience with low-speed flows, is that the adverse streamwise pressure gradient should promote more rapid transition than for a configuration without a flare. The results of Kimmel [8] are inconclusive, however. In high-speed boundary layers, the transition zone can be quite long, due to the generally stabilizing influence of increasing Mach number. Whereas adverse pressure gradient appears to accelerate transition onset, in some cases the transition zone was observed to lengthen relative to the zero pressure gradient case. Apparently, at high speeds, there is interplay among subtle effects, several of which were mentioned above. For example, possible interaction/competition between second-mode [12] and Goertler instabilities may occur, the latter of which are linearly stable for cones at zero angle of attack without flare. Moreover, variations in edge Mach number and wall temperature may tend to select or deselect certain modes of instability in different regions of the transition zone. A further subtlety concerns the level of freestream turbulence and the issue of boundary-layer receptivity, which is beyond the scope of the current investigation. However, one should keep in mind that, whereas the experiment of Lachowicz et al. [9] was conducted in a low-turbulence “quiet” facility, the experiments of Kimmel [8] were conducted in a conventional facility with a relatively high level of freestream turbulence. Suffice it to say, transitional high-speed flows remain poorly understood, and further experiment and computation are warranted.

In the present work, we adapt the approach and algorithm of Pruett et al. [15] to simulate the early stages of laminar-turbulent transition on an axisymmetric flared cone in Mach 6 flow. Our motivations are to advance the state-of-the-art in configuration DNS and to study the subtle transition phenomena associated with surface curvature mentioned above. Consequently, the effects of streamwise surface curvature, mean streamwise pressure gradient, and varying boundary-layer edge conditions are incorporated into the governing equations and boundary conditions. A DNS test case has been designed based on the configuration and flow conditions of the experimental investigation of Lachowicz et al. [9]. This choice of test case affords the additional opportunity to draw upon the theoretical investigation by Balakumar and Malik [1], who conducted N-factor studies for the flared-cone geometry of the Lachowicz et al. experiment.

In the next sections, we discuss the governing equations, present the test case, summarize the numerical methodology, present results, and draw some conclusions, respectively.

GOVERNING EQUATIONS: Let p , ρ , T , μ , and κ denote the pressure, density, temperature, viscosity, and thermal conductivity of a compressible fluid, respectively. We assume that the flow of a compressible fluid is exactly governed by the compressible Navier-Stokes equations (CNSE), which can be found in many references on fluid mechanics. If we restrict attention to axisymmetric bodies and define x as the surface arc length, θ as the azimuthal angle, and z as the coordinate normal to the wall, then in body-fitted coordinates, the CNSE assume the form given in Pruett et al. [15], where u , v , and w denote the velocity components in the principal coordinate directions, respectively. We note that the equations given in Pruett et al. include both transverse and streamwise curvature terms and incorporate the notation $R(x)$ and $\phi(x)$ to denote the body radius and the angle of the surface tangent relative to the axis, respectively, as functions of arc length. Four dimensionless parameters arise from nondimensionalization of the governing equations: Mach number M , Reynolds number Re , Prandtl number Pr , and the ratio of specific heats, γ . Throughout this work, the Pr and γ are assumed to be constants with values of 0.72 and 1.4, respectively. Finally, the dependency of viscosity μ on temperature is modeled by Sutherland's law, and $\kappa = \mu/Pr$.

TEST CASE: The experiment of Lachowicz et al. [9], on which the numerical computation is based, examines Mach 6 flow on a 20-inch-long flared-cone model at zero angle of attack. The model consists of a 5-degree half-angle axisymmetric sharp cone blended to an afterbody with a circular-arc flare beginning 10 axial inches from the apex. The radius of curvature of the flare is constant and equal to 93.07 inches; a curvature discontinuity exists at the flare interface. The nominal pre-shock freestream conditions are

$$\begin{aligned} M_\infty &= 6.0 \\ T_\infty^* &= 98.78^\circ R \\ (T_t^* &= 810.0^\circ R) \\ p_\infty^* &= 11.86 \text{ psf} \\ (p_t^* &= 18,720 \text{ psf}) \\ Re_1^* &= 2,728,087 \text{ ft}^{-1} \end{aligned} \tag{1}$$

where Re_1 is the freestream unit Reynolds number. Throughout this work, asterisks denote dimensional quantities, and subscripts ∞ , t , and e denote freestream, total, and boundary-layer edge conditions, respectively.

A precise thermal boundary condition at the model surface cannot be ascertained on the basis of information reported about the experiment. Run times were long, and it is believed that the wall behaved approximately adiabatically under equilibrium conditions. However, the model was thin-skinned and uninsulated, and mounting hardware prevented the attainment of thermal equilibrium near the models' base. Given the uncertainty as to the experimental thermal condition and the fact that we consider only the early stages of transition for the DNS, we have adopted the boundary condition of Pruett and Chang [16].

The use of this thermal condition is advantageous in that it allows comparison of simulated flared-cone and straight-cone results for the same boundary conditions. The boundary conditions will be specified precisely later.

METHODOLOGY: Roughly speaking, spatial DNS is a three-step process. A laminar and steady base state is defined, whose stability is to be investigated. The base state is subject to time-dependent fluctuations at or near the computational inflow boundary, and the spatial evolution of these disturbances is calculated by solution of the three-dimensional and unsteady CNSE. The temporally and spatially evolving numerical solution is sampled and stored periodically in time for the subsequent postprocessing and analysis that constitute the final step. We address each of these steps in turn.

To obtain the laminar base state for their stability calculations, Balakumar and Malik [1] computed the flow over the flared-cone configuration by both Euler and Navier-Stokes techniques. The Navier-Stokes solution was sensitive to the choice of limiter (dissipation) and required very high resolution within the wall layer to provide accurate first and second wall-normal derivatives, which were needed for their linear-stability analysis. They found that the pressure distributions computed by the two methods agreed very well except near the tip of the cone. Moreover, N-factors computed by the two methods agreed to within approximately ten percent. Because the difference in N-factors was small, in the final analysis, for computational efficiency, they recommended an Euler/boundary-layer approach over the solution of the full CNSE.

For the present work, we also favor a boundary-layer equation approach. Specifically, we exploit the spectrally accurate boundary-layer code of Pruett and Streett [13] with the modification for varying edge conditions proposed by Pruett [14]. The post-shock edge pressure distribution $p_e^*(x^*)$ needed by the boundary-layer code is obtained from the Navier-Stokes solution of Balakumar and Malik [1]. In the vicinity of the tip (a region excluded in the DNS calculation), the pressure distribution is modified by extrapolating linearly from downstream values. For self consistency, all other boundary-layer edge conditions are inferred from the pressure, based on the assumption of isentropic post-shock flow. Although this assumption is not strictly valid in the flared region, the shock is highly oblique and weak, and errors committed by assuming isentropic post-shock flow are small. Figure 1 presents the radius R^* of the cone as a function of surface arc length x^* . The edge Mach number, edge temperature, and edge pressure distributions are also provided as functions of x^* . Note that the edge Mach number decreases almost linearly from nearly 5.6 at the beginning of the flare to 4.9 at the end of the model. In contrast, edge pressure and temperature both increase significantly and nearly linearly in the flare region. The evolution of the laminar boundary-layer displacement thickness δ_1 is shown in Fig. 2. Note the reversal of the normal thickening of the boundary layer in the flare region. Typical temperature and streamwise velocity profiles for an adiabatic wall are shown in Fig. 3. The profiles correspond to axial station 1.1725 ft. in the flare region. Note that the velocity distribution is nearly linear across the boundary layer, a characteristic of high-speed flow, and that, because of frictional heating, the wall temperature is nearly six times that at the boundary layer edge.

The boundary-layer solution is interpolated onto a DNS grid using a spectrally accurate interpolation code, which extrapolates outside the boundary-layer region by solving the continuity equation exactly in the asymptotic limit as $z \rightarrow \infty$. The asymptotic outer solution is matched to the inner solution at the boundary-layer edge. Special attention is paid to accurately computing the wall-normal velocity, for which we use the method of Pruett [14]. A typical wall-normal velocity distribution versus z is shown in Fig. 4. For axisymmetric cones, the wall-normal velocity is negative, which implies that the far-field computational boundary should be treated as an inflow boundary.

The special care used to match inner and outer solutions consistently is necessary to prevent discontinuities in higher derivatives of the basic state, which would contaminate the subsequent stability analysis. As a consistency check, we typically compute the residuals of the time-independent and dimensionless CNSE by using the interpolated boundary-layer solution as an initial state. Residuals that are quite small, say of order 10^{-4} , as shown in Fig. 5, indicate that the boundary-layer solution closely approximates the exact solution. Because the residuals reflect the sum of approximation errors, interpolation errors, numerical errors, and blunders, small residual errors provide a stringent test of self-consistency among the various numerical tools exploited by DNS. Indeed, on several occasions we have uncovered and corrected algorithmic bugs simply by examining the steady-state residuals.

For the DNS calculation, we adapt the techniques of Pruett et al. [15]. Their fully explicit collocation scheme exploits the third-order low-storage Runge-Kutta scheme of Williamson [25] for time advancement and both spectral and central compact-difference methods for spatial discretization. Specifically, spectral-collocation methods are used in the azimuthal direction, in which the flow is periodic, whereas the high-order compact-difference methods of Lele [10] are exploited in the aperiodic streamwise and wall-normal directions. Modest filtering is used to correct the innate tendency of central-difference approximations toward odd-even decoupling of the solution in the far field whenever resolution is marginal. Filtering also alleviates numerical reflections at the outflow boundary. A discussion of the necessity for and implementation of filtering can be found in Pruett et al. [15]. With regard to the spectral-collocation scheme used in the azimuthal direction, we implement dealiasing according to the 1/2-rule to suppress high-frequency oscillations that could lead to numerical instability.

Minor modifications to the scheme of Pruett et al. are necessitated by particulars of the current flared-cone problem. Because boundary-layer edge conditions vary for the current problem, flow quantities are nondimensionalized by the pre-shock freestream temperature, velocity, and density, etc., given or implied in Eq. 1. Previously, flow quantities were scaled by appropriate post-shock values at the boundary-layer edge, which were presumed constant along the axisymmetric cone without flare. For both the work of Pruett et al. and the current work, lengths are scaled by the boundary-layer displacement thickness δ_1^* at the computational inflow boundary x_{in} . Previously, $R(x)$ was computed internally and $\phi(x)$ was constant; for the present problem, both quantities are computed externally by the boundary-layer code and read as input to the DNS algorithm. As was done in Pruett et al., grid

spacing is uniform in the x direction, and, in the wall-normal direction, grid points are tightly clustered near the wall and near the critical layer. For the present problem, the DNS computation includes only a region of flow aft of the flare, where the boundary-layer thickness diminishes (Refer to Fig. 2). This is in contrast to the growing boundary layer along the cone without flare. In either case, to account for the variation in boundary-layer thickness, we exploit a mapping of the form

$$z = \eta f(x) \quad (2)$$

However, for the present problem, the mapping function is linear and is given by

$$f(x) = 1 - .05 \frac{x - x_{\text{out}}}{x_{\text{in}} - x_{\text{out}}} \quad (3)$$

where x_{out} is the coordinate of the computational outflow boundary.

The boundary conditions for the present problem are taken without modification from Pruett et al. [15]. In brief, all flow variables are specified along the inflow boundary, a buffer domain approach (Streett and Macaraeg [22]) is exploited at the outflow boundary, and Thompson [23] conditions are adapted along the far-field boundary $\eta = \eta_{\text{max}}$. At the wall, all velocity components vanish; the thermal boundary condition may be either adiabatic or isothermal. As mentioned previously, to facilitate comparison with the straight-cone results of Pruett and Chang [16], we adopt their hybrid thermal boundary condition whereby wall temperature is held fixed at its laminar adiabatic-wall value. Density at the wall is computed directly from the governing equations.

PRIMARY INSTABILITY: The hot-wire data of Lachowicz et al. [9] were examined to identify unstable disturbances. These data show that the most unstable frequency F^* downstream of the flare is in the range 218-228 kHz, in close agreement with the 230kHz predicted by Balakumar and Malik [1] on the basis N-factor studies. Unfortunately, the signal-to-noise levels of the data of Lachowicz et al. are too low in the region ahead of the flare to provide useful information there. Neither was information available in regard to the obliqueness angle of the primary instability. For this work, additional information was needed to identify a transition mechanism. Consequently, a parameter study was conducted by Chang [6] on the basis of nonlinear parabolized stability equation (PSE) methodology to identify a likely transition scenario. Chang considered primary disturbances with temporal circular frequencies $\omega^* = 2\pi F^*$ close to those observed or predicted in the investigations of [9] or [1]. The study confirmed, as anticipated, that Goertler modes of instability are linearly unstable for a broad range of azimuthal wavenumbers β^* . In contrast, Goertler modes (which have zero temporal frequency) are linearly stable for the cone without flare and gain energy only through nonlinear interactions. For $F^* = 230$ kHz, a fundamental azimuthal wavenumber given by $n = \beta^* R^* = 15$ was shown to lead to highly unstable disturbances. (Note that because of periodicity in the azimuthal direction, n must be an integer.) A transition scenario was constructed based on a disturbance consisting initially of three fundamental components whose nonlinear interactions lead to a transitional state. Subsequently, we refer to the fundamental components and their harmonics by integer pairs

(l,m) , where the integers l and m identify the harmonic with respect to the fundamental values of temporal frequency ω and azimuthal wavenumber β , respectively.

The amplitudes of selected harmonics from the PSE calculation are shown in Fig. 6. The PSE computation spanned the region $x^* = 0.58$ ft., ahead of the flare, to $x^* = 1.4$ ft. in the flared zone. At the inflow boundary, the calculation was initialized with a disturbance triad comprised of Fourier components $(1,0)$, $(1,1)$, and $(1,-1)$ (not shown). The $(1,0)$ component represents an axisymmetric disturbance, whereas the $(1,1)$ and $(1,-1)$ components represent symmetric oblique (helical) disturbances. All other harmonics emerged spontaneously from the nonlinear interactions among the fundamental triad. Fig. 6 shows saturation of the fundamental components of the disturbance near $x^* = 1.0$ ft. occurring simultaneously with significant distortion of the mean flow $(0,0)$ and rapid growth of higher harmonics to significant amplitudes. These conditions indicate that the flow is transitioning from a laminar to a turbulent state.

RESULTS: The computational domain of the DNS encompassed a section along the body downstream of the beginning of the flare. Specifically, the computational domain spanned the region

$$\begin{aligned} x_{\text{in}}^* &= 0.9 \leq x^* \leq 1.2 = x_{\text{out}}^* \text{ ft.} \\ 0 \leq \theta &\leq \frac{2\pi}{n} \quad (n = 15) \\ 0 \leq \eta &\leq 7.5 \end{aligned} \tag{4}$$

The time-periodic inflow condition at $x_{\text{in}}^* = 0.9$ was derived from the PSE results at the corresponding station. At this station, the fundamental $(1,0)$ component of the disturbance had attained a large (nonlinear) amplitude, and numerous harmonics of the disturbance showed significant amplitudes. All significant harmonics were incorporated into the DNS inflow condition. Relative to the wavelength of the fundamental components of the disturbance, the computational domain encompassed approximately 26 wavelengths in streamwise extent. The resolution of the computational grid was $2304 \times 18 \times 128$ in the streamwise, azimuthal, and wall-normal directions, respectively. At this streamwise grid density, each fundamental wavelength was resolved by approximately 90 grid points, sufficient, according to Pruett et al. [15], to resolve at least the first six streamwise harmonics. The azimuthal resolution, significantly less than that of Pruett et al., was sufficient only for the initial stages of laminar breakdown, and was dictated largely by available computational resources. Consequently, the simulation was halted prior to end-stage transition.

The DNS computation was performed on the Waterways Experiment Station (WES) Cray C90 at Vicksburg, MS. Approximately 250 hours of single processor time and 115 megawords of main memory were required for the computation. The code is optimized to run in parallel, and during the production runs, we typically requested three CPUs. In physical terms, the computation proceeded for approximately 30 periods of oscillation at the fundamental frequency. The dominant instability waves were observed to propagate downstream at approximately 90 percent of the boundary-layer edge velocity; consequently,

the physical computation time was approximately that necessary for the fundamental instability wave to complete one traverse of the computational domain.

During the computation, the numerical solution was periodically written to output and archived at a rate of 64 samples per period of the fundamental frequency. These data were later postprocessed to extract quantitative and qualitative information about the evolution of the flow. Most of the results to follow were obtained by Fourier time-series analysis of the final period (29-30) of the computation.

Figure 7, obtained by Fourier transforms in the periodic temporal and azimuthal dimensions, displays the streamwise evolution of the amplitudes of selected harmonics of the DNS calculation. The corresponding PSE results are also provided for comparison. Several important observations can be made. First, the DNS and PSE results agree well for approximately the first third of the computational domain of the DNS. Downstream of the first third of the domain, the DNS and PSE results gradually diverge, but the methods continue to indicate agreement in the qualitative behavior of the selected harmonics. Downstream of $x^* = 1.15$ ft., some vestige of the initially undisturbed laminar state remains; here the DNS results cannot be considered fully developed and should be disregarded.

Figure 8 displays the streamwise evolution of various mean quantities computed by averaging both temporally and spatially over the azimuthal coordinate. For comparison, the corresponding quantities are shown also for the undisturbed initial laminar state. Clear indications of transitioning flow are evident: principally a dramatic drop in the shape factor $H = \delta_1^*/\delta_2^*$ below its laminar value. We note that the laminar shape factor, which is nearly constant for the cone without flare (Pruett and Zang [17]), diminishes with x in the flared region for the present configuration because of the decrease in Mach number. At this stage of the transition process, the decrease in H is due almost entirely to an increase in momentum thickness δ_2^* rather than to a decrease in displacement thickness δ_1^* . Near the end of the computational domain, the skin-friction coefficient C_f has increased approximately 25 percent over its laminar value, where

$$\begin{aligned} C_f &= \frac{2\tau_{\text{wall}}}{\rho_e^* u_e^{*2}} \\ \tau_{\text{wall}} &= \bar{\mu} \frac{\partial \bar{u}}{\partial z} \Big|_{z=0} \end{aligned} \quad (5)$$

However, at the same station, the coefficient C_h of thermal stress at the wall has more than doubled. Taken together, the plots for C_f and C_h call attention to an ambiguity in defining the location x_{tr}^* of transition onset for high-speed flows. On the basis of minimum wall shear, $x_{tr}^* = 0.95$ ft. On the basis of minimum heat transfer, transition onset apparently occurs upstream of the computational inflow boundary.

An overall impression is that, relative to the straight-cone case, transition on the flared cone, as indicated by skin-friction and heat transfer, begins earlier and proceeds more gradually. The reason for this qualitative behavior may have to do with the linear instability of Goertler modes for the flared-cone problem. These modes manifest significant velocities near

the wall, and because of their linear instability, they grow to significant amplitudes early in the transition process. As a result, mean skin friction is also affected relatively early. In contrast, for the straight cone, the disturbances tend to “live” far from the wall near the critical layer. Disturbance activity spreads toward the wall only through strongly nonlinear effects, which occur much later in the transition process. This observation of early transition onset but gradual transition for the cone with concave flare is not inconsistent with the experimental results of Kimmel [8]. However, because different researchers use different measures of transition onset, it is difficult to draw definitive comparisons between computation and experiment. In our judgement, the transition community would benefit by consensus in the definition of transition onset for high-speed boundary-layer flows.

Figure 9 presents the streamwise evolution of the principal components of the Reynolds stress tensor, namely $\overline{\rho u' u'}$, $\overline{\rho v' v'}$, and $\overline{\rho w' w'}$, where overlines denote temporal and azimuthal averages and primes denote fluctuations about the mean states. Dramatic differences relative to the results of Pruett and Chang [16] and Pruett and Zang [17] are immediately obvious. First, whereas for the cone without flare, the Reynolds stresses are dominated by the streamwise component, along the flared cone the streamwise and wall-normal stresses are of nearly equal magnitudes. Second, the dominant Reynolds stresses show profiles which peak quite close to the wall, in contrast to the peaks that occur about a displacement thickness from the wall in Pruett and Chang [16]. Similar trends are observed in turbulent Mach number M_t and (density-weighted) turbulent kinetic energy $\overline{\rho} K$ as shown in Fig. 10, each of which peaks close to the wall for the flared-cone case. (Turbulent kinetic energy is defined as one-half the trace of the Reynolds stress tensor.)

The differences noted above between the flared-cone and straight-cone cases may be due to a combination of effects manifest in other quantities. Figure 10 also displays the streamwise evolution of the root-mean-square density fluctuation. For the flared cone, the density fluctuation is very large at the wall, nearly 30 percent of the reference density. For the case of the cone without flare, the density fluctuations are non-zero but relatively small at the wall. Both configurations show peaks near the critical layer (about one displacement thickness from the wall). We speculate that the large density fluctuation near the wall is directly related to the significant streamwise pressure gradient of the flared-cone problem and its associated in wall-temperature gradient (Fig. 12). As shown in Fig. 11, most harmonics of the disturbance manifest significant velocity fluctuations in close proximity to the wall, in contrast to the usual character of second-mode disturbances. The combination of large density fluctuations and significant velocity fluctuations near the wall probably accounts for the trends observed above for Reynolds stress and (density-weighted) turbulent kinetic energy.

In addition to displaying the structure (amplitude envelope) of the velocity and temperature components of selected harmonics, Figures 11 and 13 also present a comparison of DNS and PSE results. The comparison is made at $x^* = 1.05$ ft., the midpoint of the computational domain of the DNS. In contrast to the previous close agreement between DNS and PSE obtained by Pruett et al. [15] and Pruett and Chang [16], the agreement between

methods can only be considered good in a qualitative sense for the flared cone, except for the fundamental (1,0) component, for which the agreement is relatively good. The discrepancy comes as a surprise, and, at the present, we do not know the cause.

Finally, we note that Lachowicz et al. [9] observes “second-mode” waves at the edge of the boundary layer in schlieren images made during his flared-cone experiment. Similar structures have been observed in hypersonic boundary-layer flows by several other experimentalists and have been referred to previously as “rope-like” waves. See, for example, the excellent review by Smith [20]. Computational flow imaging (CFI) of the present numerical experiment also clearly reveals instability waves of rope-like appearance (Fig. 14). To crudely approximate the physics involved in schlieren imagery, the instantaneous wall-normal density gradient has been averaged over the azimuthal coordinate and projected as a two-dimensional image in greyscale. The numerically derived image is qualitatively similar in appearance to the actual schlieren image obtained by Lachowicz et al. [9]. In particular, the wavelength of the instability is approximately two boundary-layer displacement thicknesses, in keeping with the nature of second-mode disturbances.

CONCLUSIONS: The early stages of laminar-turbulent transition on a flared cone in Mach 6 flow have been investigated by nonlinear PSE and spatial DNS techniques. For the computations, the full effects of streamwise surface curvature have been taken into account. These include adverse streamwise pressure gradient, decreased edge Mach number, a reversal of boundary-layer growth, and increased wall temperature.

Physical experiments, N-factor studies based on compressible linear stability theory, nonlinear PSE methodology, and DNS all confirm that disturbances of very high frequency (on the order of 230 kHz), are responsible for transition from a laminar to a turbulent state for the flared-cone configuration under study. Disturbances in this frequency range are classified as “second-mode” disturbances in the nomenclature of Mack [12]. A further indication that the primary disturbances are of second-mode type is the appearance of so-called “rope-like” waves in schlieren images from the physical experiment or in schlieren-like images from the numerical experiment. These disturbances manifest a wavelength that is approximately twice the boundary-layer displacement thickness, in keeping with the high-frequency nature of second-mode disturbances.

The results obtained by nonlinear PSE and DNS methodologies show significant quantitative disagreement as the flow evolves spatially from identical upstream initial states. Qualitative agreement in the growth rates and structures of harmonics persists quite far downstream. Despite these quantitative differences, the transition mechanism identified as viable by PSE methodology is confirmed by DNS to lead to a transitional state. The transitional state is triggered by the interaction of a triad of fundamental disturbance components whose nonlinear interactions generate all possible harmonics in (l,m) wavenumber space, where integers l and m refer to the harmonic with respect to the fundamental temporal frequency and azimuthal wavenumber, respectively. The transitional state is characterized by a decrease in the boundary-layer shape factor relative to its laminar value and increases in both skin friction and thermal stress at the wall.

The results of the present numerical flared-cone experiment differ dramatically from those of Pruett and Chang [16], who simulated laminar breakdown on a right circular cone without a flared afterbody. In particular, for the present configuration, the dominant Reynolds stress components, turbulent kinetic energy, and turbulent Mach number all manifest large values close to the wall, rather than near the critical layer as observed previously. Moreover, very large density fluctuations occur both at the wall and near the critical layer for the present configuration. For the present problem, Goertler modes of instability (i.e., harmonics of zero frequency of the form $(0,m)$) are linearly unstable. These harmonics manifest significant structure near the wall and result in earlier transition onset than is observed on the straight cone, if transition onset is defined on the basis of skin friction or thermal stress at the wall.

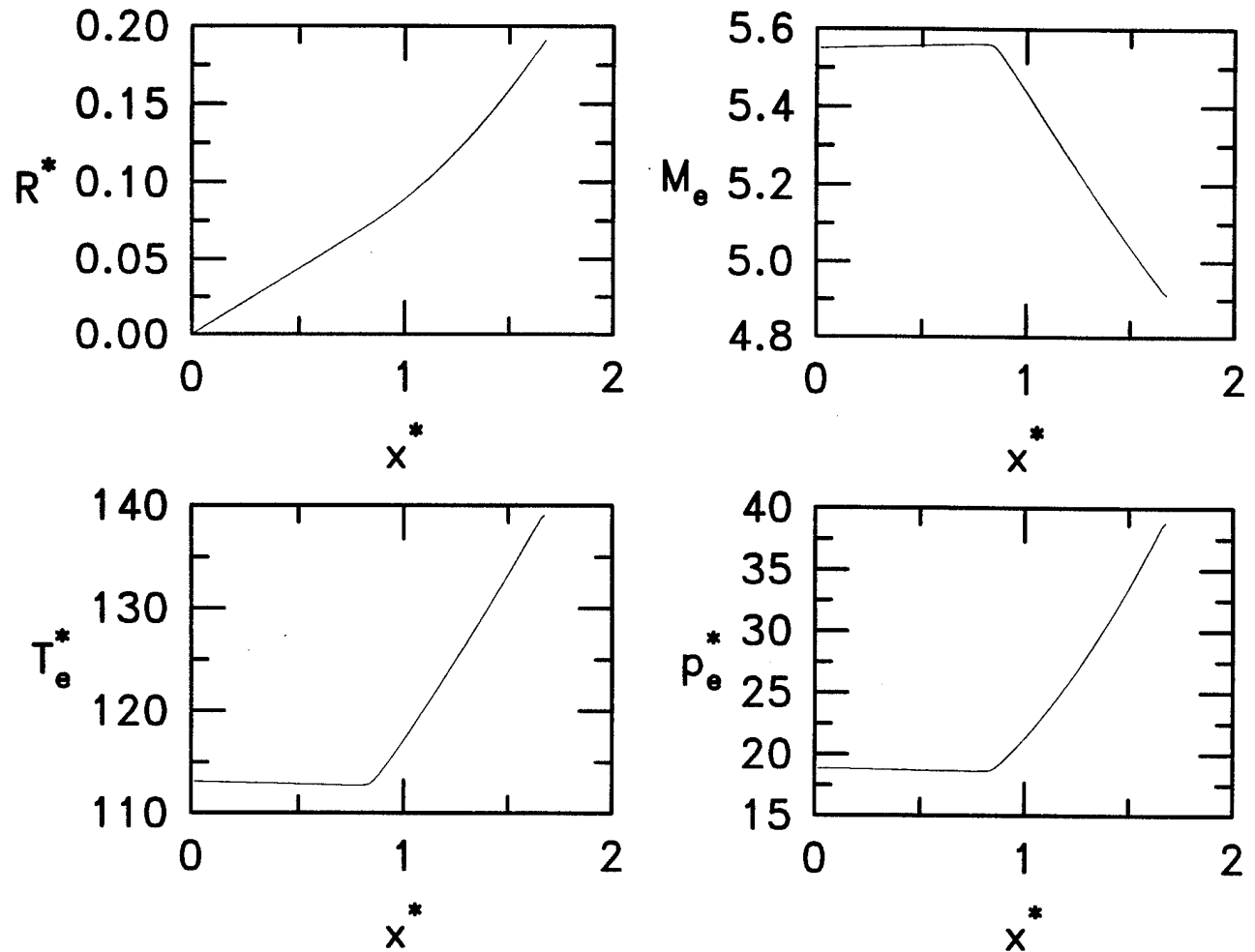


Figure 1: Radius and boundary-layer edge conditions versus surface arc length x^* for flared-cone model.

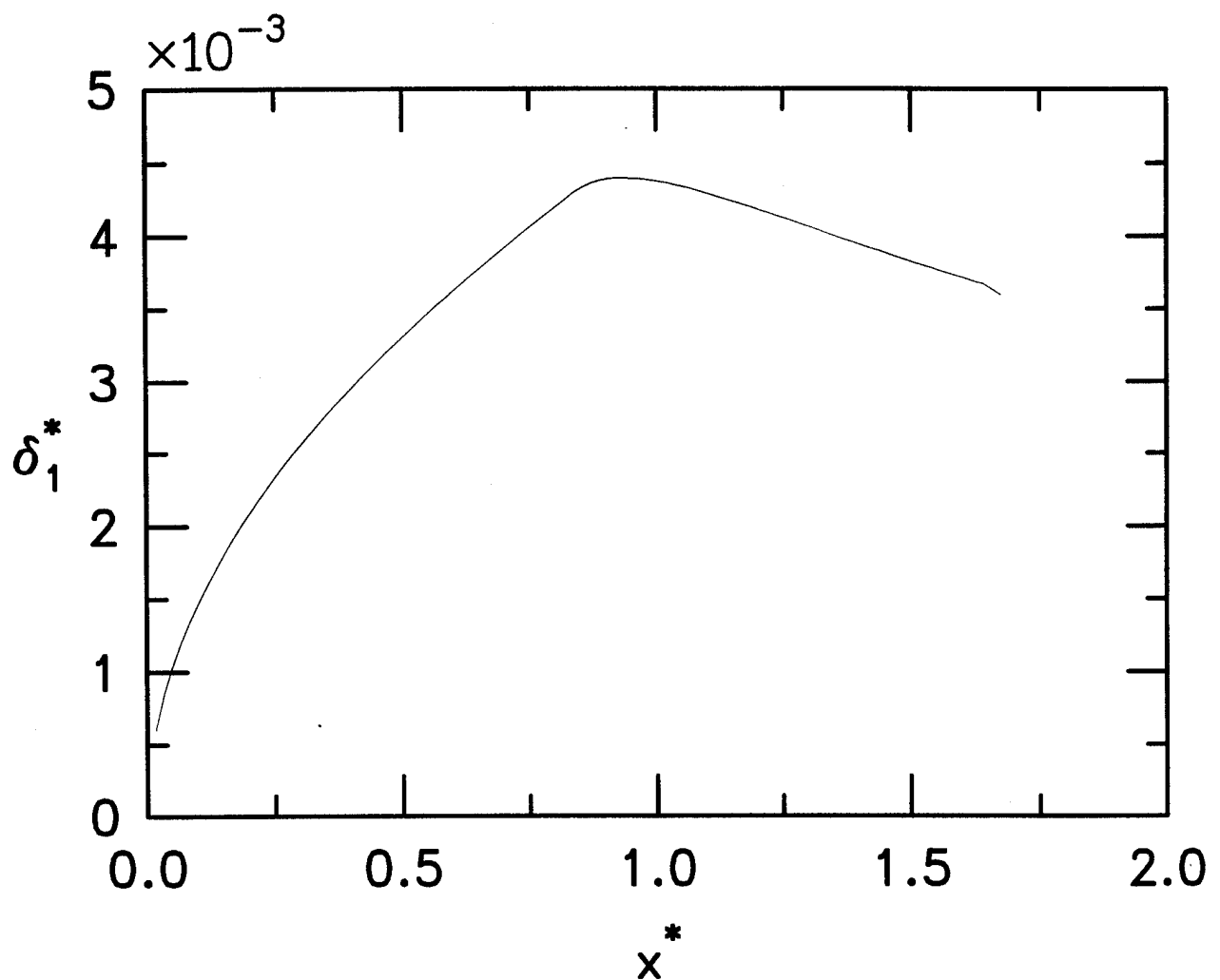


Figure 2: Boundary-layer displacement thickness versus surface arc length for flared-cone model. Boundary-layer growth reverses at body flare.

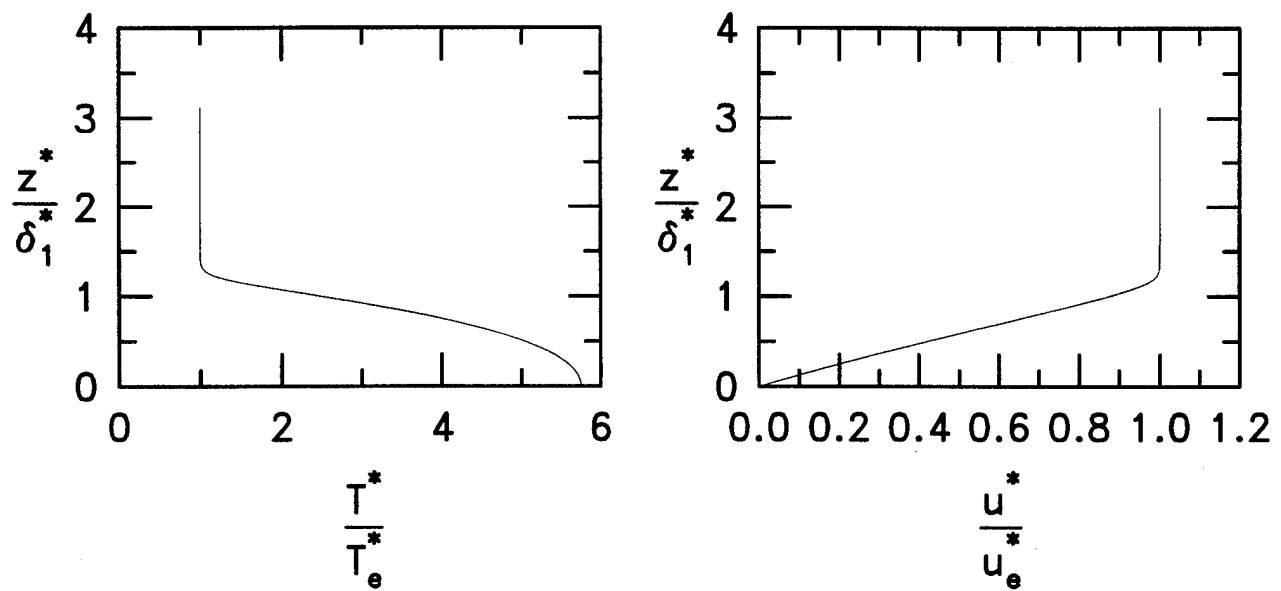


Figure 3: Normalized temperature and streamwise velocity distributions versus wall-normal coordinate z at axial station $x^* = 1.1725$ ft.

Wall-Normal Velocity

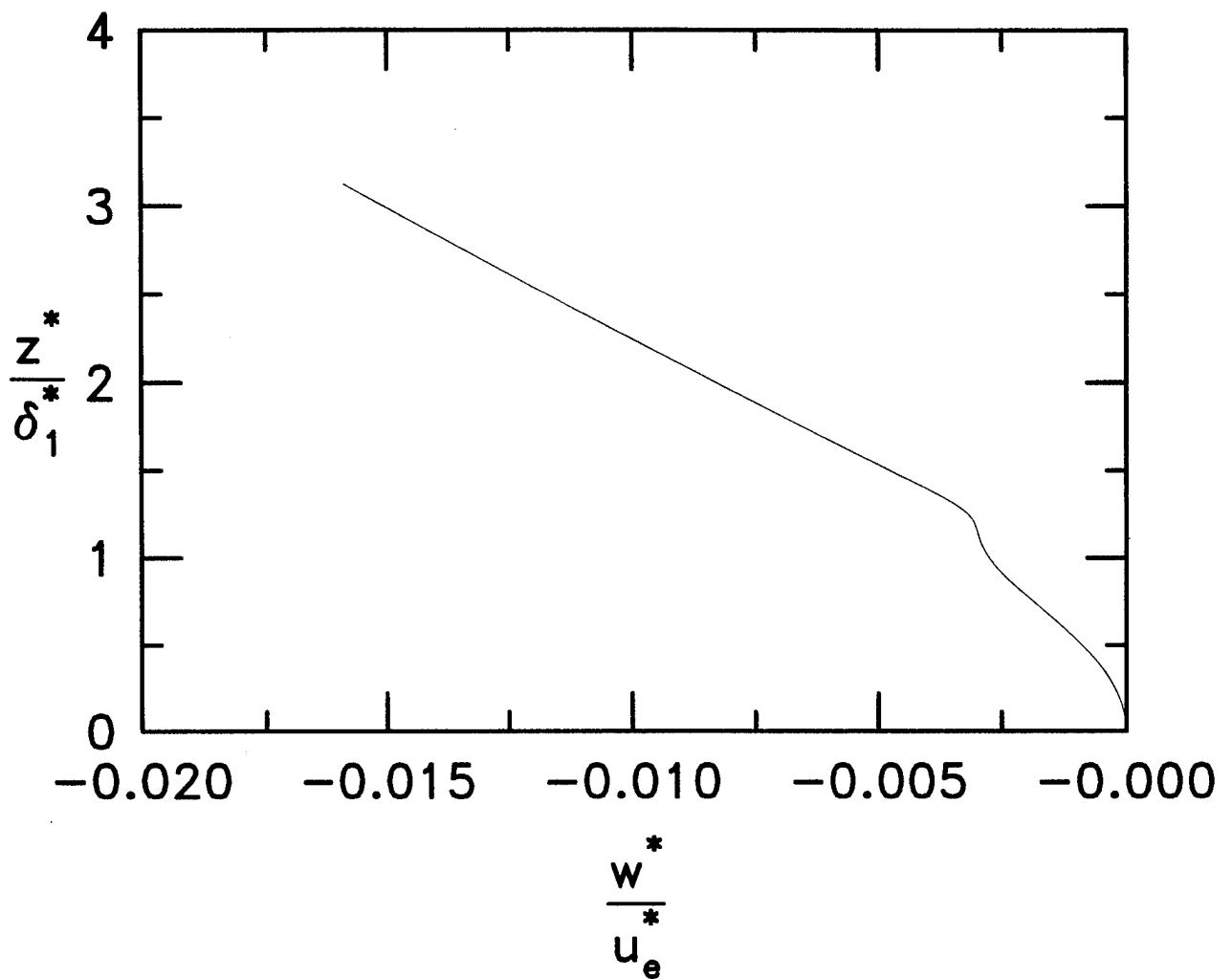


Figure 4: Normalized wall-normal velocity versus wall-normal coordinate z at axial station $x^* = 1.1725$ ft.

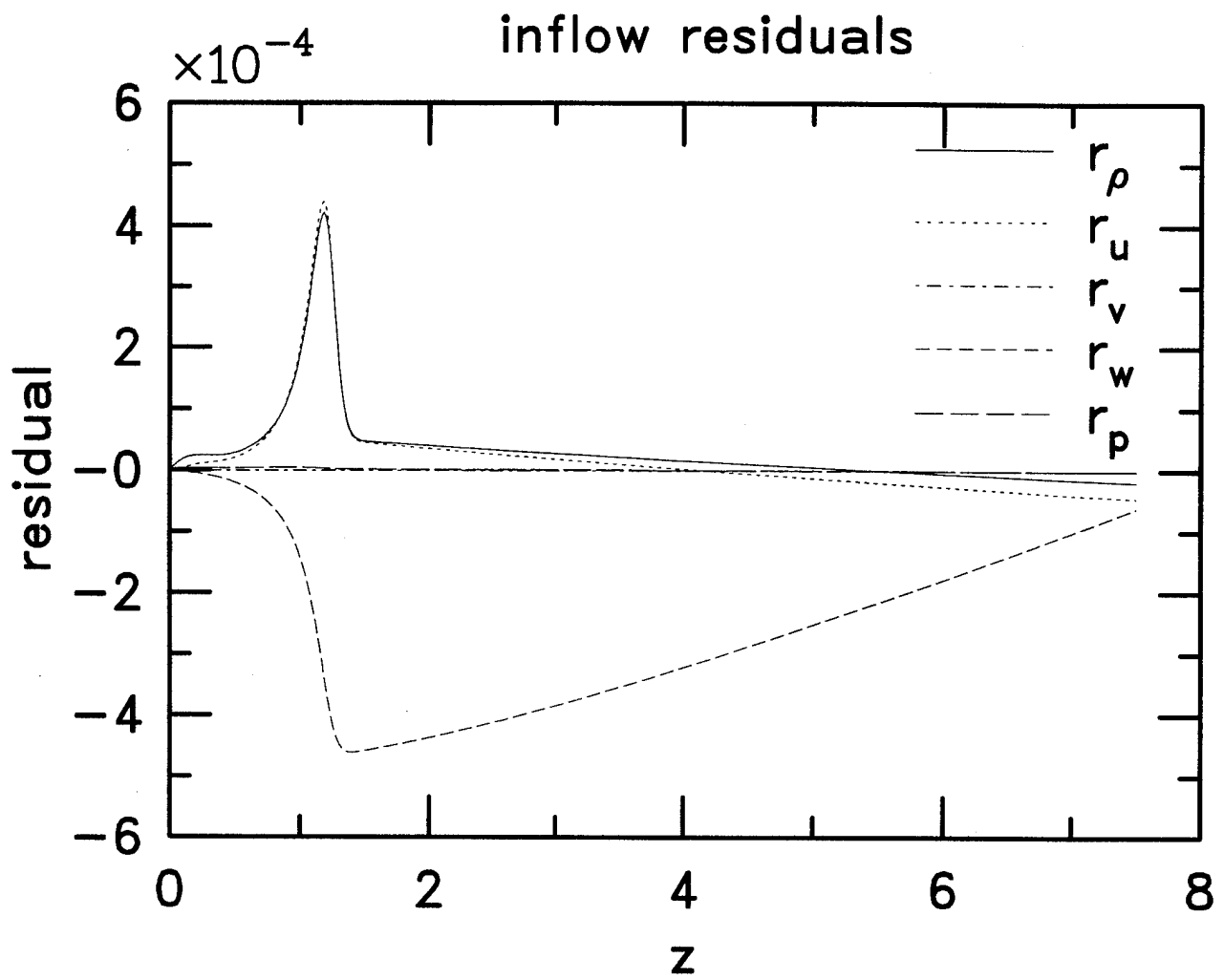


Figure 5: Residuals of governing equations along inflow boundary.

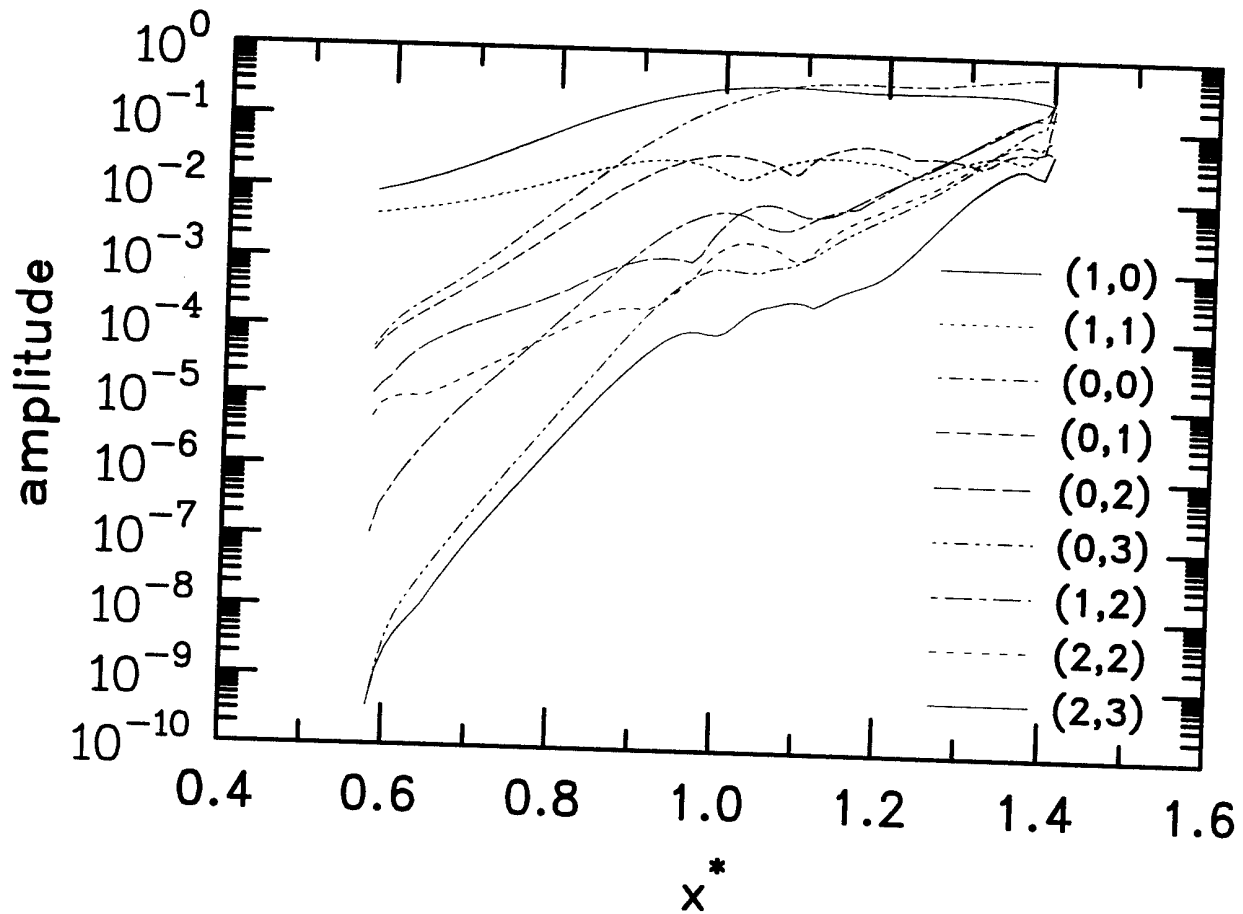


Figure 6: Streamwise evolution of maxima of selected harmonics of primary disturbances obtained from PSE method by Chang. First and second indices identify temporal and spanwise harmonics with respect to fundamental temporal frequency ω^* and spanwise wavenumber β^* , respectively, where $\beta^* R^* = 15$.

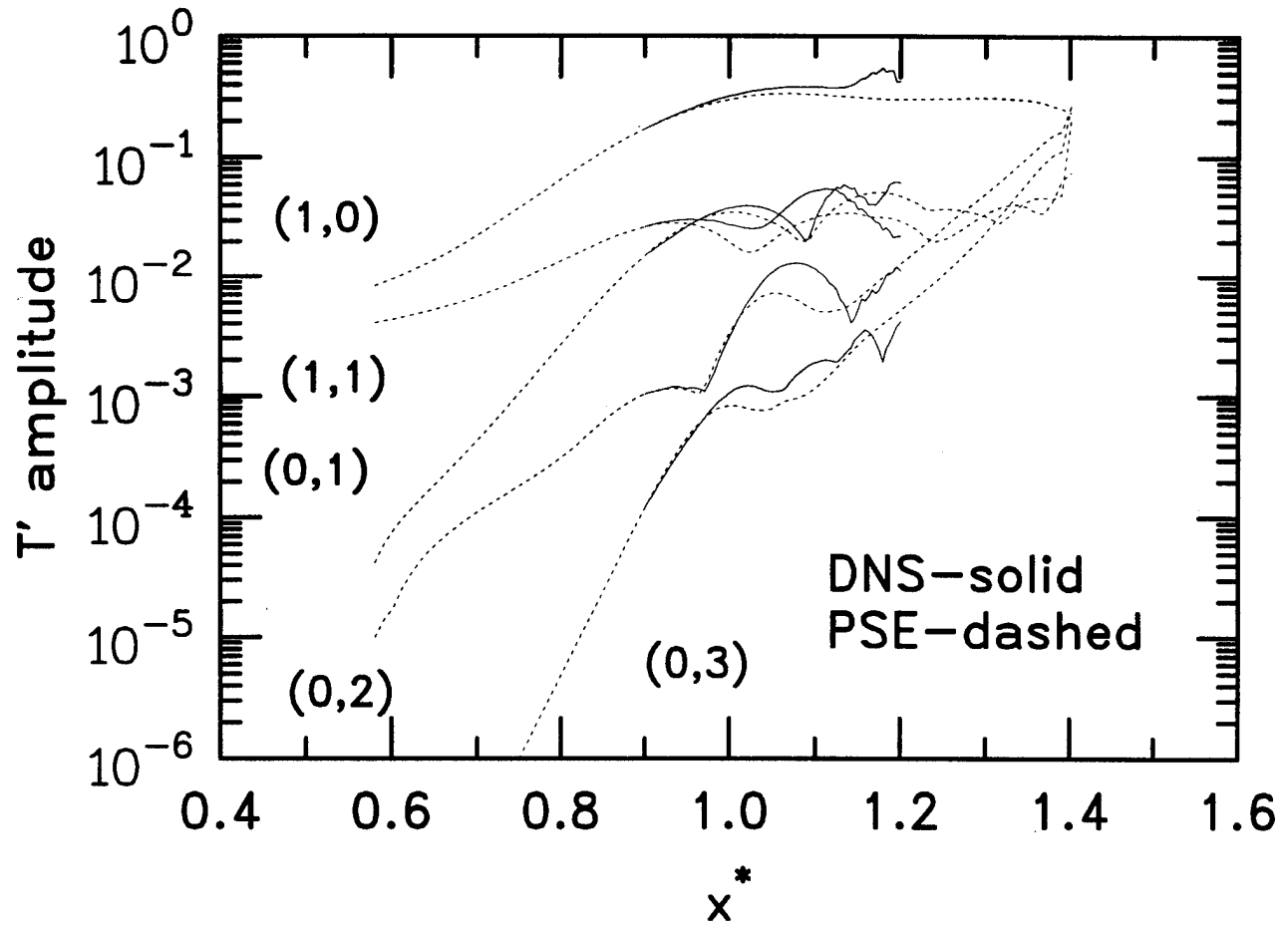


Figure 7: Comparison of DNS and PSE results for selected harmonics.

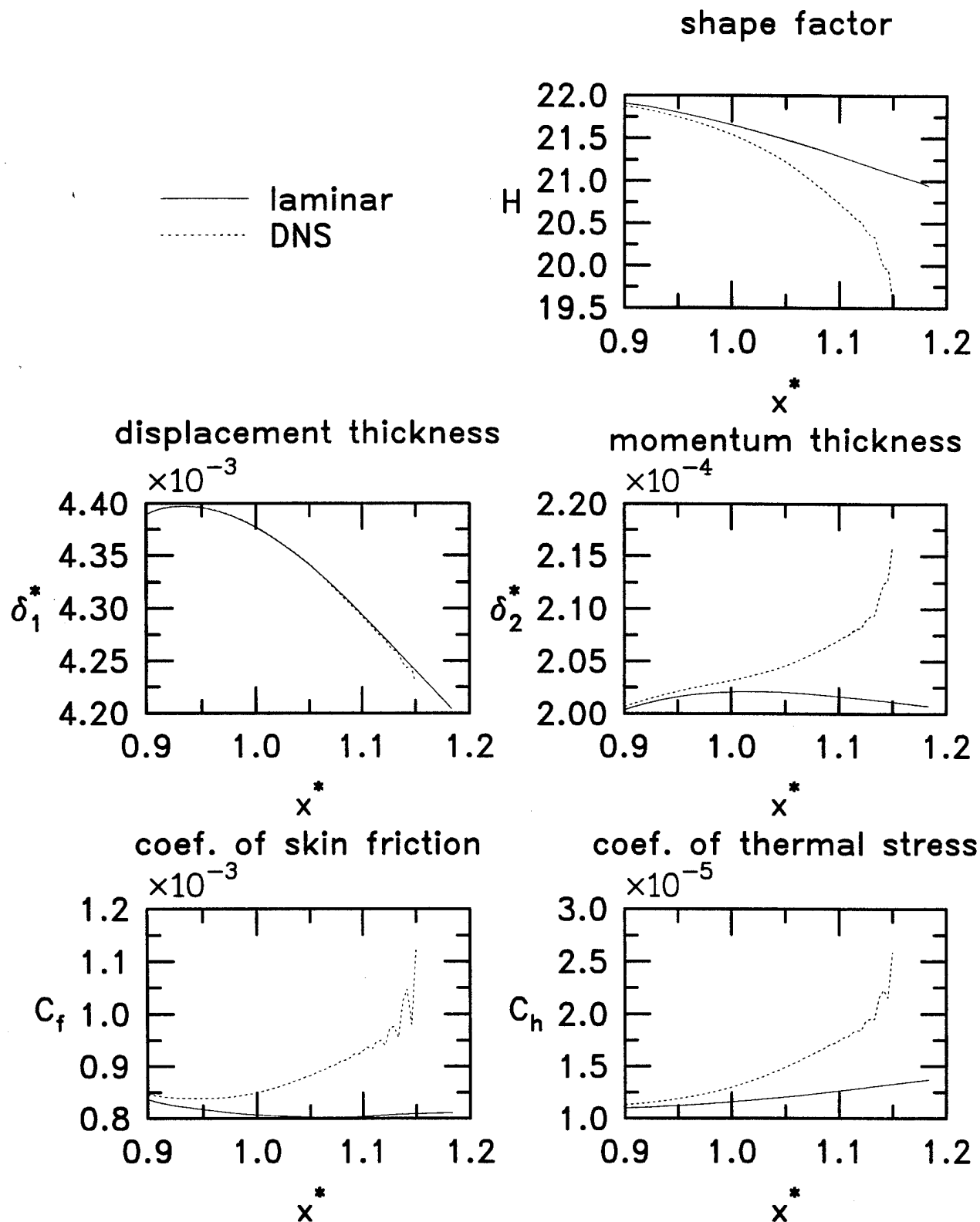


Figure 8: Streamwise evolution of selected mean quantities.

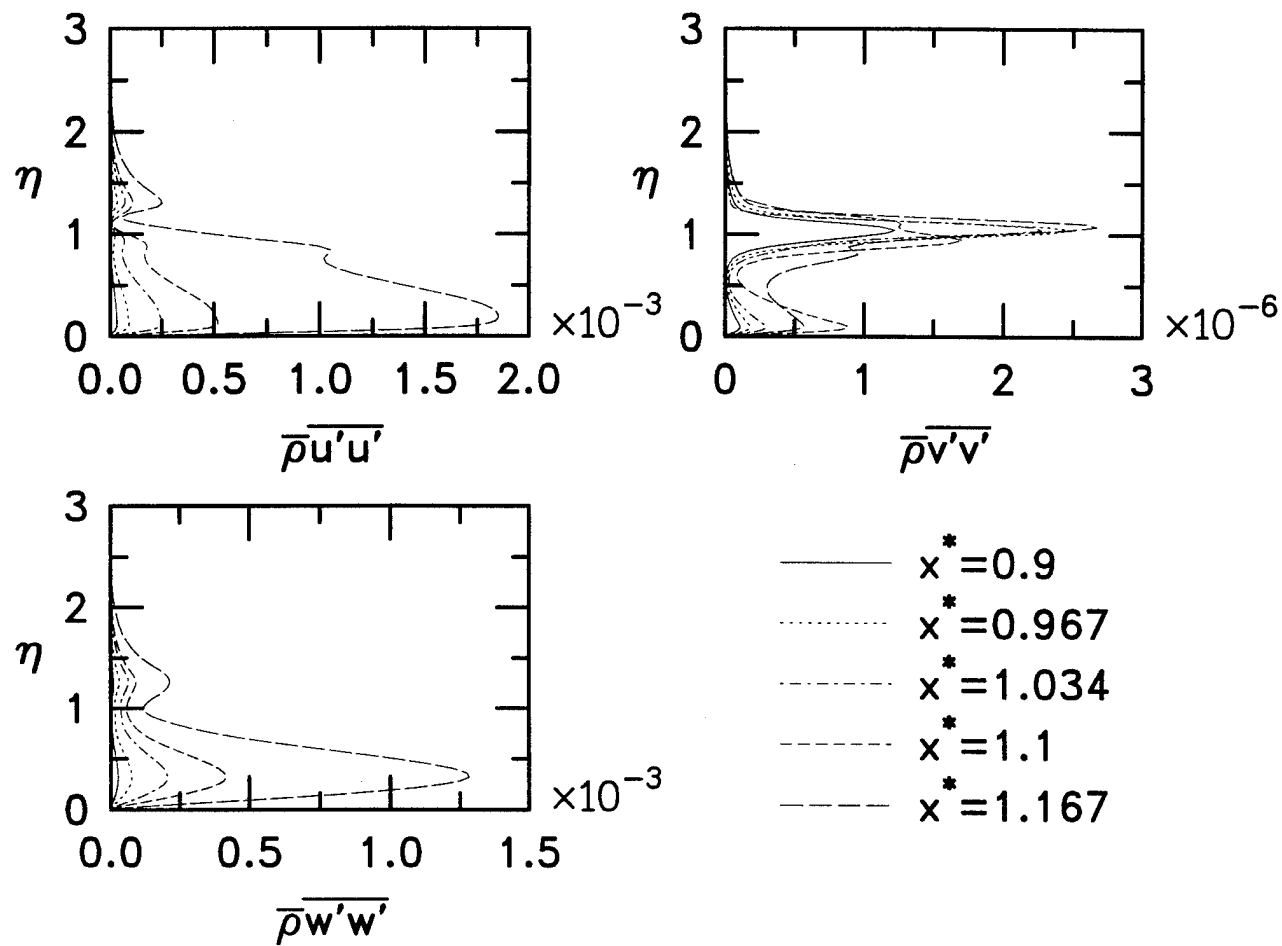


Figure 9: Streamwise evolution of principal components of Reynolds stress

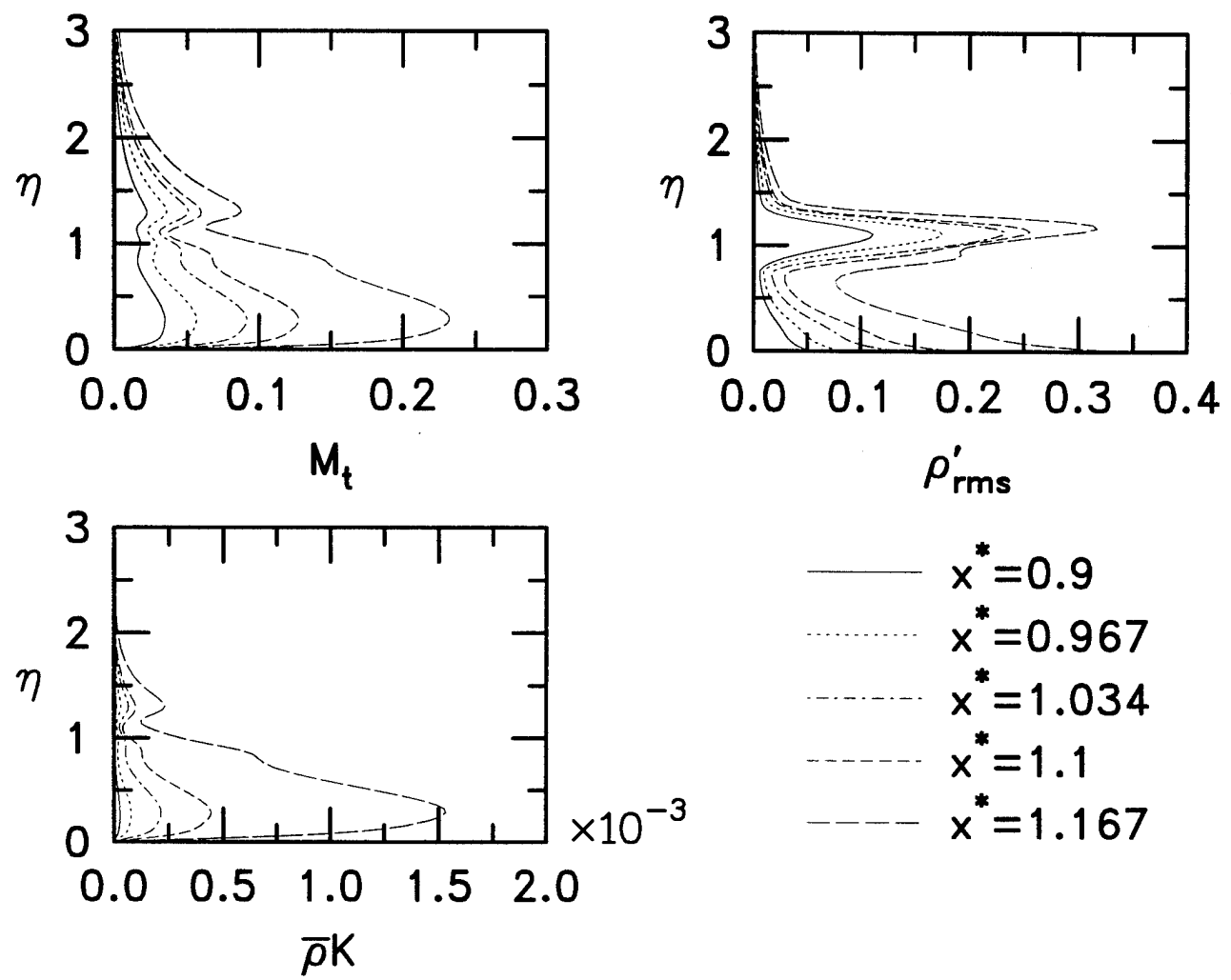


Figure 10: Streamwise evolution of turbulent Mach number, turbulent kinetic energy, and rms density fluctuation.

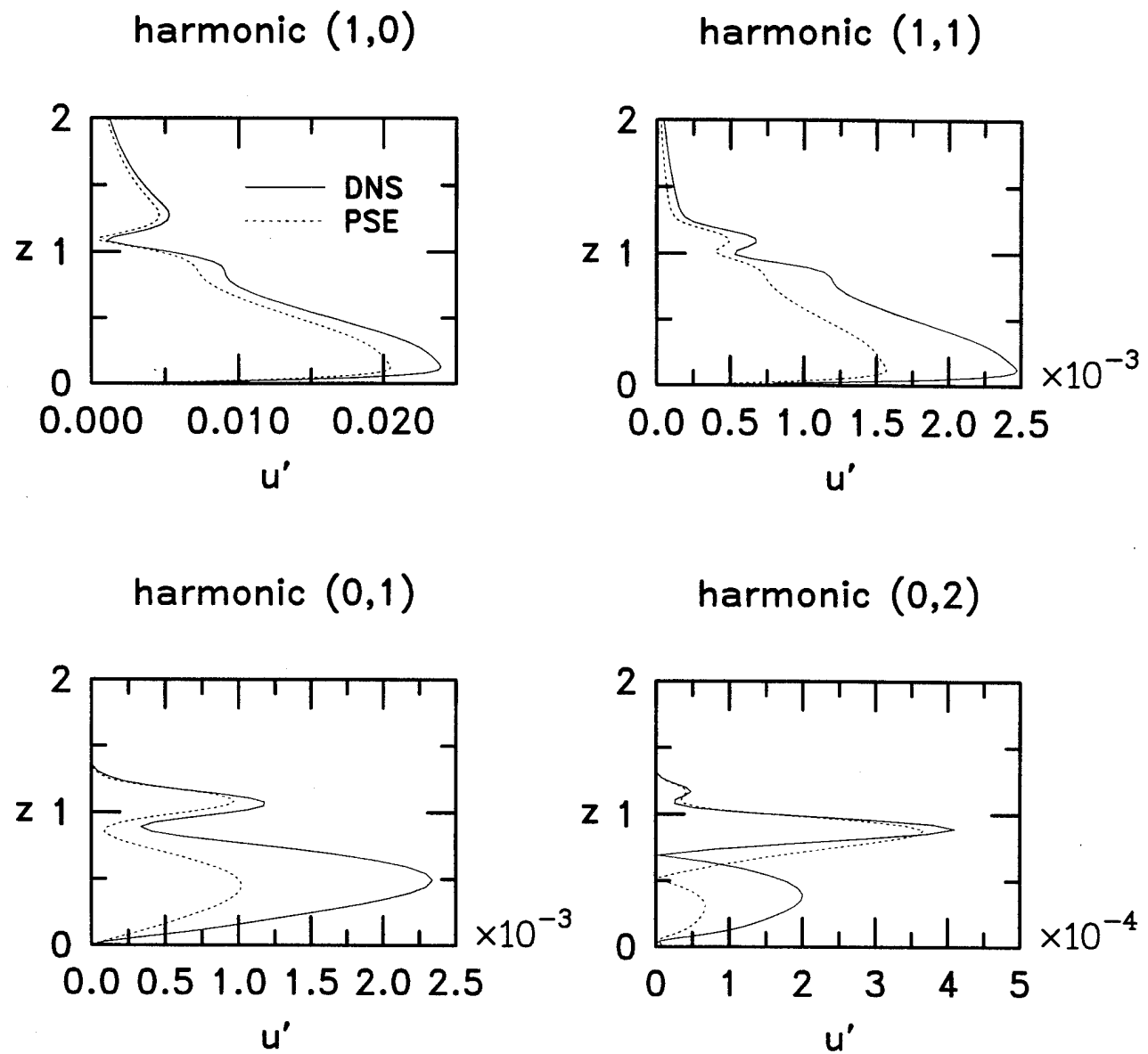


Figure 11: Amplitudes of velocity fluctuations of selected harmonics at $x^* = 1.05$ ft.

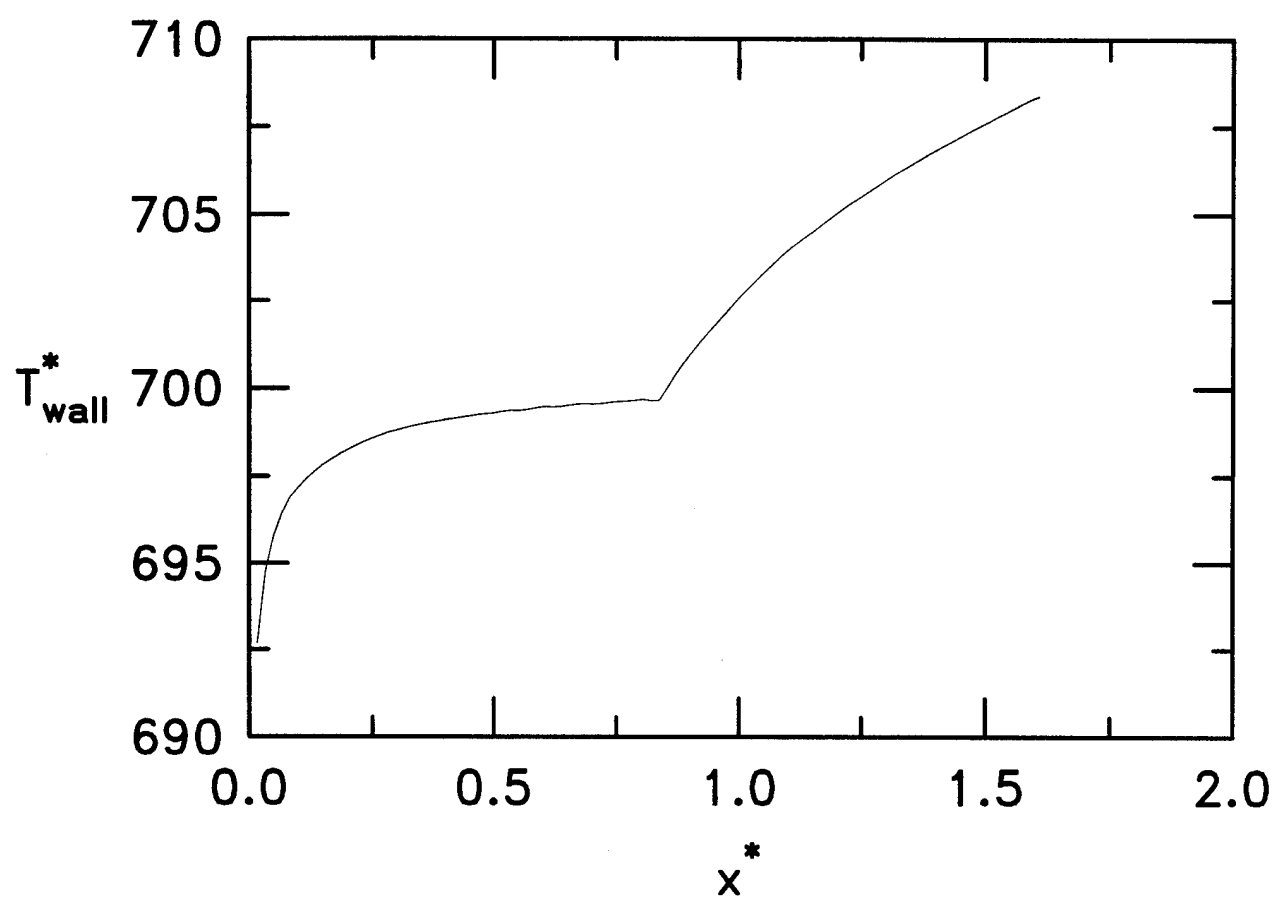
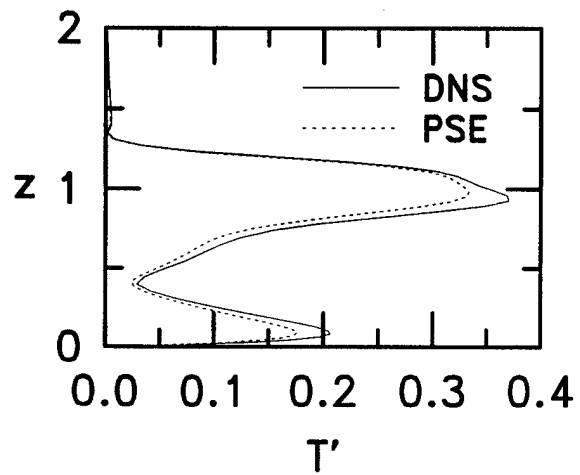
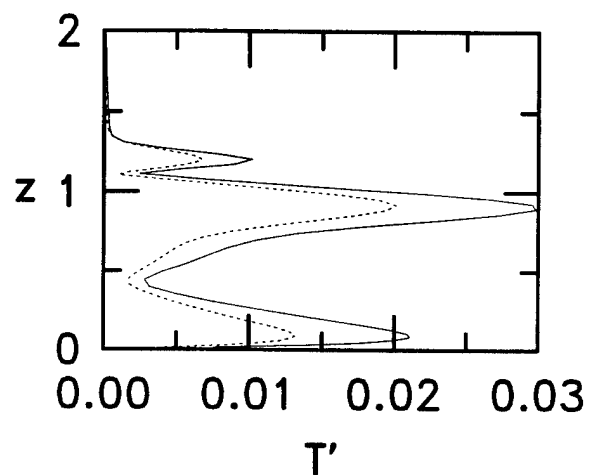


Figure 12: Laminar adiabatic-wall temperature versus arc length.

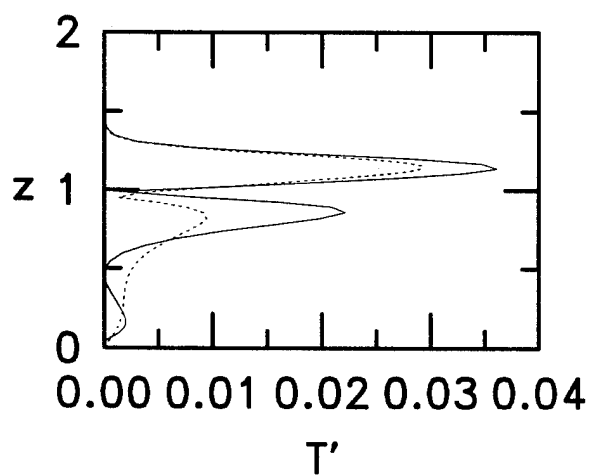
harmonic (1,0)



harmonic (1,1)



harmonic (0,1)



harmonic (0,2)

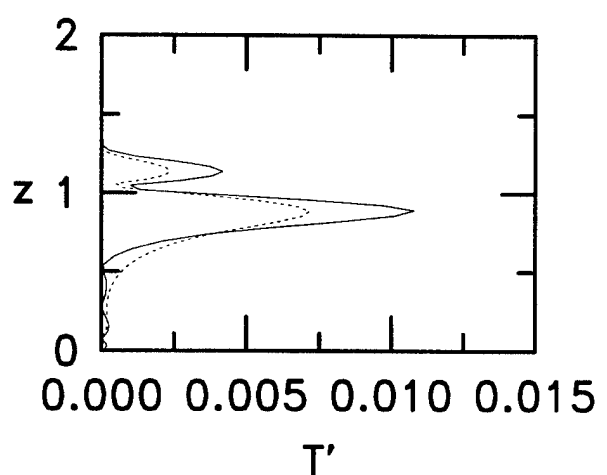


Figure 13: Amplitudes of temperature fluctuations of selected harmonics at $x^* = 1.05$ ft.

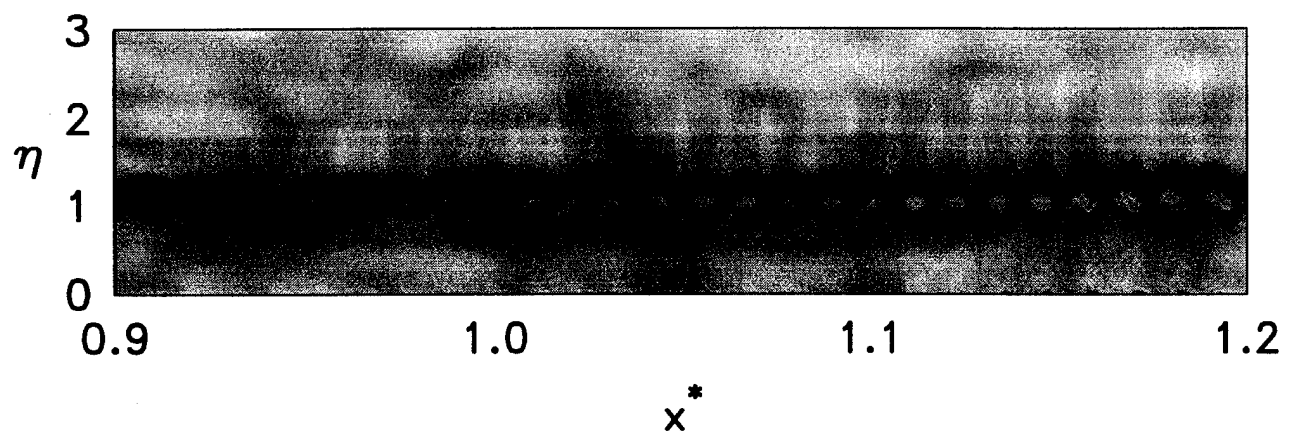


Figure 14: Computational flow image of instantaneous wall-normal density gradient showing “rope-like” appearance of dominant instability waves.

3.2 DNS of Crossflow Instability on a Supersonic Swept Wing

From a computational point of view, DNS for the elliptic-cone problem is particularly intensive because of the absence of azimuthal symmetry. That is, the computational domain must include at least one full quadrant of the elliptical cross-section. In contrast, for the circular-cone geometry of Pruett and Chang [16], symmetry considerations in conjunction with assumptions about the fundamental azimuthal wavenumber ($\beta^* R^* = 18$) allowed restriction of the computational domain to just 1/36-th of the circumference of the circular cross section. Still, the simulation of Pruett and Chang required well in excess of 1000 CPU hours on a Cray C90. Consequently, to compute laminar breakdown on the elliptic cone could consume in excess of 10,000 hours on existing supercomputers. Such a computation will be practical only on the next generation of supercomputers. In the meantime, we believe that it is important to develop the algorithms that will be needed when the next generation arrives and to gain experience with the instability mechanisms that are likely to arise on the elliptic cone and other aerospace configurations. Moreover, one can continue to validate other methodologies (e.g., PSE) against DNS by considering linear and weakly nonlinear instability waves, whose simulation is currently practicable.

As mentioned previously, it is believed that crossflow instability will dominate on the elliptic cone, but no experience exists in simulating crossflow instability for high-speed flows other than the PSE calculations of Chang et al. [5]. By considering a different configuration than the elliptic cone, namely the infinitely long swept wing, we have been able to gain experience with the simulation of crossflow instability in a supersonic boundary-layer flow. The configuration considered is the 77-degree swept wing of Cattafesta et al. [3], which is undergoing stability and transition tests in NASA Langley's Mach 3.5 quite wind tunnel. Near the aft station of the wing, cross sections are similar and pressure isobars are nearly parallel to the leading edge. Consequently, one can approximate the flow as quasi-three-dimensional; that is, the base flow varies only in the streamwise and wall-normal directions and not in the spanwise direction (parallel to the leading edge). This approximation is equivalent to assuming that the wing is infinitely long in span and permits a spanwise periodicity assumption for the perturbed flow. As a result of the particular periodicity assumption, DNS can be performed with reasonable CPU requirements.

This work was begun under NASA contract NAS1-19656 and was brought to the current state under the present AFOSR grant. The production run was accomplished under the auspices of AFOSR on the Waterways Experiment Station (WES) Cray C90 at Vicksburg, MS. Progress to date is documented thoroughly in Attachment 2, a NASA Contractor Report entitled "Simulation of Crossflow Instability on a Supersonic Highly Swept Wing," and the reader is referred to the attachment for further details. At present we have considered only stationary crossflow modes; traveling crossflow modes also need to be considered.

3.3 Setup of Elliptic-Cone Problem

To avoid confusion with the flared-cone work presented earlier, please note that different coordinate notation is used for the elliptic-cone problem. Here x , y , and z denote major axis, minor axis, and axial coordinates respectively,

- The few available documents (Refs. [7], [11], and [19]) on the elliptic-cone problem were reviewed. It was realized that, in essence, the elliptic-cone configuration can be considered a “fat” and symmetrical highly swept wing, and if the eccentricity ratio is moderately large, the flow will be dominated by crossflow instability. This realization precipitated the swept-wing study mentioned in the previous subsection.
- Some thought was given to determination of the laminar base state, which may turn out to be the most difficult task for the elliptic-cone problem. Unlike all other problems addressed previously by this P.I., the elliptic-cone problem presents ultimately the difficulty of a fully three-dimensional base flow. Two possible options currently exist to determine the basic state. Both Lytle and Reed [11] and Huang et al. [7] exploit parabolized Navier-Stokes (PNS) technology to determine the base flow. However, Lytle and Reed state: “The treatment of the subsonic pressure gradient terms introduces errors that make the calculated basic state unsuitable for stability analysis.” In our experience, PNS calculations often require numerical dissipation that may artificially but significantly alter the stability of the base state. Moreover, well-resolved PNS computations can be expensive computationally, requiring on the order of 100 CPU hours on a supercomputer. Consequently, we prefer at the present time to use an Euler/boundary-layer approach whereby the outer flow is determined by solution of the Euler equations and the inner solution is obtained from the boundary-layer equations. Fortunately, for conical flows, including flow over an elliptic cone, the inviscid flow does not vary along cone generators, as will be verified later. Once again, this permits a simplifying assumption by which the flow can be approximated as quasi-three-dimensional. It is not altogether certain that this approach will work, however, because the conical-flow boundary-layer solution will not automatically satisfy symmetry conditions. Our intuition is that the approach will work for the case of zero angle of attack but that viscous-inviscid interaction will become too strong when the cone is at non-zero incidence angle to the flow.
- An elliptic-cone configuration was defined based on the model used by Schneider [19] for his Ludwieg-tube experiments; nominal freestream conditions were also obtained from Schneider’s experiment. The model is 5 inches long with a sharp apex and elliptical cross sections. The eccentricity ratio is 4:1, and the major-axis semi-vertex angle is 17.5 degrees. At a freestream unit Reynolds number of $Re_1 = 1,431,070$, the freestream conditions are $M_\infty = 4.0$, $p_\infty^* = 13.66$ psf., and $T_\infty^* = 128.7$ Rankine, for a ratio of specific heats, $\gamma = 1.4$.

- The Euler equations were solved for the configuration and flow conditions above. Specifically, the marching Euler code “ARROW” of Salas [18] was used to obtain the inviscid solution. The pressure coefficient so obtained is shown versus the scaled minor-axis coordinate y in Fig. 15, for several streamwise stations z . Note that, in scaled coordinates, all profiles collapse onto one as the solution is marched downstream; thus, the conical-flow assumption is verified for this configuration. Since the starting condition for ARROW assumes the cross-section is circular, the initial profiles are in error but do not significantly affect the z -asymptotic state.
- The governing boundary-layer equations for conical flow were derived so that the spectrally accurate boundary-layer code of Pruett and Streett [13] could be modified to incorporate conical flows. The modification to the code has not yet been accomplished.
- An interpretation routine was written to convert the output of the inviscid solution into edge conditions for the boundary-layer code. The boundary-layer equations exploit a body-fitted coordinate system for which coordinates x' , y' , and z' specify the distance along the cone generators, the arc length perpendicular to the generator, and the wall-normal distance, respectively. The corresponding edge velocities, u_e^* , v_e^* , and w_e^* , are shown in Figs. 16, 17, and 18, respectively. By definition, the normal velocity w_e^* should vanish for inviscid flow; hence, the small values shown in Fig. 18 serve purely as a check that the inviscid solution has been properly computed and/or interpreted.
- Some thought was given to derivation of the compressible Navier-Stokes equations in a body-fitted coordinate system for the elliptic-cone configuration, as was done by Pruett et al. [15] for the cone and/or flared-cone configurations. Unfortunately, the absence of azimuthal symmetry adds a quantum leap in complexity to the metric terms for the elliptic-cone problem. Thus, it is our judgement that the elliptic-cone problem is best treated by resorting to generalized curvilinear coordinates. From a computational point of view, generalized coordinates will likely increase CPU and memory requirements each by a factor of two relative to the current baseline code. The advantage, however, is that configurations other than the elliptic cone could be treated readily in a generalized coordinate system.
- Additional thought was given to optimal parameterization of the azimuthal coordinate for the elliptic-cone configuration. Huang et al. [7] parameterize as if the cross-section were circular; that is, based on the angle ξ^3 formed by rays from the center to points on the surface. This parameterization has the unfortunate trait of placing points further apart in regions where curvature is largest. We favor parameterization based on the “clock angle” ζ formed by the surface normal. Fig. 19 contrasts the two parameterizations for the edge Mach number M_e . Note that the Mach number distribution is much smoother in the preferred parameterization.

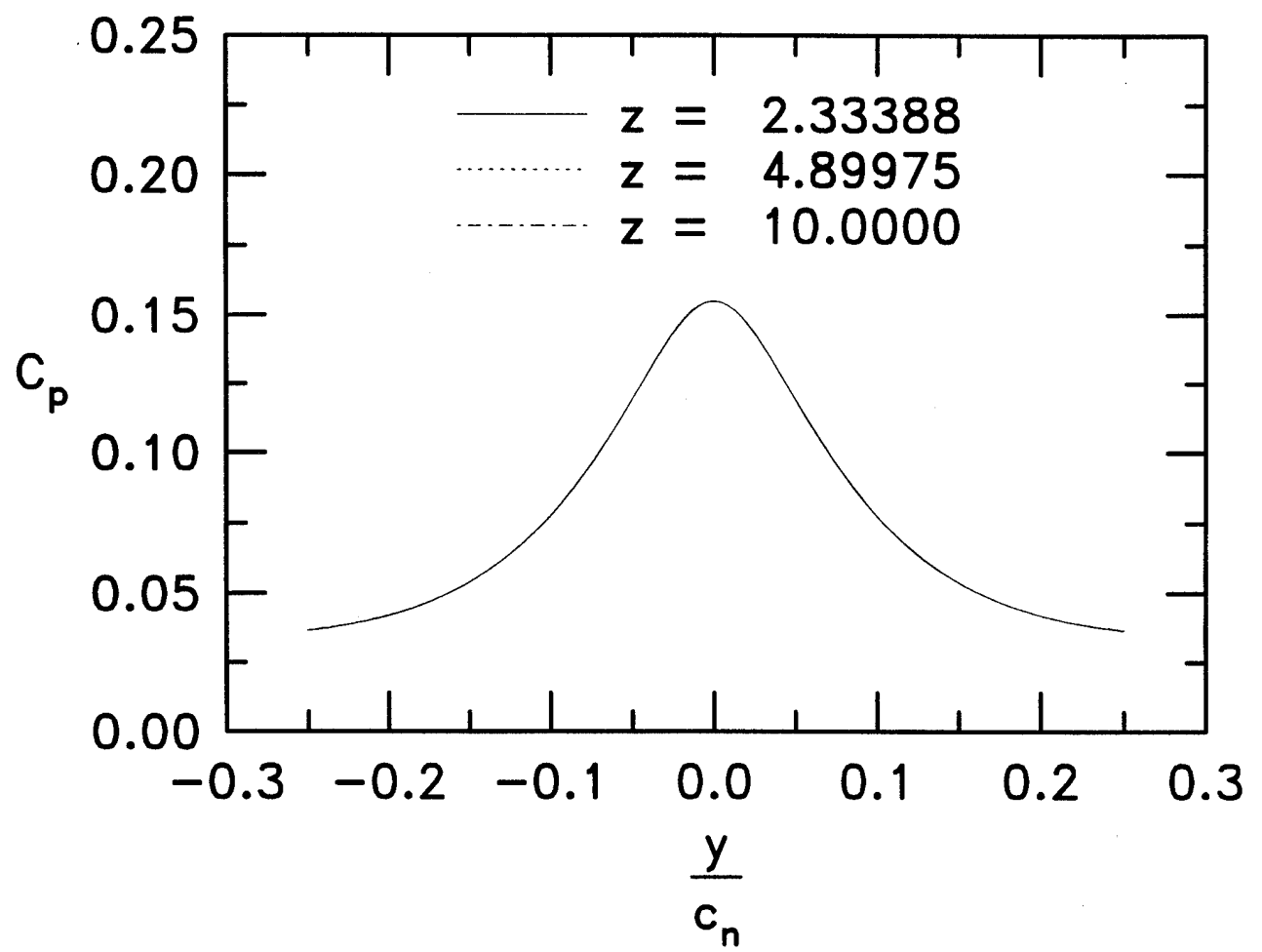


Figure 15: Inviscid surface pressure coefficient versus scaled minor-axis coordinate at three axial stations obtained with ARROW code of Salas. Collapse of all three profiles onto one curve indicates that flow is conical on elliptic cone. (Length of major semi-axis is c_n .)

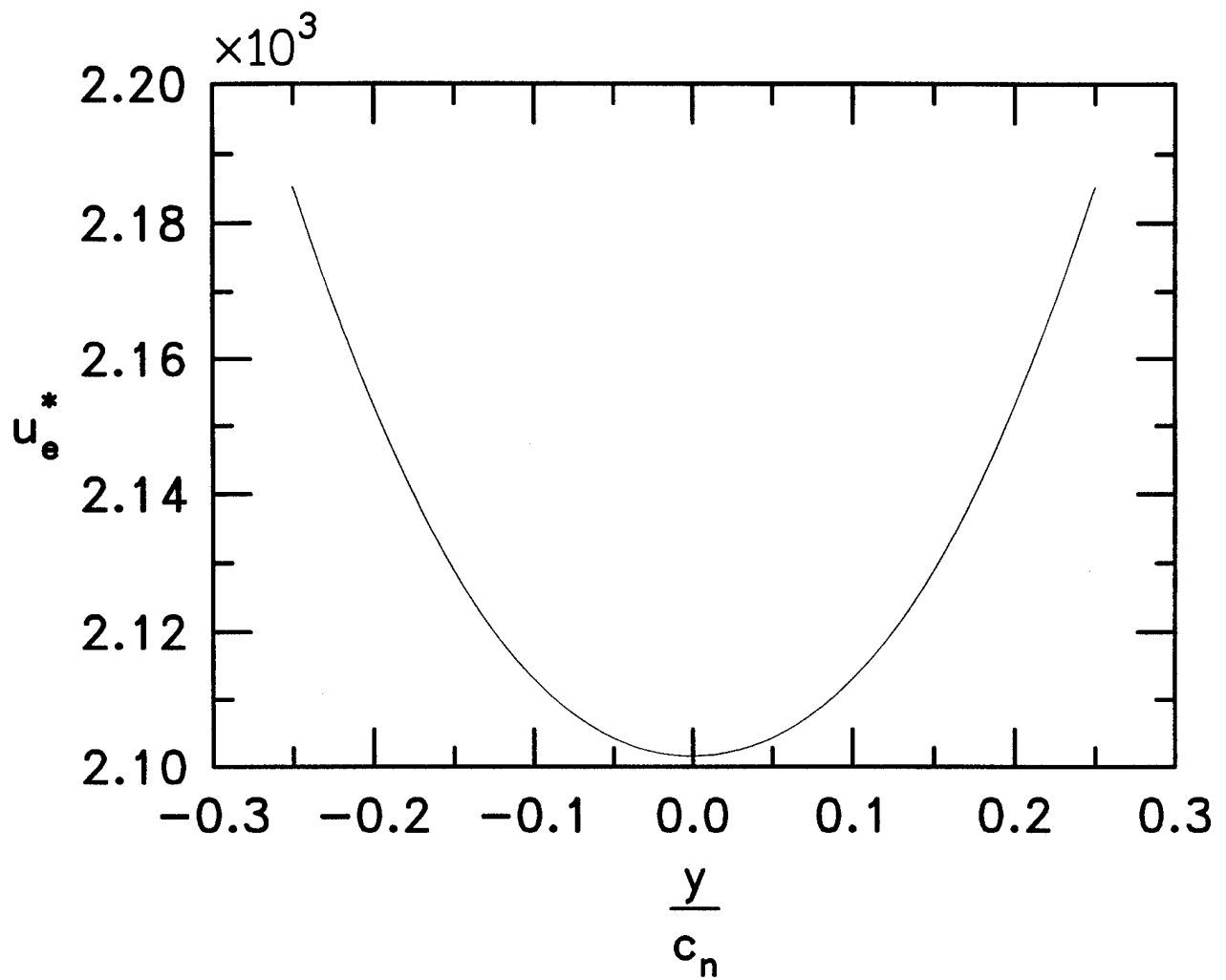


Figure 16: Inviscid velocity in direction along cone generator versus scaled minor-axis coordinate.

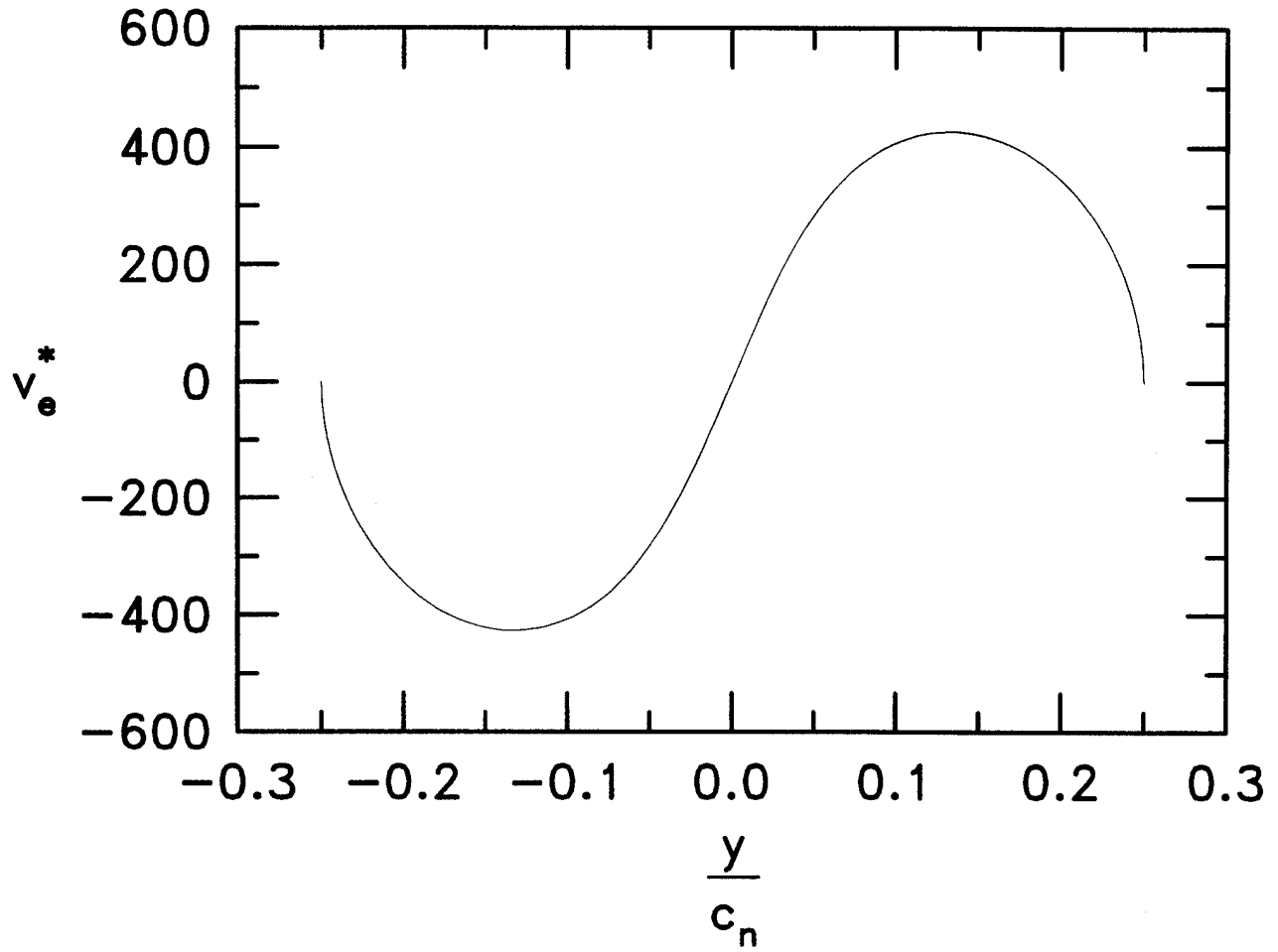


Figure 17: Inviscid velocity in direction perpendicular to cone generator and tangent to surface versus scaled minor-axis coordinate.

77-Degree Swept Wing
Mach 3.29
Disurbance Density

Acoustic Radiation
from Developing Wavefront

17. Contours of constant disturbance density in computational plane normal to both leading edge and wing surface showing acoustic energy generated by strong nonlinearity in wave-packet region.

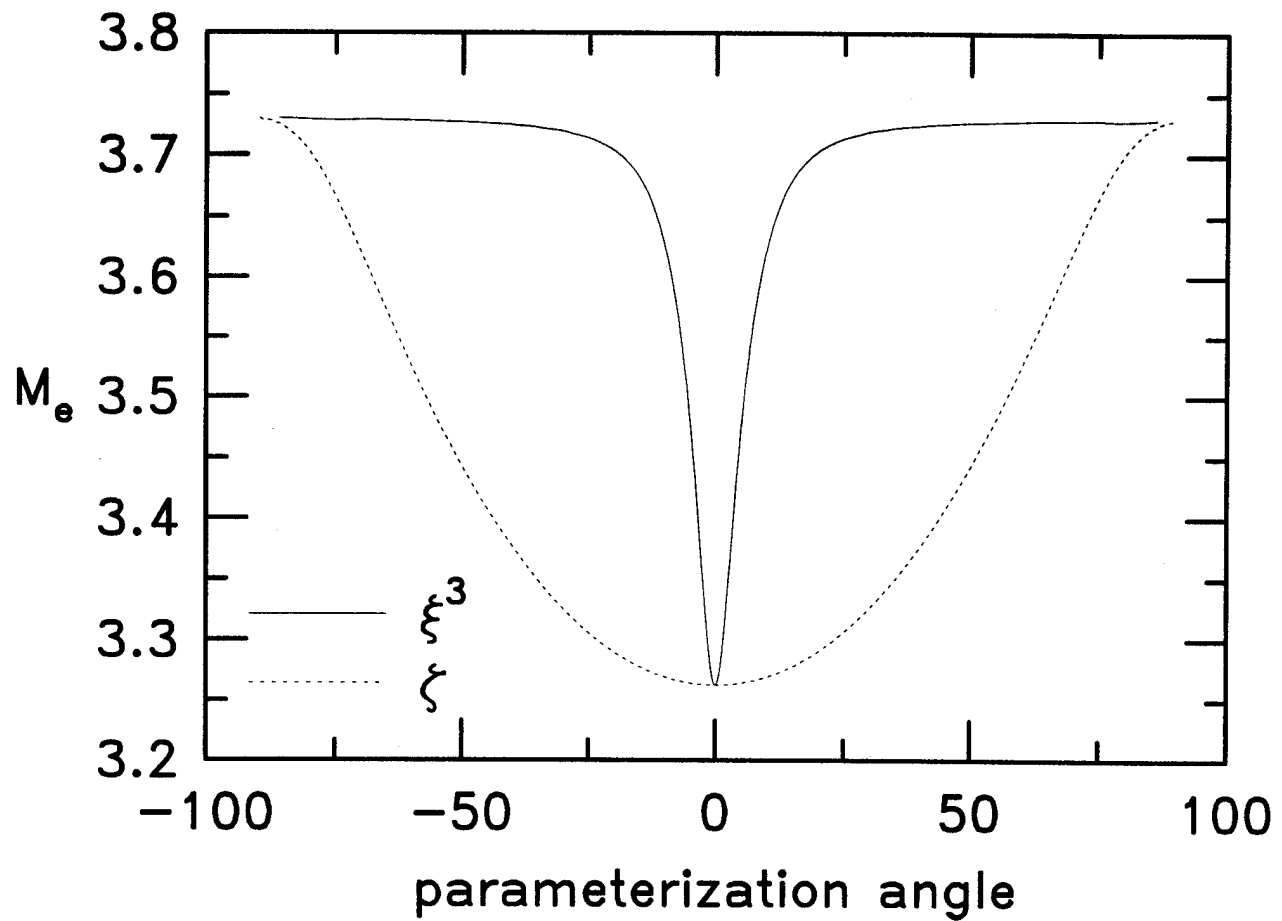


Figure 19: Comparison of two possible parameterizations of azimuthal coordinate for elliptic-cone problem. Proposed clock-angle parameterization results in better distribution of grid points.

4 Personnel

This grant has supported the research efforts of the Principal Investigator, Dr. C. David Pruett, Dept. of Applied Science, The College of William and Mary, Williamsburg, VA. In addition, Dr. Chau-Lyan Chang of High Technology Corporation, Hampton, VA, has contributed substantially to this effort without remuneration from AFOSR.

5 Publications

- C. D. Pruett and C.-L. Chang, "Spatial Direct Numerical Simulation of High-Speed Boundary-Layers Flows—Part II: Transition on a Cone in Mach 8 Flow," *Theoretical and Computational Fluid Dynamics*, Vol. 7, No. 5, 1995, pp. 397-424.
- C. D. Pruett and T. A. Zang, "On Simulation and Analysis of Instability and Transition in High-Speed Boundary-Layer Flows," *Computing Systems in Engineering*, to appear.
- C. D. Pruett, "Spatial Direct Numerical Simulation of Transitioning High-Speed Flows" (Invited Paper), presented to the Second Symposium on Transitioning and Turbulent Compressible Flows at the ASME/JSME Fluids Engineering Annual Conference, Hilton Head, SC, 13-18 August, 1995.

6 Interactions/Transitions

- Addressed the Virginia Consortium of Engineering and Science Universities (VCES) Seminar in Hampton, VA, on 10 March, 1995, on the topic of "Direct Numerical Simulation of Transitioning High-Speed Flows."
- Visited AFOSR at Bolling AFB, DC, on 24 July, 1995, to discuss current and future directions of this effort with the technical monitor, Dr. Leonidas Sakell.
- Addressed the Second Symposium on Transitional and Turbulent Compressible Flows at the ASME/JSME Fluids Engineering Annual Conference, Hilton Head, SC, 13-18 August, 1995. (See "Publications.")

7 Discoveries, Inventions, or Patents

A qualitative difference exists between transitioning hypersonic boundary-layer flows on axisymmetric straight and flared cones. For the case of the straight cone, Reynolds stresses are largest near the critical layer, spreading toward the wall only through nonlinear effects. For

the flared cone, Goertler modes, associated with concave streamwise curvature, are linearly unstable and introduce large fluctuations close to the wall in the relatively early stages of transition. As a result, Reynolds stresses peak close to the wall. From an engineering-design point of view, transition onset, as determined by increased wall shear and thermal transfer, will be observed sooner in the flared-cone case. However, the transition process is relatively gradual and the transition zone may be relatively long for the flared cone.

8 Honors and Awards

Invited to address the Symposium on Transitional and Turbulent Compressible Flows at the ASME/JSME Fluids Engineering Annual Conference, Hilton Head, SC, 13-18 August, 1995. (See "Interactions" and "Publications.")

9 Attachments

1. Paper by Pruett, Zang, Chang, and Carpenter entitled "Spatial Direct Numerical Simulation of High-Speed Boundary-Layer Flows—Part I: Algorithmic Considerations and Validation."
2. NASA Contractor Report by Pruett entitled "Simulation of Crossflow Instability on a Supersonic Highly Swept Wing."

References

- [1] P. Balakumar and M. R. Malik, "Effect of Adverse Pressure Gradient and Wall Cooling on Instability of Hypersonic Boundary Layers," High Technology Report No. HTC-9404, 1994.
- [2] C. Canuto, A. Quarteroni, M. Y. Hussaini, and T. A. Zang, *Spectral Methods in Fluid Dynamics*, Springer-Verlag, Berlin, 1988.
- [3] L. N. Cattafesta III, V. Iyer, J. A. Masad, R. A. King, and J. R. Dagenhart, "Three-Dimensional Boundary-Layer Transition on a Swept Wing at Mach 3.5," AIAA Paper No. 94-2375, 1994.
- [4] C.-L. Chang and M. R. Malik, "Non-parallel Stability of Compressible Boundary Layers," AIAA Paper No. 93-2912, 1993.
- [5] C.-L. Chang, M. R. Malik, and H. Vinh, "Linear and Nonlinear Stability of Compressible Swept-Wing Boundary Layers," AIAA Paper 95-2278, 1995.
- [6] C.-L. Chang, High Technology Corporation, Hampton, VA, personal communication, 1995.
- [7] S. L. Huang, G. K. Stuckert, and Th. Herbert, "Cross-Flow Instability of the Supersonic Flow over a 4:1 Elliptic Cone," Final Report for AFOSR Contract F49620-94-C-0053.
- [8] R. L. Kimmel, "The Effect of Pressure Gradients on Transition Zone Lengths in Hypersonic Boundary Layers," Wright Laboratory Report WL-TR-94-3012, December 1993.
- [9] J. T. Lachowicz, N. Chokani, and S. P. Wilkinson, "Hypersonic Boundary-Layer Stability Over a Flared Cone in a Quiet Tunnel," AIAA Paper No. 96-0782.
- [10] S. K. Lele, "Compact Finite-Difference Schemes with Spectral-Like Resolution," *J. Comput. Phys.*, Vol. 103, 1992, pp. 16-42.
- [11] I. J. Lytle and H. L. Reed, "Use of Transition Correlations for Three-Dimensional Boundary Layers within Hypersonic, Viscous Flows," presented at the Second Symposium on Transitional and Turbulent Compressible Flows of the ASME/JSME Fluids Engineering Annual Meeting, Hilton Head, SC, 13-18 August, 1995.
- [12] L. M. Mack, "Boundary-Layer Stability Theory," in *Special Course on Stability and Transition of Laminar Flow*, ed. R. Michel, AGARD Report No. 709, 1984, pp. 3.1-3.81.
- [13] C. D. Pruett and Craig L. Streett, "A Spectral Collocation Method for Compressible, Non-similar Boundary Layers," *Int. J. Numer. Meth. Fluids*, **13**, 6, 1991, pp. 713-737.
- [14] C. D. Pruett, "On the Accurate Prediction of the Wall-Normal Velocity in Compressible Boundary-Layer Flow," *Int. J. Numer. Meth. Fluids*, **16**, 1993, pp. 133-152.

- [15] C. D. Pruett, T. A. Zang, C.-L. Chang, and M. H. Carpenter, "Spatial Direct Numerical Simulation of High-Speed Boundary-Layer Flows—Part I: Algorithmic Considerations and Validation," *Theoret. Comput. Fluid Dynamics*, Vol. 7, No. 1, 1995, pp. 49-76.
- [16] C. D. Pruett and C.-L. Chang, "Spatial Direct Numerical Simulation of High-Speed Boundary-Layer Flows—Part II: Transition on a Cone in Mach 8 Flow," *Theoret. Comput. Fluid Dynamics*, to appear.
- [17] C. D. Pruett and T. A. Zang, "On Simulation and Analysis of Instability and Transition in High-Speed Boundary-Layer Flows," *Computing Systems in Engineering* (to appear).
- [18] M. D. Salas, NASA Langley Research Center, Hampton, VA, personal communication, 1995.
- [19] S. Schneider, "Informal Progress Report on Elliptic Cone Transition Experiments," Purdue University, 27 April 1995.
- [20] L. G. Smith, "Pulsed-Laser Schlieren Visualization of Hypersonic Boundary-Layer Instability Waves," AIAA Paper No. 94-2639, 1994.
- [21] K. F. Stetson, E. R. Thompson, J. C. Donaldson, and L. G. Siler, "Laminar Boundary-Layer Stability Experiments on a Cone at Mach 8. Part 1: Sharp Cone," AIAA Paper No. 83-1761, 1983.
- [22] C. L. Streett and M. G. Macaraeg, "Spectral Multi-Domain for Large-Scale Fluid Dynamic Simulations," *Appl. Numer. Math.*, Vol. 6, 1989/90, pp. 123-139.
- [23] K. W. Thompson, "Time Dependent Boundary Conditions for Hyperbolic Problems," *J. Comput. Phys.*, Vol. 68, 1987, pp. 1-24.
- [24] S. P. Wilkinson and S. G. Anders, "Instability and Transition on a Conical Model with Adverse Pressure Gradient in a Quiet Hypersonic Wind Tunnel," draft copy of a proposed NASA Technical Paper, 1994.
- [25] J. H. Williamson, "Low-Storage Runge-Kutta Schemes," *J. Comput. Phys.*, Vol. 35, pp. 48-56.

Attachment 1

Spatial Direct Numerical Simulation of High-Speed Boundary-Layer Flows

Part I: Algorithmic Considerations and Validation

C. David Pruett

Analytical Services & Materials, Inc., Hampton, VA 23666, U.S.A.

Thomas A. Zang

Computational Sciences Branch, NASA Langley Research Center,
Hampton, VA 23681, U.S.A.

Chau-Lyan Chang

High Technology Corporation, Hampton, VA 23665, U.S.A.

Mark H. Carpenter

Theoretical Flow Physics Branch, NASA Langley Research Center,
Hampton, VA 23681, U.S.A.

Communicated by M.Y. Hussaini

Received 6 May 1993 and accepted 13 August 1993

Abstract. A highly accurate algorithm for the direct numerical simulation (DNS) of spatially evolving high-speed boundary-layer flows is described in detail and is carefully validated. To represent the evolution of instability waves faithfully, the fully explicit scheme relies on non-dissipative high-order compact-difference and spectral collocation methods. Several physical, mathematical, and practical issues relevant to the simulation of high-speed transitional flows are discussed. In particular, careful attention is paid to the implementation of inflow, outflow, and far-field boundary conditions. Four validation cases are presented, in which comparisons are made between DNS results and results obtained from either compressible linear stability theory or from the parabolized stability equation (PSE) method, the latter of which is valid for nonparallel flows and moderately nonlinear disturbance amplitudes. The first three test cases consider the propagation of two-dimensional second-mode disturbances in Mach 4.5 flat-plate boundary-layer flows. The final test case considers the evolution of a pair of oblique second-mode disturbances in a Mach 6.8 flow along a sharp cone. The agreement between the fundamentally different PSE and DNS approaches is remarkable for the test cases presented.

1. Introduction

A worthy “grand challenge” for the computational boundary-layer-transition community is the accurate direct numerical simulation (DNS) of the complete laminar-turbulent transition process in a spatially evolving high-speed boundary-layer flow. Even for such simple geometries as the flat plate or

sharp cone, this remains a daunting goal. It was only in the late 1980s that the corresponding challenge for temporally evolving incompressible flow was met by Gilbert and Kleiser (1990) for the relatively simple problem of channel-flow transition. For spatially evolving compressible boundary-layer flows, the recent landmark simulations of Rai and Moin (1991) and Thumm (1991) have come closest to the realization of this goal. In the former simulation a fully turbulent state was attained from an initially laminar state subject to high-amplitude random forcing imposed in the free stream. However, although the algorithm was designed for compressible flow, the low subsonic Mach number (Mach 0.1) of the numerical experiment guaranteed that the flow was essentially incompressible in behavior. The latter computation of Thumm (1991) considered a relatively low-speed supersonic flow (Mach 1.6), and, while simulating highly nonlinear stages of transition, it did not proceed into a fully turbulent regime. (For a thorough background of DNS for transitional incompressible and compressible wall-bounded flows, including a discussion of the temporal and spatial problems, see Kleiser and Zang (1991).)

The first tentative steps were taken in the use of DNS to investigate transition to turbulence in supersonic, wall-bounded flows in the mid to late 1980s. Bayliss *et al.* (1985) presented the first DNS results for supersonic boundary-layer flow along a flat plate. These results were for spatially evolving, but two-dimensional, flow. The first three-dimensional DNS of a perturbed high-speed (Mach 4.5) flat-plate boundary-layer flow was accomplished by Erlebacher and Hussaini (1990). This numerical experiment used temporal DNS to examine boundary-layer stability, but stopped far short of attaining a transitional state.

Recently, due partly to increased supercomputer capacity, there have been many noteworthy three-dimensional simulations of compressible wall-bounded flows. Among these are temporal simulations by Normand and Lesieur (1992), Pruett and Zang (1992), Dinavahi and Pruett (1993), and Adams and Kleiser (1993); and spatial simulations by Thumm *et al.* (1990), Maestrello *et al.* (1991), Thumm (1991), Normand and Lesieur (1992), Eissler and Bestek (1993), Ng and Zang (1993), and Pruett and Chang (1993). Among these, the temporal simulation of Dinavahi and Pruett (1993) is unique in attaining a well-resolved fully turbulent state without recourse to modeling.

To date, with the exception of Rai and Moin (1991), virtually all of the numerical experiments cited have simulated controlled rather than natural instability processes. In a controlled experiment, instability waves of a particular wavelength (temporal) or frequency (spatial) are excited by imposed forcing. In contrast, in natural transition the input is random, and the flow itself selects the preferred instability modes. A few of the cited simulations are hybrid in the sense that the primary instability wave is imposed, whereas secondary instability is triggered by low-level noise. A distinguishing feature of high-speed boundary-layer flows is that multiple primary instability modes can coexist (Mack, 1984). The viscous first-mode instability, the counterpart of the Tollmien–Schlichting (TS) wave in incompressible flow, predominates in low-speed compressible flows. In hypersonic boundary-layer flows second-mode instabilities arise, which are acoustic in nature, and which eventually predominate as the Mach number increases. Thus far, all simulations of instability and transition in compressible flows have focused on first- and second-mode instabilities and their associated secondary instabilities, rather than on crossflow or Goertler modes.

Several observations gleaned from temporal DNS are worthy of note. Normand and Lesieur (1992) performed both DNS of a low-speed (Mach 0.5) compressible flat-plate flow and large-eddy simulation of a high-speed (Mach 5) flow. They observed transition to occur by means of fundamental secondary instability in the former case and subharmonic secondary instability in the latter case. Their findings are consistent with those of Pruett and Zang (1992), Dinavahi and Pruett (1993), and Adams and Kleiser (1993). Pruett and Zang (1992) and Dinavahi and Pruett (1993) considered the case of Mach 4.5 flow along a hollow cylinder (the axisymmetric analog of a flat-plate boundary layer) and observed subharmonic secondary instability triggered by second-mode primary instability to lead to transition. Adams and Kleiser (1993) performed a similar computation for a Mach 4.5 flat plate using random noise to trigger secondary instability from a base state perturbed by a second-mode disturbance. The secondary instabilities they observe are of subharmonic type and agree in growth rate and structure with the predictions of temporal secondary instability theory (Ng and Erlebacher, 1992). Moreover, despite the difference in geometry, their results are in qualitative agreement with those of Pruett and Zang (1992). A potential weakness of each of these simulations, however, is the failure to

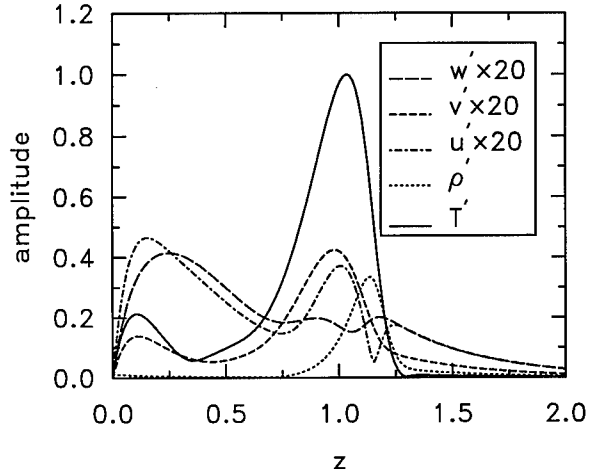


Figure 1. Amplitudes of components of oblique second-mode disturbance of $F = 2.094 \times 10^{-4}$ and $Re_L = 1013$ in Mach 6.8 boundary layer on 7° sharp cone.

account for growth of the boundary layer, a somewhat ambiguous task in the context of temporal theory. Recent experimental results (Stetson and Kimmel, 1993) and numerical results obtained from the parabolized-stability-equation (PSE) method (Chang, 1993) suggest that subharmonic secondary instability may not be the preferred path to transition in a growing high-speed boundary layer. The issue can probably only be resolved by spatial DNS, which incorporates the evolution of the boundary layer.

The temporal simulations cited above required upward of 10^6 grid points and consumed hundreds of Cray Y-MP CPU hours. There are several reasons for the great expense of computations of high-speed compressible flow relative to simulations of incompressible or subsonic flows:

1. The time discretizations in the compressible cases were fully explicit. In many instances the allowable time step was limited by the viscous stability condition rather than by the advection condition. For incompressible simulations the viscous stability limit is usually absent due to the conventional implicit treatment of the viscous terms.
2. The second-mode disturbances associated with high-speed transitional flows have a double-peaked structure (Figure 1) with amplitude peaks occurring both near the wall and the critical layer ($z \approx 1$ in Figure 1). In contrast to low-speed flows, at high speeds the critical layer lies far (approximately one displacement thickness) from the wall, necessitating concentrations of grid points in both regions of strong gradients.
3. At high speeds the growth rates of both the primary and secondary instabilities are much slower than for low-speed flows. This requires much longer time integrations.
4. In contrast to DNS of incompressible flow, flow-field oscillations due to inadequate resolution are potentially fatal in the compressible case since spurious negative densities, pressures, and/or temperatures can arise.

Relative to temporal DNS, spatial DNS is yet more computationally demanding, primarily because of the greater length of the computational domain. Nonetheless, the computational boundary-layer transition community has recently produced several spatial simulations of particular importance. The simulations of Thumm *et al.* (1990) examine the very early stages of secondary instabilities of both fundamental and subharmonic type in Mach 1.6 boundary-layer flows along a flat plate. Subsequently, Thumm (1991) turned his attention to investigating a new "oblique-mode" transition mechanism, again for Mach 1.6 flat-plate flow. Conventionally, transition is triggered by secondary instability originating from a finite-amplitude two-dimensional primary disturbance and a pair (or array) of low-amplitude oblique secondary disturbances. For Mach 1.6 boundary-layer flow, however, the most amplified linear instability turns out to be oblique and not two-dimensional, in contrast to the case for either incompressible flow or flow at very high Mach numbers. This suggests the possibility of triggering transition simply by the nonlinear interactions of a pair of symmetric unstable primary modes. Thumm (1991) presented an extensive set of results, comparing fundamental-, subharmonic-,

and oblique-breakdown scenarios. The simulations, which were carried into the early nonlinear stages of laminar breakdown, have recently been summarized by Fasel *et al.* (1993). Maestrello *et al.* (1991) performed three-dimensional spatial simulations of Mach 4.5 flows excited simultaneously by a two-dimensional second-mode disturbance and a single oblique disturbance of the same frequency. They computed to the early nonlinear stages of transition and demonstrated significant interactions between the forced modes, which then generated other rapidly growing instability modes. Eissler and Bestek (1993) performed several simulations at Mach 4.8 using periodic suction and blowing at the wall to excite instability waves. In addition to the excitation of the expected oblique second mode, their results showed excitation of an additional "viscous" mode of the same frequency but of different wavelength. The evolution of these modes was tracked from the first-mode region into the second-mode region.

Of these simulations, the typical spatial accuracy was fourth-order, occasionally with a spectrally accurate Fourier collocation method in the (periodic) spanwise direction. In most of these spatial simulations the spanwise resolution was modest, in some cases admitting just a single oblique mode. Although Thumm (1991) used up to 17 grid points in the spanwise direction, and Maestrello *et al.* (1991) used up to 32 spanwise grid points, such resolution is believed to be insufficient for the later stages of transition, in which there is typically an explosive broadening in wave space of the energy spectrum in the spanwise direction. The simulations at the higher Mach numbers call attention to the difficulties (and impracticality) of simulating the entire laminar-turbulent transition process when the dominant second-mode instabilities are of high frequency but slow growth. To begin from a linearly perturbed laminar state, the computational domain must be extremely long in streamwise extent (relative to the disturbance wavelength). Alternately, the forcing amplitudes must be quite large, in which case nonlinear interactions are significant at the inflow boundary and consistent inflow conditions are difficult to obtain.

This work focuses on the development of an algorithm and additional procedures for which spatial DNS of such challenging high-speed transition problems is feasible. With regard to the algorithm, its origins can be found in Ng and Zang (1993), who compared spatial DNS with secondary instability predictions for Mach 1.6 and Mach 6.8 flows in artificial, quasi-parallel boundary-layer flows. Their work validated both the basic spatial DNS code and the spatial secondary instability code, but it was not an investigation into the physics of transition. Their work, however, formed the starting point for the algorithm developed by Pruett and Chang (1993) for the spatial DNS computations and the results reported in this paper. Pruett and Chang (1993) made detailed comparisons of spatial DNS and PSE for two-dimensional linear and nonlinear second-mode disturbances in Mach 4.5 flat-plate boundary layers. They achieved remarkable agreement between the methods for these cases; however, they found that the numerical methods utilized in the DNS had to be extremely refined in order to obtain accurate results. Careful attention was given to many details often overlooked. Among the issues addressed were: obtaining self-consistent inflow conditions for nonparallel flows, the necessity of filtering to suppress spurious high-frequency modes and boundary reflections, obtaining reliable estimates for the numerical stability limits on the time step as a function of the precise spatial discretization, and the imposition of nonreflecting far-field and outflow boundary conditions.

Our present position is that the "grand challenge" of simulating transition in high-speed boundary-layer flows is best met by a combination of numerical tools. The PSE method is much more efficient than DNS for computing the early linear and weakly nonlinear stages of the transition process. Thus, we advocate the use of PSE to furnish accurate and consistent inflow conditions to a DNS that commences near the highly nonlinear laminar-breakdown stage. The primary objective of this paper is to provide thorough validation and documentation of the DNS algorithm. In the cross-validation of DNS with PSE, however, we demonstrate convincingly the fidelity of the PSE method within the appropriate flow regimes.

An alternative, but still developing approach, is that of large-eddy simulation (LES). In this method large-scale structures are resolved, but a model is employed for the subgrid-scale fluctuations. The LES approach is fairly well developed for incompressible flows (see Kleiser and Zang, 1991), but only a few results are available for supersonic flows (see Normand and Lesieur, 1992; Zang *et al.*, 1992; El-Hady *et al.*, 1993). Because the cost of PSE increases much faster than that of DNS as the number of spanwise modes is increased, PSE is limited in practice to investigations of narrow-band forcing. At present, LES appears to be the only hope for complete simulations of natural (broad-band)

transition. In the same way that the spatial DNS described herein has served to validate PSE, it is hoped that it will also be useful in validating LES approaches.

This paper consists of a reprise of the Pruett and Chang (1993) results, with an emphasis on the subtle numerical issues that are essential for accurate spatial DNS of high-speed boundary-layer flows. Their previous work is also extended to the simulation of three-dimensional second-mode disturbances propagating in the boundary layer of a sharp cone immersed in a Mach 8 flow. The motivation for this example is the stability experiment by Stetson *et al.* (1983), in which the second-mode disturbance was observed as the dominant instability in such a flow. The ultimate objective of this work, and the subject of the sequel to this paper, is the combined PSE/DNS investigation of the complete laminar-turbulent transition process in a hypersonic boundary-layer flow along a cone.

In the next section the three-dimensional compressible Navier-Stokes equations are presented for flow along a two-dimensional or an axisymmetric body. The fully explicit numerical method, which combines high-order compact-difference and spectral collocation methods, is presented in detail in Section 3. Algorithm details are discussed in Section 4. In Section 5 compressible linear stability theory (LST) and the PSE method are discussed very briefly, and the DNS code is thoroughly validated against these yardsticks. Three of the four validation cases examine the evolution of two-dimensional second-mode instability waves in a Mach 4.5 flat-plate boundary-layer flow. Both linear and nonlinear disturbance amplitudes are considered. The fourth case examines the evolution of a pair of oblique second-mode disturbances on a sharp 7° half-angle cone in a Mach 6.8 (free-stream Mach 8) flow. Conclusions which relate both to the numerical method and to transition physics are presented in the final section.

2. Governing Equations

Consider the body-fitted orthogonal coordinate system $\mathbf{x} = [x, \theta, z]^T$ on an axisymmetric body as shown in Figure 2, where x is the arc length along the body, θ is the azimuthal angle, and z is the coordinate normal to the body. Associated with \mathbf{x} is the fundamental metric tensor g_{mn} , which has the nonzero components

$$g_{11} = s^2, \quad g_{22} = r^2, \quad g_{33} = 1, \quad (1)$$

where

$$r(x, z) = R + z \cos \varphi, \quad (2)$$

$$s(x, z) = 1 - z \frac{d\varphi}{dx},$$

and where $R(x)$ and $\varphi(x)$ are the body radius and the angle of the surface tangent in the plane of symmetry, respectively. For convenience, we define the following partial differential operators, which incorporate the metric quantities r and s :

$$D_x^0 u \equiv \frac{1}{s} \frac{\partial u}{\partial x}, \quad D_\theta^0 u \equiv \frac{1}{r} \frac{\partial u}{\partial \theta}, \quad D_z^0 u \equiv \frac{\partial u}{\partial z}, \quad D_x^1 u \equiv \frac{1}{rs} \frac{\partial(ru)}{\partial x}, \quad D_z^1 u \equiv \frac{1}{rs} \frac{\partial(rsu)}{\partial z}. \quad (3)$$

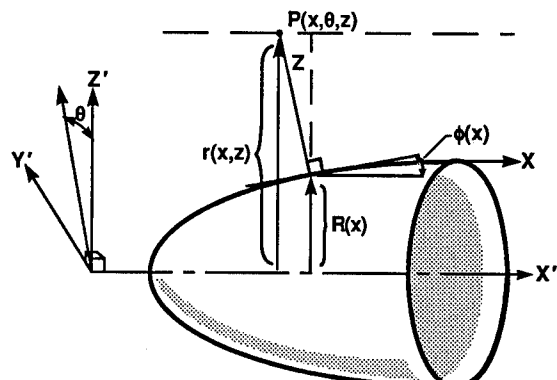


Figure 2. Body-fitted coordinate system on axisymmetric body.

In the coordinate system of Figure 2 and in the terminology of (3), the dimensionless compressible Navier-Stokes equations assume the following conservative form:

$$\frac{\partial \mathbf{Q}}{\partial t} + D_x^1 \mathbf{E} + D_\theta^0 \mathbf{F} + D_z^1 \mathbf{G} + \mathbf{H} = \mathbf{0}, \quad (4)$$

where $\mathbf{Q} = [\rho, \rho u, \rho v, \rho w, E_t]^T$ is the fluid state vector of conserved quantities; ρ is the density; u , v , and w are velocities in the \mathbf{e}_x , \mathbf{e}_θ , and \mathbf{e}_z directions, respectively; and E_t is the total energy. For later use, we also define the vector of primitive variables $\mathbf{U} = [\rho, u, v, w, p]^T$, and, for state and flux vectors in general, $\mathbf{Q} = [Q_0, Q_1, Q_2, Q_3, Q_4]^T$, etc. Vectors \mathbf{E} , \mathbf{F} , \mathbf{G} , and \mathbf{H} are defined as follows:

$$\begin{aligned} \mathbf{E} &= \begin{bmatrix} \rho u \\ \rho uu - \tau_{11} - p \\ \rho uv - \tau_{12} \\ \rho uw - \tau_{13} \\ (E_t + p)u - ut_{11} - vt_{12} - wt_{13} - h_1 \end{bmatrix}, \\ \mathbf{F} &= \begin{bmatrix} \rho v \\ \rho vu - \tau_{21} \\ \rho vv - \tau_{22} - p \\ \rho vw - \tau_{23} \\ (E_t + p)v - ut_{21} - vt_{22} - wt_{23} - h_2 \end{bmatrix}, \\ \mathbf{G} &= \begin{bmatrix} \rho w \\ \rho wu - \tau_{31} \\ \rho wv - \tau_{32} \\ \rho ww - \tau_{33} - p \\ (E_t + p)w - ut_{31} - vt_{32} - wt_{33} - h_3 \end{bmatrix}, \\ \mathbf{H} &= \begin{bmatrix} 0 \\ -\frac{\sin \varphi}{r} F_2 - (D_x^0 \varphi) E_3 \\ \frac{\sin \varphi}{r} F_1 + \frac{\cos \varphi}{r} F_3 \\ -\frac{\cos \varphi}{r} F_2 + (D_x^0 \varphi) E_1 \\ 0 \end{bmatrix}, \end{aligned} \quad (5)$$

where p is thermodynamic pressure,

$$\begin{aligned} h_1 &= \frac{\kappa}{(\gamma - 1) M_r^2 Re} D_x^0 T, \\ h_2 &= \frac{\kappa}{(\gamma - 1) M_r^2 Re} D_\theta^0 T, \\ h_3 &= \frac{\kappa}{(\gamma - 1) M_r^2 Re} D_z^0 T \end{aligned} \quad (6)$$

are the heat flux components, T is the temperature, κ is the thermal conductivity,

$$\tau_{ij} = \frac{2\mu}{Re} \sigma_{ij} - \frac{2}{3} \frac{\mu}{Re} \delta_{ij} d \quad (7)$$

is the stress tensor, μ is the dynamic viscosity, δ_{ij} is the Kronecker delta, $d = D_x^1 u + D_\theta^0 v + D_z^1 w$ is the divergence of the velocity (dilatation), and σ_{ij} is the symmetric rate-of-deformation tensor with

components

$$\begin{aligned}\sigma_{11} &= D_x^0 u - w D_x^0 \varphi, \\ \sigma_{22} &= D_\theta^0 v + \frac{u \sin \varphi}{r} + \frac{w \cos \varphi}{r}, \\ \sigma_{33} &= D_z^0 w, \\ \sigma_{12} = \sigma_{21} &= \frac{1}{2} \left(D_\theta^0 y + D_z^0 v - \frac{v \sin \varphi}{r} \right), \\ \sigma_{13} = \sigma_{31} &= \frac{1}{2} (D_x^0 w + D_z^0 u - u D_x^0 \varphi), \\ \sigma_{23} = \sigma_{32} &= \frac{1}{2} \left(D_\theta^0 w + D_z^0 v - \frac{v \cos \varphi}{r} \right).\end{aligned}\quad (8)$$

With the exception of (1), which refers to a covariant tensor, all other equations refer to physical vector or tensor components. Thus, for convenience and brevity, we adopt a loose notation of referencing physical components by subscripts.

The components of vector (4) define, respectively, conservation of mass, conservation of momentum in the three dimensions, and conservation of energy. The governing system is closed by the equation of state. For this work, we assume that the fluid is air and behaves as a perfect gas, whereby

$$\gamma M_r^2 p = \rho T, \quad (9)$$

$$E_t = \frac{p}{\gamma - 1} + \frac{\rho}{2} (u^2 + v^2 + w^2), \quad (10)$$

and $\kappa = \mu/Pr$.

Four dimensionless parameters emerge from nondimensionalization: Mach number, Reynolds number, Prandtl number, and the ratio of specific heats, defined, respectively, as follows:

$$M_r = \frac{u_r^*}{\sqrt{\gamma R_g^* T_r^*}}, \quad Re = \frac{\rho_r^* u_r^* \delta_{in}^*}{\mu_r^*}, \quad Pr = \frac{C_p^* \mu_r^*}{\kappa_r^*}, \quad \gamma = \frac{C_p^*}{C_v^*}, \quad (11)$$

where R_g^* , C_p^* , and C_v^* are the ideal gas constant and the specific heats at constant pressure and constant volume, respectively. Throughout this work, dimensional quantities are denoted by asterisk, reference values are denoted by a subscript “r”, $Pr = 0.7$, and $\gamma = 1.4$. In the nondimensionalization from which (4) arises, the reference values for density, velocities, and temperature, ρ_r^* , u_r^* , and T_r^* , respectively, are arbitrary. Pressure is scaled by $\rho_r^* u_r^{*2}$. Viscosity is normalized by the viscosity at the reference temperature and is assumed to vary according to Sutherland’s law. In dimensionless form

$$\mu = \frac{T^{3/2}(1+C)}{T+C}, \quad C = \frac{110.3 \text{ K}}{T_r^*}. \quad (12)$$

Throughout this paper, a subscript “e” denotes a value at the boundary-layer edge, and lengths are scaled by the boundary-layer displacement thickness at the inflow boundary δ_{in}^* , where, in general (White, 1974),

$$\delta^* \left(1 + \frac{\delta^*}{2R^*} \right)^b = \int_0^\infty \left(\frac{r^*}{R^*} \right)^b \left(1 - \frac{\rho^* u^*}{\rho_e^* u_e^*} \right) dz^*, \quad b = \begin{cases} 0, & \text{two-dimensional,} \\ 1, & \text{axisymmetric.} \end{cases} \quad (13)$$

For comparison with results obtained from spatial LST and the PSE method, we define the boundary-layer length scale as

$$L^* \equiv \sqrt{\frac{\mu_e^* x^*}{\rho_e^* u_e^*}}, \quad (14)$$

and we denote the Reynolds number based on edge conditions and L^* as Re_L . For comparisons with experiments, it is also useful to define Re_x , the Reynolds number based on x^* , whereby $Re_x = (Re_L)^2$.

With proper interpretation, (4) is valid for either two-dimensional or axisymmetric bodies. The two-dimensional case is recovered as $r \rightarrow 1$ in (3) and $1/r \rightarrow 0$ in H (5).

A nonconservative, but computationally useful, alternative form of the energy equation is

$$\begin{aligned} Q_4 &= p, & E_4 &= pu, & F_4 &= pv, & G_4 &= pw, \\ H_4 &= \Phi - (\gamma - 1)p\nabla \cdot \mathbf{u}, & \Phi &\equiv \sigma_{ij}\tau_{ij}, \\ \nabla \cdot \mathbf{u} &\equiv D_x^1 u + D_\theta^0 v + D_z^1 w, \end{aligned} \quad (15)$$

where repeated indices imply summation. In subsequent discussions we refer to (15) as the “pressure equation” as distinguished from the “energy equation.”

Mathematically, DNS is the numerical solution of an Initial-Boundary-Value Problem (IBVP). For spatial DNS, inflow and outflow boundary conditions are required. The imposition of initial and boundary conditions is discussed more fully in the next section.

3. Numerical Method

Navier-Stokes codes fall roughly into two classes depending upon the application: aerodynamic codes, in which body geometry is usually complicated, but from which one typically wants to extract only mean quantities such as surface pressure, lift, and drag; and DNS codes, in which body geometry is simple, but from which one wants to compute fine details of the flow field, ideally, to the smallest scales. Usually, aerodynamic codes are of relatively low-order accuracy, and, to capture shocks, they impose significant artificial dissipation through some form of upwinding. Often the boundary layer is severely underresolved, a deficiency partially atoned for by the use of transition or turbulence models. In contrast, in DNS, for which the boundary layer is the primary focus, dissipation and dispersion errors must be minimized if the growth rates and phase speeds of instability waves are to be computed accurately.

In this section, we present a fully explicit method designed specifically for the DNS of instability and transition in high-speed boundary-layer flows. The flow region of interest is downstream of the bow shock, and it is an implicit assumption that there are no shocks in the domain. To minimize dissipation and dispersion errors, we rely on a combination of spectral methods and high-order central compact-difference approximations for spatial derivatives. In the development of the algorithm, accuracy, efficiency, and simplicity, in that order, have been our guiding criteria.

Spatial Discretizations

We consider the physical domain and grid points defined by

$$\begin{aligned} x_{\text{in}} &\leq x_i \leq x_{\text{out}}, & i &= 0, \dots, N_x, \\ 0 &\leq \theta_j \leq \frac{2\pi}{n}, & j &= 0, \dots, N_\theta, \\ 0 &\leq z_k \leq z_{\text{max}}, & k &= 0, \dots, N_z. \end{aligned} \quad (16)$$

Let u_{ijk} be the discrete approximation of $u(x_i, \theta_j, z_k)$, etc., and, for the moment, assume that grid points are equally spaced in terms of their respective coordinates. For DNS of axisymmetric (two-dimensional) boundary layers, it is conventional and physically reasonable to assume that the flow is periodic in the azimuthal (spanwise) direction. This periodicity permits the exploitation of spectral collocation methods (e.g., Canuto *et al.*, 1988) based on finite series expansions of the flow quantities in terms of Fourier basis functions, as, for example,

$$u(\mathbf{x}, t) = \sum_{j=-N_\theta/2}^{N_\theta/2} \hat{u}_j(x, z, t) \cdot \exp\{ijn\theta\}, \quad (17)$$

where $i = \sqrt{-1}$. Collectively, the Fourier coefficients \hat{u}_j provide the Fourier spectrum, an intrinsic measure of the adequacy of resolution. The integer n , which appears in (16) and (17), is a parameter of the flow that defines the period in the azimuthal direction and is related to the azimuthal wave

number β through the relation

$$n = \beta r = \beta_0 R_0, \quad R_0 \equiv R(x_{in}). \quad (18)$$

(For bodies on which the radius changes, such as a cone, (18) implies that the wave number of oblique (helical) waves evolves with x .) We implement the collocation method in the conventional pseudo-spectral manner. That is, derivatives with respect to θ of the truncated series in (17) are evaluated exactly in Fourier space, whereas nonlinear terms of the governing equations are evaluated in physical space. Vectorized fast Fourier transforms (FFTs) are used to shuttle efficiently between the transform and physical spaces. If desired, aliasing errors are controlled by spectral truncation. For computational efficiency, an option exists in the code to enforce symmetry about the plane $\theta = 0$, in which case odd (e.g., v) and even (e.g., u) functions are expanded in sine and cosine series, respectively, rather than in complex exponential series. As expected, there is roughly a factor of 2 reduction in computational effort with symmetry enforced.

The proper spectral expansion for a two-dimensional, rather than an axisymmetric, body is recovered from (17) by defining the azimuthal arc length $y = r\theta$ and by using (18).

For spatial DNS, both the streamwise and wall-normal directions are aperiodic, which precludes the use of Fourier spectral methods. In the aperiodic directions our DNS code allows a variety of differentiation options. Among these are a Chebyshev spectral-collocation scheme and several members from a class of fourth-order and sixth-order central compact-difference schemes (Lele, 1990; Carpenter *et al.*, (1991)). For explicit time advancement, the Chebyshev spectral method is subject to an extremely severe restriction on the time step of the form $\Delta t \sim 1/N_z^4$, which renders the method impractical for long-time integrations. Nevertheless, the method is useful for diagnostic purposes. In particular, it permits us to compute the Chebyshev spectrum as an indicator of the adequacy of resolution.

In the context of fully explicit time advancement, derivatives are computed by means of compact-difference techniques as follows:

$$M \mathbf{u}_z = E \mathbf{u}, \quad (19)$$

where M is a tridiagonal matrix, E is a banded matrix, and the vector \mathbf{u}_z , for example, contains the discrete approximation of $\partial u / \partial z$. Matrices M and E are referred to as the implicit and explicit operators, respectively. For the fourth-order Pade method, E is tridiagonal. For sixth-order methods, it is usually pentadiagonal. Compact-difference operators are thus of the form $C = M^{-1}E$ and are global (dense matrices).

An area of active research concerns stable boundary closures for compact-difference methods. In general, stencils are modified in the vicinity of boundaries, which results in some loss of formal accuracy. It is well known (Gustafsson, 1975) that, for a hyperbolic system of equations, a scheme of h th order closure can retain global formal accuracy of order $h + 1$ at best. In distinguishing between various schemes, we adopt the nomenclature of Carpenter *et al.* (1991). For example, 3,4–6–4,3 refers to a scheme that is of sixth-order accuracy at interior node points, fourth-order accuracy at nodes 1 and $N_z - 1$, and third-order accuracy at nodes 0 and N_z . Recently, Carpenter *et al.* (1991) have developed a 5,5–6–5,5 scheme which retains global sixth-order accuracy. It evaluates derivatives at the boundary points and at immediately adjacent points by fully explicit eight-point stencils. Among the schemes which we have tried and for which options exist in the DNS code are the 3–4–3 (Pade), 3,4–6–4,3 (Lele), and 5,5–6–5,5 (Carpenter *et al.*) schemes. The reader is referred to Lele (1990) and Carpenter *et al.* (1991) for details, including the coefficients of matrices M and E . These options exist for differentiation in both the streamwise and wall-normal directions. To date we have been unable to maintain numerical stability whenever fifth-order boundary closure is implemented in both the x and the z directions. Our most accurate results exploit the method of Carpenter *et al.* in the streamwise direction and the 3,4–6–4,3 method of Lele in the wall-normal direction.

All differentiation operators assume that grid points are equally spaced in computational space. Analytic functions, described in detail later, are used to map from computational space onto physical space, where the grid may be highly stretched. Metrics of the transformation are incorporated directly into the differentiation operators.

Time Advancement

To be practical, an explicit DNS algorithm must provide long-time temporal accuracy while requiring modest temporary storage. Unless excruciatingly well resolved in time, we believe that second-order schemes lack sufficient accuracy for DNS. Attempts to gain higher-order accuracy through multistep methods violate the latter practical constraint. An elegant compromise is afforded by the use of one of the family of third-order low-storage Runge–Kutta methods proposed by Williamson (1980). To implement the Runge–Kutta scheme, we cast the governing equations in the following form:

$$\frac{\partial \mathbf{Q}}{\partial t} = \mathbf{V}, \quad (20)$$

$$\mathbf{V} \equiv -D_x^1 \mathbf{E} - D_y^0 \mathbf{F} - D_z^1 \mathbf{G} - \mathbf{H}.$$

Time advancement of the discrete version of (20) is accomplished in physical space. Such schemes are now in wide use, and so we omit details.

An important peripheral issue for DNS concerns the determination of a limit on the time step Δt , for which the time-advancement scheme remains stable, but which is not unnecessarily restrictive. For parameter values typical of high-speed boundary-layer flows, advection and viscous constraints on the time step are of the same order of magnitude. Moreover, if the flow is transitional, determination of an appropriate time step is complicated by localized large-scale velocity and temperature fluctuations. Consequently, we have chosen to estimate the stability limit dynamically so as to maintain the time step continually near its maximum allowable size. Specifically, we require

$$\max(\lim_1, \lim_2) \cdot \Delta t < sf,$$

$$\lim_1 = (\lim_a^2 + \lim_\mu^2)^{1/2}, \quad (21)$$

$$\lim_2 = (\lim_a^2 + \lim_\kappa^2)^{1/2},$$

where $0 < sf < 1$ is the stability limit safety factor (typically $sf = 0.95$), and where \lim_a , \lim_μ , and \lim_κ are limiting values obtained by independent consideration of the stability of model linear advection, viscous diffusion, and thermal diffusion equations, respectively. For example, to evaluate the advection limit, we consider the linear transport equation

$$q_t + (|u| + c)q_x + (|v| + c)q_y + (|w| + c)q_z = 0. \quad (22)$$

The coefficients u , v , and w are obtained from the instantaneously “frozen” velocity fields of the true problem. Similarly, the speed of sound $c = \sqrt{\gamma p/\rho}$ is computed from the “frozen” density and pressure of the true problem. The integration of (22) is stable provided

$$\Delta t \cdot \lim_a < 1, \quad (23)$$

$$\lim_a = \max_{ijk} \left[\frac{(|u| + c)_{ijk}}{cfl_x \Delta x_i} + \frac{(|v| + c)_{ijk}}{cfl_y \Delta y_j} + \frac{(|w| + c)_{ijk}}{cfl_z \Delta z_k} \right],$$

where $\Delta x_i \equiv x_i - x_{i-1}$, etc. The Courant–Friedrichs–Levy (CFL) limits cfl_x , cfl_y , and cfl_z depend upon both the method of temporal advancement and the eigenvalue spectrum of the discrete spatial operator exploited in the x , y , and z dimensions, respectively. Table 1 presents the stability limits of a variety of spatial operators for the one-dimensional linear advection (wave) equation integrated in time by a third-order Runge–Kutta (RK3) scheme. Some of these limits have been derived by rigorous

Table 1. Courant–Friedrichs–Levy (CFL) limit $|a(\Delta t/\Delta x)| < cfl$ for the scalar linear advection equation $q_t + aq_x = 0$.

Spatial operator	Stability limit cfl	Method of derivation
Compact fourth order	1.0	Empirical
Compact sixth order	$\sqrt{3}/2$	Analytical
Fourier spectral	$\sqrt{3}/\pi$	Analytical
Chebyshev spectral	$5(\sqrt{3}/\pi)$	Empirical

Table 2. Viscous stability limit $|v(\Delta t/\Delta x^2)| < vl$ for the scalar diffusion equation $q_t = vq_{xx}$.

Spatial operator	Stability limit vl	Method of derivation
Compact fourth order	2.51/3	Empirical
Compact sixth order	2.51/4	Empirical
Fourier spectral	2.51/ π^2	Analytical
Chebyshev spectral	2(2.51/ π^2)	Empirical

eigenvalue analyses and are so noted. Others have been established empirically by numerical experimentation with the time step, in which cases the scheme “blows up” whenever the time step exceeds the value given. For the Fourier spectral and finite-difference schemes, the stability limits are sharp. For the Chebyshev spectral scheme, the limit was harder to evaluate empirically because of the less explosive nature of the numerical instability; hence, we urge some caution in the use of the value presented.

Similarly, \lim_μ and \lim_a are defined by considering model diffusion equations of the form

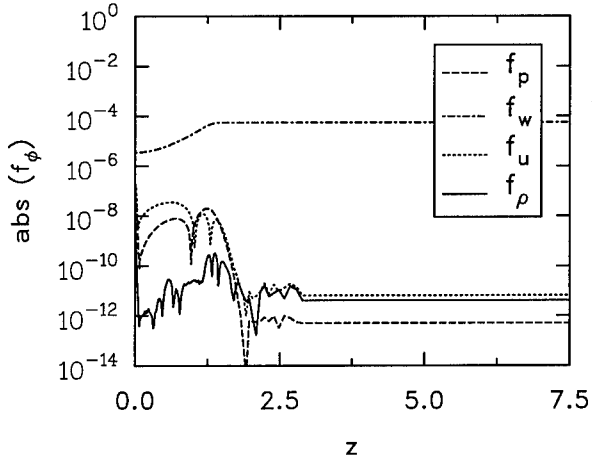
$$q_t = \frac{v}{Re} \nabla^2 q, \quad v \in \left\{ \frac{\mu}{\rho}, \frac{\kappa}{\rho} \right\} \quad (24)$$

with the help of Table 2. The domain of absolute stability for third-order Runge–Kutta methods can be found in many references including Canuto *et al.* (1988). The factors of 2.51 and $\sqrt{3}$ which arise in Tables 2 and 1, respectively, pertain to the intercepts of the RK3 stability boundary with the real and imaginary axes, respectively. The stability of a diffusion problem is limited by the value -2.51 of the real-axis intercept, whereas the stability of an advection problem is limited by the values $\pm\sqrt{3}$ of the imaginary-axis intercepts. We conjecture that solutions of problems of mixed advection-diffusion type remain stable provided, say, the point $(-2.51 \cdot \lim_\mu, \sqrt{3} \cdot \lim_a)$ lies within the RK3 domain of absolute stability. Equation (21) is a convenient approximation to this criterion based on the fact that a half-ellipse through the real and imaginary intercepts lies entirely within this region.

The numerical stability of semidiscrete and fully discrete compact-difference schemes is subtle and, as mentioned previously, is currently an area of active research (Carpenter *et al.*, 1991). In general, what is true for scalar equations is not necessarily true for systems. Our method of estimating stability limits is somewhat heuristic, but it has proved a useful guideline in practical applications for a wide variety of numerical methods and over a wide range of parameter values. For the range of parameter values of the test cases in Section 5, approximately 1000 time steps per disturbance period suffice to maintain numerical stability.

Initial Condition

We obtain the initial (“basic”) flow state \mathbf{Q}^0 , which is assumed to be two-dimensional or axisymmetric, from the spectrally accurate boundary-layer (BL) code described in Pruett and Streett (1991) and Pruett (1993). Velocity and temperature profiles provided by this code are smooth nearly to machine precision. Either isothermal or adiabatic wall cases can be computed by the BL code. The present results assume that the wall is adiabatic. Because the boundary-layer equations neglect terms of order $1/Re_L$ and higher, a small residual remains when the boundary-layer solution is injected into the steady Navier–Stokes equations. Without special treatment, this numerical error introduces transients into the domain that may contaminate the Fourier analysis of the flow field. There are two philosophies for treating the initial residual. The governing equations can be integrated in time (relaxed) from the initial guess until the residual becomes arbitrarily small (in practice, on the order of machine zero). Unfortunately, for an explicit code, the computation of a clean steady state may require a greater computational effort than the computation of the perturbed flow of interest, since numerical errors may mimic slowly traveling physical waves. Alternately, small source terms can be subtracted from the governing equations to cancel the initial residual exactly (Erlebacher and Hussaini, 1990). To conserve computational resources, we adopt the latter method. For the parameter



7.5 **Figure 3.** Components of source term $\mathbf{f} = [f_\rho, f_u, 0, f_w, f_p]^T$ subtracted from Navier-Stokes equations to cancel steady-state residual of base flow.

values of Cases 2 and 3 of Section 5, Figure 3 compares the magnitude of the components of the source term \mathbf{f} that are subtracted from the continuity, u and w momentum, and pressure equations at the inflow station. The source term is small, but most significant, in the wall-normal momentum equation, where the slight transverse pressure gradient is neglected by the boundary-layer equations. An advantage of this approach is that it facilitates direct comparisons with LST and PSE analyses, both of which assume inherently that the base state is steady and simultaneously satisfies the governing equations.

For the presentation of results, it is often useful to display only the disturbance fields, which we denote by primes. That is, $\mathbf{Q}' \equiv \mathbf{Q} - \mathbf{Q}^0$ and similarly for individual components.

Boundary Conditions

As any practitioner of spatial DNS will acknowledge, the specification of boundary conditions for inflow-outflow problems is a delicate matter. The reader is referred to Nordstrom (1989) and Poinsot and Lele (1992) for detailed discussions of the issues involved. For Navier-Stokes calculations, all flow quantities can be specified at the inflow boundary. The prescription of the inflow condition depends upon the method by which disturbances are introduced into the flow. To date, spatial DNS calculations have introduced forcing either through a time-periodic inflow condition (e.g., originated, we believe, by DeSanto and Keller, (1962)) or through a time-periodic wall boundary condition (e.g., Kral, 1988; Thumm, 1991). For stability calculations, the difficulty with the latter method is that it is never known precisely what disturbances are generated. Indeed, in high-speed boundary-layer flows, it appears that multiple modes at the same frequency can be generated by periodic suction and blowing at the wall (Eissler and Bestek, 1993). Therefore, we favor the former approach. At the inflow boundary $x = x_{in}$, the flow is specified as the superposition of the steady two-dimensional or axisymmetric base flow and a temporally periodic fluctuation of frequency ω , amplitude ϵ , streamwise wave number α , and spanwise (azimuthal) wave number β as follows:

$$\mathbf{Q}(x_{in}, y, z, t) = \mathbf{Q}^0(x_{in}, z) + \epsilon \exp[i(\alpha x_{in} + \beta y) - \omega t] \Psi(z) + c.c. \quad (25)$$

To minimize temporal transients, ϵ is ramped smoothly to its maximum value over an interval of time (typically one disturbance period). The disturbance structure, which is contained in the complex vector Ψ , is obtained either from spatial LST (Ng and Zang, 1993) or from PSE theory as in Chang *et al.* (1991). In either case the disturbance is normalized so that the maximum amplitude of the temperature fluctuation is unity. For high-speed flows, the disturbances derived from the parallel (LST) and nonparallel (PSE) theories are significantly different, as shown in Figure 4, and the disparity tends to increase with x and with Mach number. For developing (nonparallel) high-speed boundary-layer flows, the use of LST-derived forcing results in a significant inconsistency at the inflow boundary, which manifests itself in undesirable streamwise transients downstream of the inflow boundary.

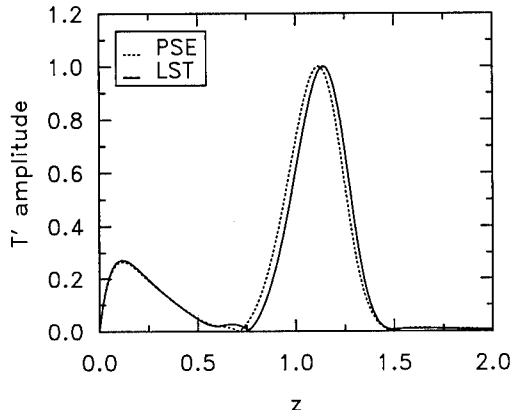


Figure 4. Amplitude of temperature component of linear disturbance at $Re_L = 700$ from parallel (LST) and nonparallel (PSE) theories.

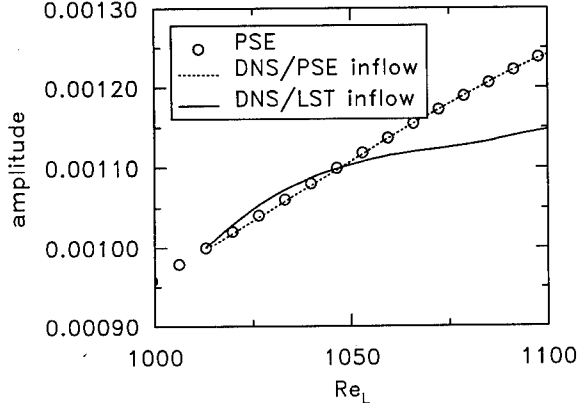


Figure 5. Transients downstream of inflow boundary for Case 4 of Section 5.

Moreover, if the amplitude of the disturbance is large enough, a weak Mach wave can be seen emanating from the inflow boundary near the critical layer. It is therefore important that nonparallel effects be considered. We have found PSE-derived forcing functions virtually to eliminate inflow inconsistencies, as shown in Figure 5, which presents the evolution of the temperature maximum in the region near the inflow boundary for Case 4 in Section 5. In contrast, the wandering of the temperature maximum away from the nearly constant-slope DNS/PSE curve for the DNS/LST case is symptomatic of the inconsistency between the parallel LST theory and the nonparallel DNS calculation.

For reference, the amplitudes of each of the five components Ψ of an oblique second-mode disturbance in a Mach 6.8 boundary-layer flow on a cone are shown in Figure 1, having been obtained from the nonparallel PSE method for parameter values which correspond to Case 4 in Section 5. Note the domination of the temperature and density components of the disturbance.

In the vicinity of the outflow boundary, we have found a buffer domain, proposed by Streett and Macaraeg (1989/90), to be effective in passing large-amplitude fluctuations with minimal reflection and upstream influence. Within the buffer region, the governing system of equations is gradually modified as follows:

1. Streamwise viscous terms are smoothly attenuated to zero to parabolize the governing system.
2. The base streamwise velocity profile is smoothly brought to that of a uniform flow at the velocity of the free stream to ensure that all characteristics lead out of the domain.
3. The source term f discussed previously is modified significantly in the buffer region to balance the changes to the basic flow.

With these changes, flow quantities along the outflow boundary can be extrapolated from the interior.

At the wall, the usual no-slip conditions are imposed on the velocities (except within the buffer region). Temperature is assumed to be fixed at its adiabatic value. (The rationale for the hybridization of the adiabatic and Dirichlet wall condition on temperature is addressed in an article by Pruett and Zang (1992) in a previous issue of this journal.) No condition is imposed on density; its value is determined directly from the governing equations at the wall. Pressure at the wall is derived from density and temperature via the equation of state.

At the far-field boundary ($z = z_{\max}$), we adapt the nonreflecting boundary conditions proposed by Thompson (1987), which are based in inviscid characteristic theory. Here, these are applied only to the disturbance field $\mathbf{U}' \equiv \mathbf{U} - \mathbf{U}^0$ in the following way. Adding and subtracting formally identical quantities from the right-hand side of (20), we obtain

$$\frac{\partial \mathbf{Q}}{\partial t} = \mathbf{V} - \frac{\partial \mathbf{G}'}{\partial z} + \frac{\partial \tilde{\mathbf{G}}'}{\partial z}, \quad (26)$$

where

$$\frac{\partial \mathbf{G}'}{\partial z} \equiv \frac{\partial \mathbf{G}}{\partial \mathbf{U}} \frac{\partial \mathbf{U}'}{\partial z}. \quad (27)$$

Recognizing that

$$\frac{\partial \mathbf{Q}}{\partial t} = \frac{\partial \mathbf{Q}}{\partial \mathbf{U}} \frac{\partial \mathbf{U}}{\partial t}$$

and exploiting the notation $A = \partial \mathbf{Q} / \partial \mathbf{U}$ and $B = \partial \mathbf{G} / \partial \mathbf{U}$, we temporarily recast (26) in terms of \mathbf{U} as follows:

$$\frac{\partial \mathbf{U}}{\partial t} = A^{-1} \mathbf{V} - (S - \tilde{S}) \frac{\partial \mathbf{U}'}{\partial z}, \quad (28)$$

where $S \equiv A^{-1}B$, and \tilde{S} has yet to be defined. Matrix S is then diagonalized by the similarity transformation $S = P\Lambda P^{-1}$, where Λ is the diagonal matrix with eigenvalues $\lambda_m \in \{w - c, w, w, w, w + c\}$ in the order shown. Positive and negative eigenvalues correspond to outbound and inbound characteristics, respectively. Now let $\tilde{S} = P\tilde{\Lambda}P^{-1}$, where $\tilde{\Lambda}$ is the diagonal matrix with eigenvalues $\tilde{\lambda}_m = \max(\lambda_m, 0)$. Writing (28) once again in terms of \mathbf{Q} , we obtain our working form

$$\frac{\partial \mathbf{Q}}{\partial t} = \mathbf{V} - AP[\Lambda - \tilde{\Lambda}]P^{-1} \left[\frac{\partial \mathbf{U}}{\partial z} - \frac{\partial \mathbf{U}^0}{\partial z} \right]. \quad (29)$$

Note that if $\mathbf{U} = \mathbf{U}^0$, or if all eigenvalues of Λ are nonnegative, then there is no change to the right-hand side vector \mathbf{V} . If, however, there are disturbances traveling inbound at the far-field boundary, their time derivatives are set to zero on the boundary.

Mappings

As shown in Figure 1, the eigenfunction of a second-mode disturbance in a high-speed boundary-layer flow has a double structure in which the temperature component is sharply peaked near the wall and the critical layer. Consequently, accuracy and resolution considerations necessitate that grid points be clustered in both regions of sharp gradients. For this purpose, we use a highly tuned mapping from the computational space to the physical space. The mapping is adapted from Erlebacher and Hussaini (1990) and combines gradual exponential stretching away from the wall with clustering in the vicinity of the critical layer. In computational space, for $k = 0, 1, \dots, N_z$,

$$\xi_k = \begin{cases} -1 + \frac{2k}{N_z}, & \text{compact difference,} \\ \cos\left(\frac{k\pi}{N_z}\right), & \text{Chebyshev spectral.} \end{cases} \quad (30)$$

For the compact-difference schemes, note that grid points are equally spaced in computational space. There are five parameters for the mapping: z_{\max} , $z_{1/2}$, z_0 , Δz , and τ . The following transcendental equation maps the interval $[-1, +1]$ in computational space onto itself and performs a clustering of grid points of strength τ and width Δz about the point z_0 :

$$\zeta + \tau \tanh\left[\frac{\zeta - \zeta_0}{\Delta \zeta}\right] = \frac{\xi - \xi_0}{\Delta \xi}, \quad -1 \leq \xi \leq +1. \quad (31)$$

The subsequent exponential transformation below maps the computational interval $[-1, +1]$ onto the physical interval $[0, z_{\max}]$:

$$\begin{aligned} z(\zeta) &= z_{\max} \left[\frac{a^{(\zeta+1)} - 1}{a^2 - 1} \right], \quad -1 \leq \zeta \leq +1, \\ a &= \frac{z_{\max} + \sqrt{z_{\max}^2 - 4z_{1/2}(z_{\max} - z_{1/2})}}{2z_{1/2}}. \end{aligned} \quad (32)$$

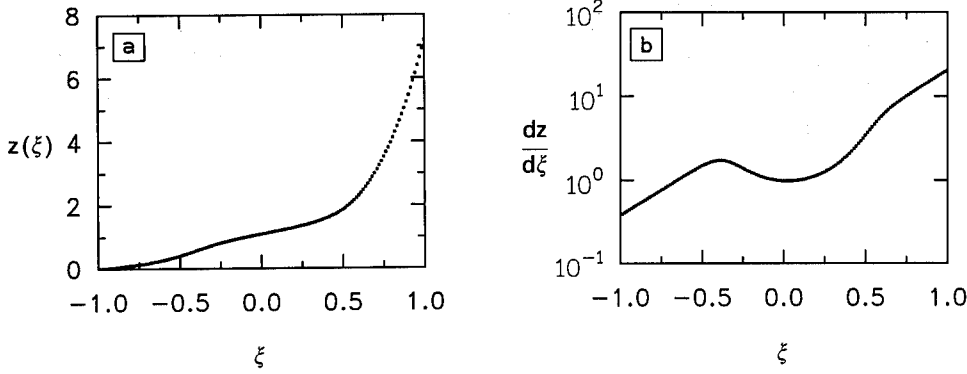


Figure 6. Wall-normal (a) mapping and (b) associated metric.

The four remaining unknown quantities in (31) are determined by requiring

$$z(\zeta_0) = z_0, \quad \Delta\zeta = \frac{d\zeta}{dz} \cdot \Delta z, \quad \zeta(-1) = -1, \quad \zeta(+1) = +1. \quad (33)$$

If $\tau = 0$, there is no clustering about z_0 , in which case exactly half of the grid points lie between the wall and $z_{1/2}$. We find (32) to be superior to the bilinear fractional transformation used originally by Erlebacher and Hussaini (1990), which stretches too fast in the far field. Figure 6 shows the grid-point distribution and metric for the parameter values of Mach 4.5 in Cases 2 and 3 in Section 5. In practice, we tune the number of grid points and mapping parameters by use of the temporal DNS code of Pruett and Zang (1992). More specifically, we adjust the resolution and mapping parameters until we are able to recover local (global) disturbance growth rates from the DNS that are in four (six) place agreement with eigenvalues obtained from temporal LST.

Similarly, a streamwise mapping can be used to concentrate points downstream where nonlinear interactions lead to a broadening of the spectrum in wave space. For this paper, however, all results were obtained with grid points equally spaced in x .

In spatial DNS the boundary layer thickens as x increases. Eventually, the mapping described above will become detuned, and the far-field boundary at z_{\max} will pinch the flow unless the physical domain grows in wall-normal extent approximately as fast as the boundary layer. Motivated by boundary-layer theory, we define $z = \eta f(x)$ where $f(x)$ is a smooth function which grows like the boundary layer. For laminar flow, an appropriate choice is $f(x) = \sqrt{x/x_0}$. An option is provided in the DNS code to fix the far-field extent of either z or η . In the latter case the physical grid is nonorthogonal and streamwise and wall-normal derivatives are modified via the chain rule as follows:

$$\begin{aligned} \frac{\partial}{\partial x} &\rightarrow \frac{\partial}{\partial x} - \eta \frac{f'(x)}{f(x)} \frac{\partial}{\partial \eta}, \\ \frac{\partial}{\partial z} &\rightarrow \frac{1}{f(x)} \frac{\partial}{\partial \eta}. \end{aligned} \quad (34)$$

With the exception of the first case in Section 5, the results presented below were obtained with the growing-domain option.

Filtering

From the work of Trefethen (1982), Vichnevetsky (1986), and Poinsot and Lele (1992), it is clear that all finite-difference schemes reflect some energy at outflow boundaries. Typically the reflection coefficient (i.e., the ratio of incident to reflected energy) behaves like $(\alpha \Delta x)^h$, where h is the order of the scheme and α is the disturbance wave number. Moreover, numerical reflections arise even if the physical boundary conditions imposed are perfectly nonreflecting. Regardless of the order of the

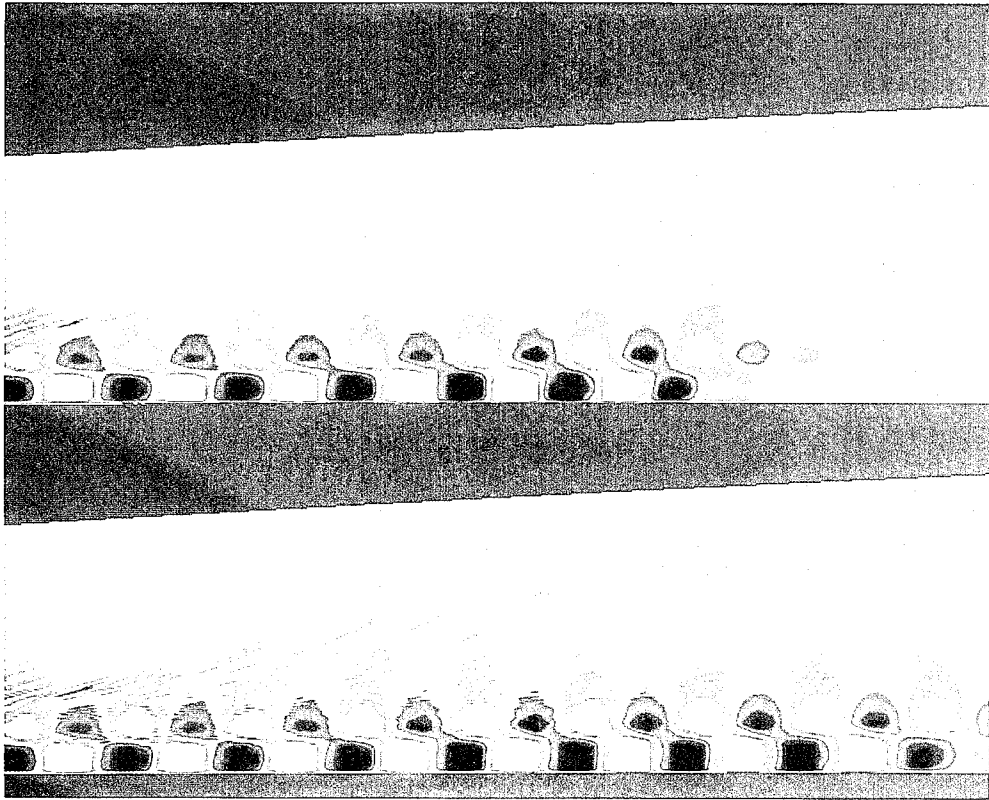


Figure 7. Two-point oscillations and spurious physical waves in disturbance pressure p' in absence of filtering. Two-dimensional Mach 4.5 flat-plate boundary-layer flow with parameter values similar to Case 2 of Section 5. Streamwise extent limited to nine disturbance wavelengths. Wall-normal extent $0 \leq \eta \leq 7.5$. Upper and lower photographs, respectively, show instants in time before and after exit of leading wavefront from computational domain.

scheme, energy at the “sawtooth” wavelength ($\alpha\Delta x = \pi$) is usually totally reflected. As shown by Trefethen (1982) and Vichnevetsky (1986), reflected energy travels upstream as a wave packet at the group velocity V_g , which depends on the spatial discretization scheme. As mentioned by Poinsot and Lele (1992), for the one-dimensional Euler equation, the group velocities of the fourth-order and sixth-order central compact-difference schemes are $3(|u| + c)$ and $14(|u| + c)/3$, respectively. Once the wave packet encounters the Dirichlet inflow condition, which is numerically reflecting to all wavelengths, it reforms and travels downstream as a spurious physical disturbance. For the sixth-order compact-difference scheme, this entire phenomenon masquerades as an apparent coupling between the outflow and inflow boundaries, whereby spurious physical oscillations emanate from the inflow boundary shortly following the exit of the leading wavefront from the outflow boundary, as shown by the flow-visualization sequence in Figure 7. The photograph shows the instantaneous disturbance pressure p' at two different times in a simulation of a two-dimensional Mach 4.5 flat-plate boundary-layer flow. The parameter values are similar to those of Case 2 of Section 5. However, the corrective filtering described below has not been implemented, and, for clarity, the domain is foreshortened to a length of nine disturbance wavelengths in streamwise extent. The upper photograph shows p' prior to the arrival of the leading wavefront at the outflow plane. Two-point oscillations, predominantly in the wall-normal direction, are clearly visible just outside the boundary layer. The lower photograph, with precisely the same color scale, shows p' several periods after the exit of the leading wavefront from the domain. Note the appearance of spurious physical waves along the upper boundary, the ultimate result of a numerical double reflection off the outflow and inflow boundaries.

One of several possible solutions, including upwind biasing, is through filtering, which we prefer for its simplicity and efficiency. Outside the boundary layer, the physical viscosity has a vanishingly small

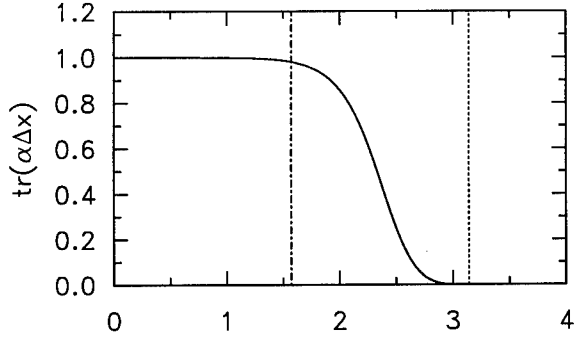


Figure 8. Transfer function $\text{tr}(\alpha\Delta x)$ for sixth-order compact-difference filter.

effect; without some added numerical dissipation, the central-difference approximations result in odd-even decoupling that introduces energy at the troublesome “sawtooth” wavelength. The trick is to keep energy at this wavelength from crossing the outflow boundary. Here, minimal damping is imposed by periodically applying a low-pass sixth-order compact-difference filter (Lele, 1990) to the solution. Typically we apply the filter every few time steps, in which case the additional computational effort is insignificant when amortized over, say, nine Runge–Kutta stages. Moreover, we find it necessary to apply the filter only in the wall-normal direction.

Lele’s sixth-order filter has two free parameters. For the values we have chosen, the formal truncation error for filtering a function $f(x)$ is $\frac{1}{640}(\Delta x)^6 f^{(6)}$, and the transfer function is shown in Figure 8. Two-point oscillations (shown by the vertical dotted line) are completely eliminated by the filter, whereas oscillations of twice that wavelength (shown by the vertical dashed-dotted line) and longer are virtually undamped. In practice, the filter incorporates third-order boundary closure (Lele, 1990), which reduces the global accuracy to fourth order, as does the boundary closure of the 3,4–6–4,3 compact-difference scheme. The filter parameters and frequencies in current use are in no sense optimal, and it may well be possible to reduce the modest computational effort still further by less frequent filtering.

An additional subtlety arises when implementing the filter in the context of a total variable formulation of the governing equations (rather than a disturbance variable formulation). Over many applications, filtering effects gradual evolution of the base state. For example, for a simulation similar to that of Case 4 in Section 5, but with a foreshortened domain (one-sixth the streamwise extent of Case 4) and no imposed disturbance ($\varepsilon = 0.0$), the base density changes approximately 0.01% in 1.4 flow-through times when filtering is applied every third time step. This presents two problems. First, because of the extreme sensitivity of the stability of the flow to changes in the base state, unintended evolution of the base state may affect hydrodynamic stability. Second, when the basic state is subtracted from the total-flow variables for purposes of flow visualization, the disturbance fields, whose velocity components may be, say, of order 10^{-6} , are contaminated. The difficulty is corrected by incorporating an additional steady source term f_1 , to be defined shortly, into the right-hand side of the governing equations. For simplicity, in the context of a first-order (forward Euler) time-integration scheme, the filtering algorithm can be summarized as follows:

For $l = 0, 1, 2, \dots$

$$\begin{aligned} | & \quad \mathbf{q}^{l+1} = \tilde{\mathbf{q}}^l + \Delta t \cdot [\mathbf{v}(\tilde{\mathbf{q}}^l) - \mathbf{f} - \mathbf{f}_1] \\ | & \quad \tilde{\mathbf{q}}^{l+1} = F \mathbf{q}^{l+1} \end{aligned} \tag{35}$$

where \mathbf{q} and \mathbf{v} denote the discrete representations of \mathbf{Q} and \mathbf{V} , respectively, a tilde denotes a filtered quantity, F is the discrete filter operator, and l is the time-level index. In practice, $P\tilde{\mathbf{q}}^l = H\mathbf{q}^l$, where P and H are pentadiagonal and heptadiagonal matrices, respectively, whereby $F = P^{-1}H$. Recognizing

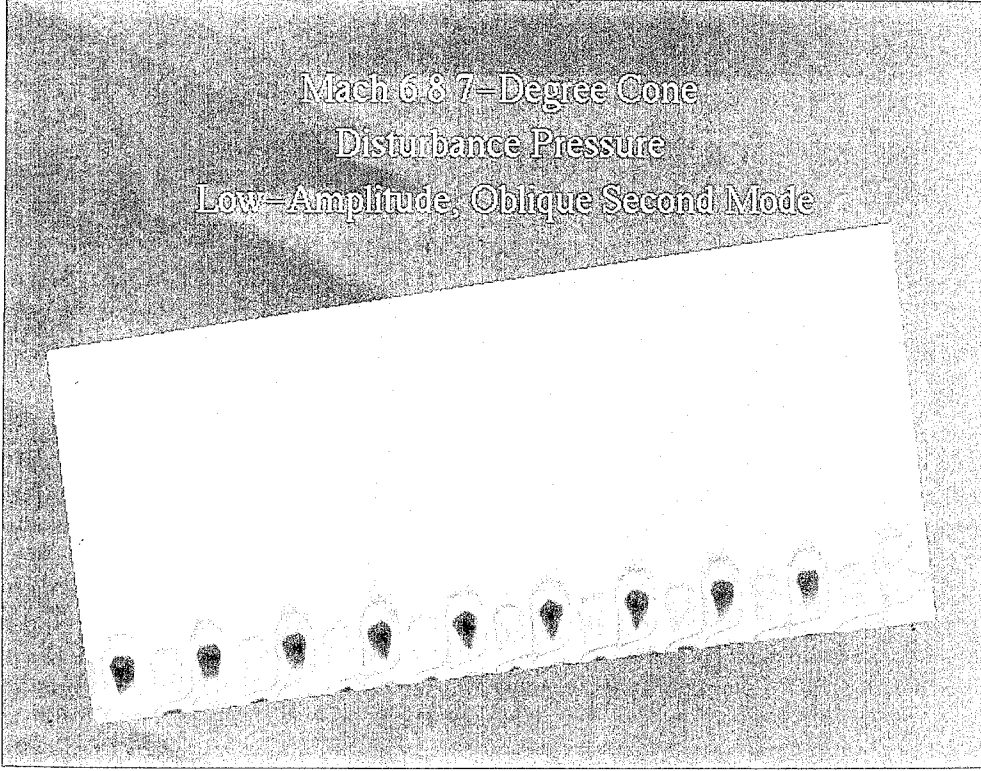


Figure 9. Instantaneous disturbance pressure p' at time of 53 periods of oscillation of fundamental for Case 4 of Section 5. For clarity, computational domain truncated in streamwise extent to $1436 \leq Re_L \leq 1536$. (Buffer domain shown.) Wall-normal extent $0 \leq \eta \leq 7.5$. Results shown in “peak” plane $\theta = 0$. Colors depict contour levels between -3×10^{-6} and 3×10^{-6} .

that (by definition) $\mathbf{v}(\tilde{\mathbf{q}}^0) - \mathbf{f} = \mathbf{0}$ identically, the reader can readily show from (35) that if $l = 0$ and $\mathbf{f}_1 \equiv [(F - I)/\Delta t]\mathbf{q}^0$, then $\mathbf{q}^1 = \mathbf{q}^0$. That is, formally the base state is preserved over the first and all subsequent time steps in the absence of forced disturbances. In practice, the additional source term \mathbf{f}_1 is “turned on” only immediately prior to filtering operations, in which case the filtered basic state remains constant over time nearly to machine precision.

Figure 9 is presented to illustrate the beneficial effects on the solution of the filtering algorithm described above, including the adjustment to prevent unintentional evolution of the base state. It portrays the instantaneous disturbance pressure p' obtained from Case 4 of Section 5. For clarity, however, only the final ten disturbance wavelengths of the computational domain (including the buffer domain) are shown. The time corresponds to 53 periods of oscillation of the disturbance. We note that the maximum amplitude of p' is quite small, in our normalization, more than two orders of magnitude below that of T' , whose amplitude at the inflow boundary is $\epsilon = 0.001$. In contrast to Figure 7, two-point oscillations have been completely damped, thereby eliminating detectable boundary reflections and spurious physical waves, without detriment to the evolution of the instability wave.

4. Algorithm Details

In algorithm design there is frequently a tradeoff between computational effort and storage requirements, as is the case here. For a fully explicit scheme, storage requirements are modest, and the overriding consideration is to minimize the computational work per time step. We discuss very briefly several considerations which contribute to the efficiency and simplicity of the algorithm.

For the three-dimensional compressible Navier–Stokes equations, the minimum number of partial derivative computations required by an explicit algorithm to evaluate \mathbf{V} is 27: 9 for the rate-of-deformation tensor, 3 for the heat flux components, and the remaining 15 for the components of the

flux vectors **E**, **F**, and **G**. Both our conservative (energy equation) and nonconservative (pressure equation) formulations require only the minimum number of 27 partial derivative evaluations. Specifically, partial derivative evaluations are implemented through calls to a subroutine PARTIAL whose arguments specify:

1. The direction of the derivative.
2. Whether or not to include certain terms which arise from nonzero Christoffel symbols as in the distinction between $D_z^0 u$ and $D_z^1 u$ in (3).
3. If spanwise (azimuthal) symmetry is enforced, whether or not the function is even or odd.

Parameters passed to PARTIAL also specify the difference schemes for each coordinate direction. By this construction we have a wide range of possible options without complicating the core subroutine that evaluates the right-hand side vector **V**. The present algorithm uses (we believe) the minimum storage possible given the minimum work constraint previously discussed. The conservative (energy) formulation of the governing equations requires 18 storage arrays of approximate size $N_x \times N_\theta \times N_z$: 6 for the primitive variables **U** and the viscosity, 5 for storing components of the right-hand side vector **V**, 6 for temporary use in the evaluation of **V**, and 1 for partial derivative evaluations. A significant advantage of the nonconservative (pressure) formulation is that only 16 storage arrays are required. Since the energy equation and pressure equation formulations yield essentially identical results, we favor the pressure formulation for computational efficiency. For both formulations, one additional array is required if the growing-domain option is invoked.

Finally, for computational efficiency, innermost loops typically range over all $(N_x + 1) \times (N_\theta + 1)$ grid points in a surface of constant k , ensuring nearly optimal speed-up on vector processors. For directionally dependent calculations such as FFT evaluations and the solution of tridiagonal systems, the inner computational loop ranges over the number of independent transforms or right-hand sides. On single processors of the Cray Y-MP and the Cray C90, the present algorithm performs at greater than 150 megaflops and 415 megaflops, respectively. In recent calculations on the C90, the algorithm has been assessed at 5.6×10^{-6} seconds per gridpoint per (full) time step.

5. Validation

For comparisons with DNS results, we rely on compressible LST (Mack, 1984; Ng and Zang, 1993) and on results obtained by the compressible PSE method of Chang *et al.* (1991). The reader is referred to these authors for details. Briefly, in classical LST, an eigenvalue problem results from certain assumptions about the basic flow and the wave-like nature of the disturbances. Because of the assumptions, the results of LST are strictly valid only for low-amplitude (linear) disturbances in parallel base flows. Our LST results were obtained from the spectrally accurate spatial linear stability code of Ng and Zang (1993).

The PSE approach uses a traveling wave *ansatz* similar to LST, except that the disturbance shape function (Ψ in (25)) is allowed to vary in both the wall-normal and the streamwise directions. Rapid oscillation of the wave is incorporated into the exponential part of the wave *ansatz*, whereby the shape function evolves in x on a scale much longer than a wavelength. The governing equations thereby reduce to a set of PDEs for the shape function only. The PSE method becomes approximate, rather than exact, when these PDEs are parabolized to facilitate a marching solution. Provided the instabilities are of convective nature, as they are for most high-speed boundary-layer flows, the parabolization approximation is quite reasonable. For nonlinear problems, the disturbances are expressed as Fourier series in the frequency domain. The equations for each Fourier mode are independent except through inhomogeneous terms which arise due to nonlinear mode interactions. Therefore, the PSE method can treat both nonparallel and moderately nonlinear effects.

The comparison of DNS results with those obtained by LST and PSE requires the Fourier decomposition of the DNS data in time and in the azimuthal (spanwise) dimension. The resulting modes are identified with ordered pairs (m_ω, m_β) , where the integers m_ω and m_β label the harmonics in Fourier space with respect to the temporal frequency ω and the azimuthal wave number β , respectively. For example, the fundamental mode is labeled $(1, 0)$ if two-dimensional or $(1, 1)$ if oblique.

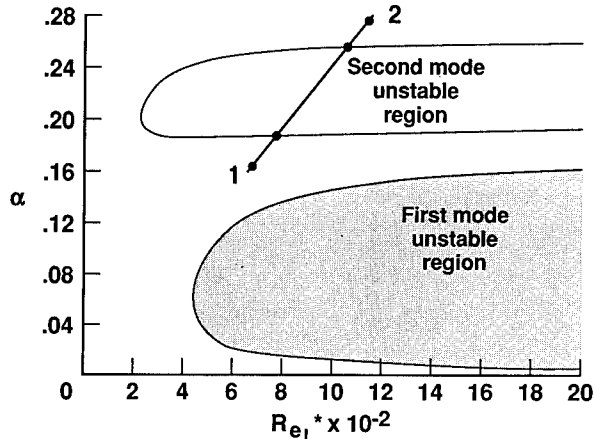


Figure 10. First- and second-mode unstable regions for Mach 4.5 flat-plate boundary layer (after Mack, 1984).

We present four validation cases. The first three consider two-dimensional second-mode disturbances in Mach 4.5 flow along a flat plate. Of these three, the first two examine the evolution of low-amplitude disturbances in parallel and nonparallel boundary-layer flows, respectively. In the third test case, forcing is of large amplitude and harmonics generated by nonlinear interactions attain significant amplitudes. The final test case considers the evolution of a pair of symmetric oblique (helical) second-mode disturbances in a Mach 6.8 boundary-layer flow along a cone.

As a point of reference for the flat-plate cases, we include Figure 10 (adapted from Mack, 1984), which shows distinct regions of instability for first- and second-mode disturbances in a Mach 4.5 planar boundary-layer flow. However, we caution against attempts at exact comparisons for these reasons: Mack's diagram is derived from temporal, rather than spatial, LST; LST inherently assumes locally parallel flow; and Mack uses a slightly different formula for viscosity.

Case 1: Flat Plate, Mach 4.5 Parallel Flow, Two-Dimensional Linear Disturbance. Our primary purpose here is to evaluate the resolution required in the streamwise direction to capture accurately the evolution of a monochromatic disturbance. Figure 11 compares the computed (DNS) and theoretical (LST) maximum amplitude of the temperature fluctuation for a disturbance of dimensionless frequency $F = \omega^* L^*/(u_e^* R_{eL}) = 2.29 \times 10^{-4}$, $R_{eL} = 955.67$, and amplitude $\varepsilon \ll 1$ in flat-plate adiabatic-wall flow with $M_e = 4.5$ and $T_e^* = 61.11$ K. These parameter values define a slightly damped second-mode disturbance that corresponds to a point just beyond the upper branch neutral curve in Figure 10. For the DNS, the computational domain spans eight wavelengths in streamwise extent (based on parallel, linear theory). The amplitude maxima versus x are determined by Fourier time-series analysis over the interval from 13 to 14 periods of oscillation of the disturbance, after the leading wavefront has exited the domain. DNS results are shown for the 5,5–6–5,5 scheme at streamwise resolutions of

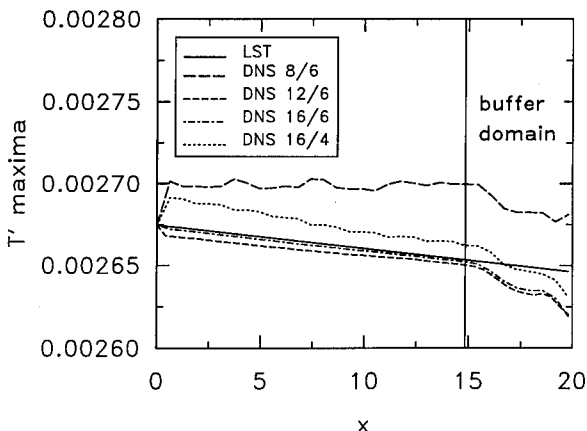


Figure 11. Case 1: DNS and LST results for linear stability problem. In the legend "DNS 16/6," for example, denotes results obtained from spatial DNS by 6th-order differencing and 16 gridpoints per wavelength in the streamwise direction.

8, 12, and 16 grid points per disturbance wavelength and for the 3–4–3 scheme with 16 grid points per wavelength. (In the legend for Figure 11, the first and second integers refer to the number of grid points per wavelength and the order of the scheme, respectively.) In all cases, wall-normal differencing is accomplished by the 3,4–6–4,3 compact-difference scheme with $N_z = 144$. For direct comparison with LST, the base flow is parallel (i.e., $u = u(z)$, $T = T(z)$, and $w = 0$), in which case the forcing terms analogous to Figure 3 are considerably larger than in the developing (nonparallel) flow case. For the fourth-order scheme and for the sixth-order scheme with fewer than 12 points per wavelength, significant oscillations are seen in the maxima. For the sixth-order scheme, the eigenvalue extracted from the DNS is correct to about three and four places for 12- and 16-point resolutions, respectively, except in the immediate vicinity of the inflow boundary where there is a very slight streamwise transient. The resolution needed for accurate results is about twice the six to eight points per wavelength we would have naively anticipated. For nonlinear problems, these results suggest that it is desirable to resolve the shortest wavelengths (highest harmonics) with at least 12 points per wavelength.

Figure 11 also offers reasonable validation of the buffer-domain outflow condition; no appreciable influence is evident on the decay rate of the instability wave upstream of the edge of the buffer domain (shown by the vertical line).

Case 2: Flat Plate, Mach 4.5 Nonparallel Flow, Two-Dimensional Linear Disturbance. Case 2 corresponds approximately to the ray that extends through points 1 and 2 in Figure 10 (Mack, 1984). In this case an evolving (nonparallel) Mach 4.5 flat-plate boundary-layer flow with the same flow parameters as before is forced at a dimensionless frequency $F = 2.2 \times 10^{-4}$. We note that, for Cases 1–3, the ratio δ^*/L^* is constant along the plate with the value 10.46. For the DNS, the inflow and outflow boundaries correspond to $Re_x = 0.49 \times 10^6$ ($Re_L = 700$) and $Re_x = 1.404 \times 10^6$ ($Re_L = 1185.3$), respectively. Over this range of Reynolds numbers, the selected frequency excites a second-mode disturbance. Relative to Figure 10, the computational domain is 36 wavelengths long (based on linear, nonparallel theory at x_{in}) and spans roughly from point 1 (just prior to the lower branch neutral point) to point 2 (somewhat beyond the upper branch neutral point). For the DNS, $N_z = 144$ and $z_{max} = 7.5$. Grid-point clustering and stretching is such that 75% of all points fall in the region bounded by the wall and $z = 1.4$. The buffer region spans the last 5% of the domain in x (i.e., the last 1.8 wavelengths). For comparison with LST, a small amplitude of $\epsilon = 0.001$ is used for the DNS calculation to render insignificant the nonlinear terms of second order or higher in ϵ . The present results were obtained for $N_x = 576$, with points equally spaced in x , and can be considered very well resolved at 16 grid points per wavelength.

The PSE and DNS calculations both proceed from identical disturbance states. However, their respective base states were derived independently, that of the PSE calculation being obtained by finite-difference techniques. The amplitude distributions of the disturbance components imposed at the inflow station can be found in Figure 2 of Pruett and Chang (1993). Because the PSE calculation is linear, amplitude is arbitrary. For the comparison, the amplitudes of the PSE and DNS density fluctuations are equated at the inflow station, and all other disturbance quantities are scaled proportionately. Since the PSE computation is performed in Fourier space, the solution provides the contents of individual modes by default. To extract the temporal Fourier harmonics from the DNS data, we perform a time-series analysis analogous to hot-wire anemometry in physical experiments. The flow field is sampled over time at selected grid points (usually a substantial subset of the computational grid) and is subsequently Fourier analyzed for its harmonic content. Figure 12 presents the amplitude envelope of the density component of the fundamental mode versus η , obtained from 32 samples that span the one-period interval between periods 42 and 43. Because the phase velocity of the second-mode disturbance is about 90% of the edge velocity, by period 42 the leading wavefront has exited the outflow boundary and the flow has settled into a quasi-steady periodic state. Individual profiles in Figure 12(a) correspond to different streamwise locations, equally spaced between the inflow boundary and a point 32 wavelengths downstream (ahead of the beginning of the buffer region). For clarity, these profiles are each staggered by a factor of 2 on the logarithmic plot; hence, their maxima are relative, not absolute. Figure 12(b) graphs the density maxima obtained from Figure 12(a) versus the streamwise coordinate x . In Figure 13 the density maxima and the maxima of other

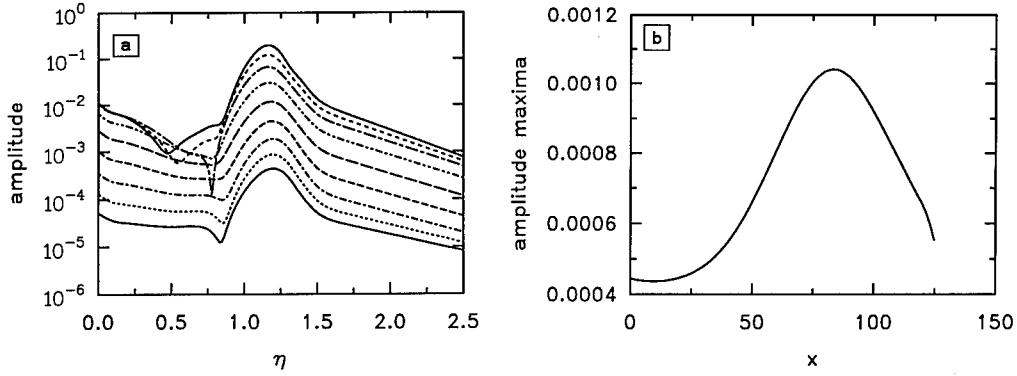


Figure 12. Case 2: Density fluctuation (a) amplitude distribution and (b) amplitude maxima for DNS.

flow quantities obtained in analogous fashion are plotted versus Re_L (rather than versus x) and are compared with the PSE results. For clarity, only every eighth DNS value is plotted. As shown in Figure 13, the agreement between the PSE and DNS results is excellent. The rapid divergence of the DNS and PSE results near the outflow boundary is attributed to the nonphysical damping of the instability wave as it traverses the buffer region and should be disregarded. From Figure 13, it can be observed that, in a nonparallel flow, maxima (or minima) of the various components of the disturbance do not necessarily occur at the same streamwise locations. Hence, neutral points and growth rates are nonuniquely defined. Based on the temperature component of the disturbance, the lower and upper branch neutral points occur at approximately $Re_L = 740$ and $Re_L = 1050$, respectively, in surprisingly good agreement with Figure 10.

Although Figure 13 shows good agreement at maxima, it provides no information about the disturbance structure. In Figure 14 we compare the velocity and density profiles of the PSE and DNS calculations at the station $Re_L = 1046$ near the location of the global maximum of the temperature fluctuation. For comparison of the disturbance structure, we scale the DNS and PSE results so that their respective density maxima are unity. Before rescaling, the respective maxima differ by less than 0.5%. For clarity, only every third DNS value (denoted by symbols) is shown in the figure. Despite the complex nature of the disturbance structure, the agreement is excellent. Moreover, this agreement confirms that the rapid change in the disturbance structure at the three stations that are farthest downstream in Figure 12(a) is a physical change and not the result of a computational anomaly.

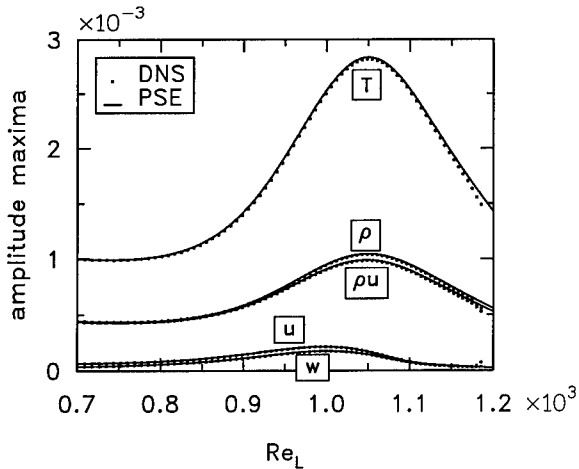


Figure 13. Case 2: PSE and DNS disturbance amplitude maxima versus Re_L .

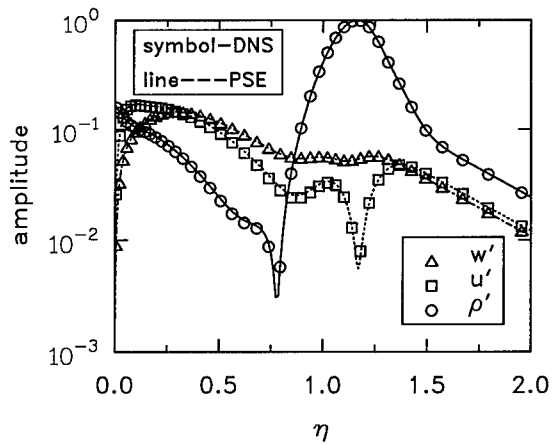


Figure 14. Case 2: Disturbance structure at $Re_L = 1046$.

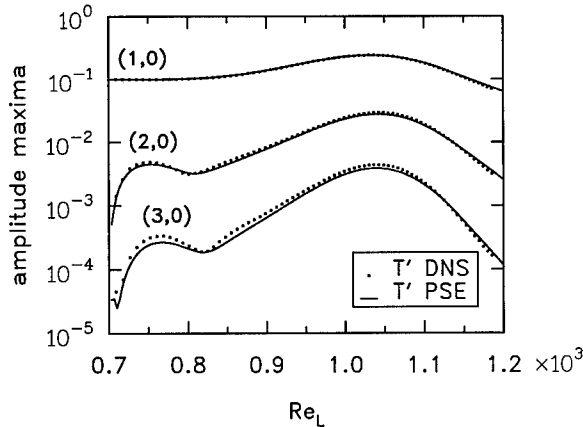


Figure 15. Case 3: Amplitude maxima of fundamental of temperature fluctuation and first two harmonics.

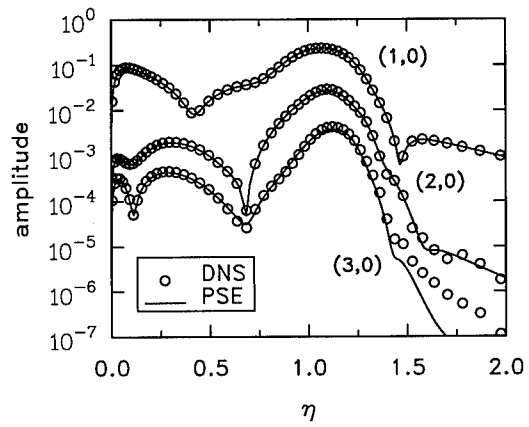


Figure 16. Case 3: Structures of fundamental and first two harmonics of temperature fluctuation at $Re_L = 1050$.

Case 3: Flat Plate, Mach 4.5 Nonparallel Flow, Two-Dimensional Nonlinear Disturbance. With regard to parameter values, this case is identical to the case above, except that the forcing amplitude is quite large at $\epsilon = 0.1$. At this level of forcing, temperature fluctuations will grow in amplitude to a value that is 25% of the edge temperature of the base flow. For the DNS calculation, wall-normal resolution remains as before; however, 32 grid points per primary disturbance wavelength are used for a total of 1153 points in x . Based on the resolution criterion established for the linear case, the fundamental and its first harmonic are well resolved. The second harmonic, however, is somewhat underresolved. Higher harmonics, which contain very little energy, are unresolved.

Figure 15 compares the PSE and DNS results with regard to the streamwise evolution of the maxima of the temperature component of the fundamental and its first two harmonics. For the DNS, the Fourier analysis is performed on 32 time samples that span the interval between periods 48 and 49. The methods agree well qualitatively and quantitatively; however, greater disagreement occurs as the index of the harmonic increases. At the streamwise location of maximum disturbance amplitude, the PSE and DNS results differ by 0.15%, 6%, and 12%, respectively, for the fundamental (1, 0), the first harmonic (2, 0), and the second harmonic (3, 0). (Recall that, because the present calculation is two-dimensional, $m_\beta = 0$.)

A further comparison is shown in Figure 16, in which the PSE and DNS predictions of the structure of the temperature component of the fundamental and its first two harmonics are compared. In contrast to the (linear-amplitude) results presented in Figure 14, the present (nonlinear-amplitude) results have not been rescaled and are presented on a logarithmic scale so that all three modes can be shown with clarity. Between the wall and the critical layer, both methods produce similar amplitude distributions. Outside the boundary layer, there is divergence between the PSE and DNS results in the asymptotic rate of decay of the second harmonic. There are any number of possible physical and/or numerical reasons for this discrepancy. Among these are the differences between PSE and DNS in the imposition of far-field boundary conditions. In the PSE approach Dirichlet conditions are imposed on the disturbance in Fourier space at very large η (typically $\eta \approx 50$). Details of the imposition of boundary conditions for the PSE method can be found in Chang *et al.* (1991). In the DNS, inviscid characteristic conditions (described previously) are imposed in physical space along the far-field boundary $\eta = 7.5$. However, we remind the reader that the logarithmic scale of Figure 16 exaggerates these differences, which are of order 10^{-6} relative to the base state, and it is beyond our current intentions to ferret out the sources of errors of this magnitude or to state categorically which method is “correct.” Within the boundary layer, the region of principal interest, the methods agree remarkably well.

Finally, a major effect of the strong nonlinearity is a mean (0, 0) component that distorts the base flow. Figure 17 shows that the PSE and DNS calculations both predict large (5%) distortions of the

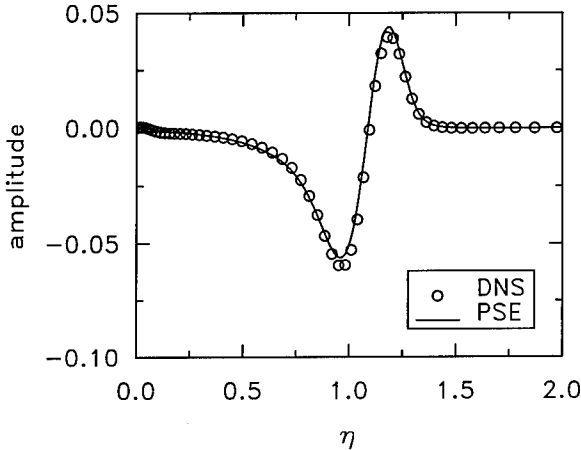


Figure 17. Case 3: Nonlinearly generated mean temperature distortion versus η at $Re_L = 1050$.

base temperature distribution near the critical layer. Disagreement between the methods is roughly 6% at the points of maximum distortion. The reason for the disparity is presently unknown.

Case 4: Sharp Cone, Mach 6.8 Nonparallel Flow, Three-Dimensional Linear Disturbance. In this final validation case we consider the high-speed boundary-layer flow along an axisymmetric sharp cone, which is forced to excite two symmetric oblique (helical) second-mode disturbances. The geometry and the flow parameters given below are chosen to correspond approximately to the stability experiment of Stetson *et al.* (1983) in a hypersonic wind tunnel with a free-stream Mach number of 8:

$$\varphi = 7^\circ \text{ (constant)}, \quad M_e = 6.8, \quad T_e^* = 71 \text{ K}. \quad (36)$$

We assume that the boundary-layer edge conditions remain constant, a reasonable approximation except near the tip of the cone, a region excluded in the present simulations. The PSE calculation spans from $700 \leq Re_L \leq 1800$. To limit the size of the DNS computation, we consider only the region corresponding to $1013 \leq Re_L \leq 1536$. At the DNS inflow boundary, the disturbance parameters are

$$\begin{aligned} F &= 2.094 \times 10^{-4}, \\ n &= 13 \quad (\beta_0 = 1.1736, R_0 = 11.077), \\ \varepsilon &= 0.001, \end{aligned} \quad (37)$$

and $\delta_{in}^*/L^* = 11.17$. Whereas the geometry and flow parameters correspond to the experiment of Stetson *et al.* (1983), the disturbance parameters were selected somewhat arbitrarily. The dimensionless frequency given in (37) corresponds to a physical frequency of 180 kHz, considerably higher than the dominant 102 kHz frequency observed in the experiment. The higher frequency was selected for this validation case because its entire instability region, including the lower and upper branch neutral points, is contained within a fairly short streamwise region, one of (almost) reasonable size for a DNS calculation of modest computational effort. There is nothing sacred about the particular choice of $n = 13$, except that it yields an unstable mode of a sizeable obliqueness angle (24.66° at the DNS inflow boundary) for the given frequency.

Figure 18 presents the evolution of the amplitudes of each of the five components of the fundamental (1, 1) mode for $700 \leq Re_L \leq 1500$. In this case the buffer region for the DNS calculation is not shown. As in Case 2, the PSE calculation is performed in the linear mode, in which case amplitude is arbitrary. For the comparisons below, the maximum densities of the PSE and DNS calculations are equated at the DNS inflow plane, and all other quantities are scaled accordingly. The agreement between the DNS and PSE results is, in general, quite good. The kinks in the u' maxima curve at $Re_L = 1120$ and the w' maxima curve at $Re_L = 1280$ are due to the double-humped structure of the disturbance shown in Figure 19. Remarkably, the DNS and PSE results predict the shift of the global maximum from one hump to the other at precisely the same values of Re_L . There is some discrepancy

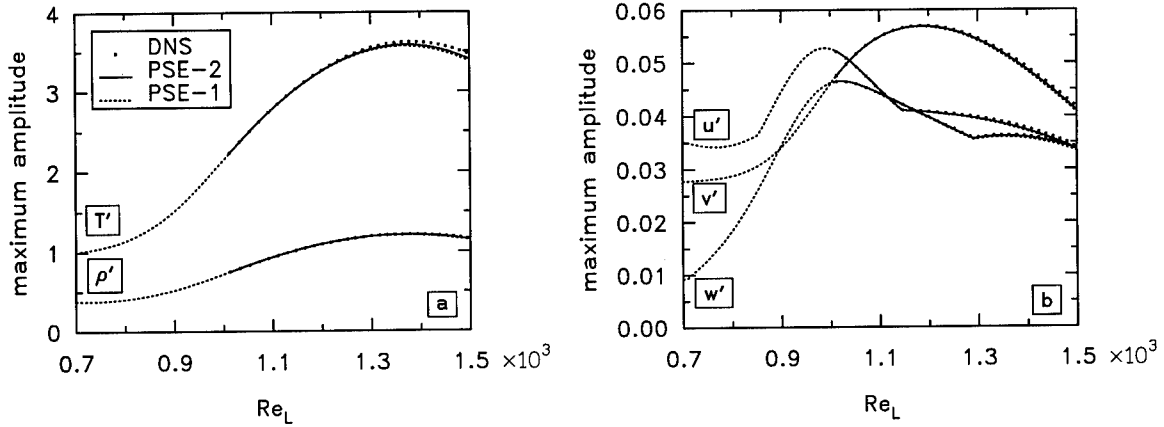


Figure 18. Case 4: PSE and DNS disturbance amplitude maxima versus Re_L for cone case: (a) T' and ρ' and (b) u' , v' , and w' . Two distinct PSE results differ only in the method by which wall-normal derivatives of the base flow are computed.

in the DNS and PSE maxima, which is most significant in the temperature, and which increases with streamwise distance. To eliminate one potential source of disagreement for this comparison, the laminar base flow Q^0 along the cone was obtained for both the PSE and DNS calculations from the spectrally accurate BL code of Pruett and Streett (1991) and Pruett (1993). The remaining sources of disagreement may be either physical or numerical or a combination. We remind the reader that the governing equations, the far-field boundary conditions, and the discretions of the two methods differ, to mention but a few of many subtle differences whose effects may be cumulative. Because the flow is sensitive to seemingly imperceptible changes, it is somewhat pointless to try to isolate the sources of disagreement. Perhaps it is more instructive to demonstrate this flow-field sensitivity. In Figure 18 two sets of PSE results are shown. The two sets differ only in the method by which derivatives of the base state were obtained. In the first set all derivatives were computed internally in the PSE code to fourth-order accuracy. In the second set the derivatives u_z , u_{zz} , T_z , and T_{zz} were computed to spectral accuracy in the BL code and were subsequently passed to the PSE code. Figure 20 compares the first and second derivatives of the temperature as computed by the BL and PSE codes. At worst, the temperature derivatives computed by the two methods differ by less than 0.001, and, in the graphical format, they are indistinguishable. Moreover, velocity derivatives obtained by the two methods agree everywhere to more than four significant digits. Nevertheless, the cumulative effect of these seemingly insignificant differences between derivative profiles is discernible in Figure 18. This inconsistency did not arise for the flat-plate test cases studied previously, for which the base flow is

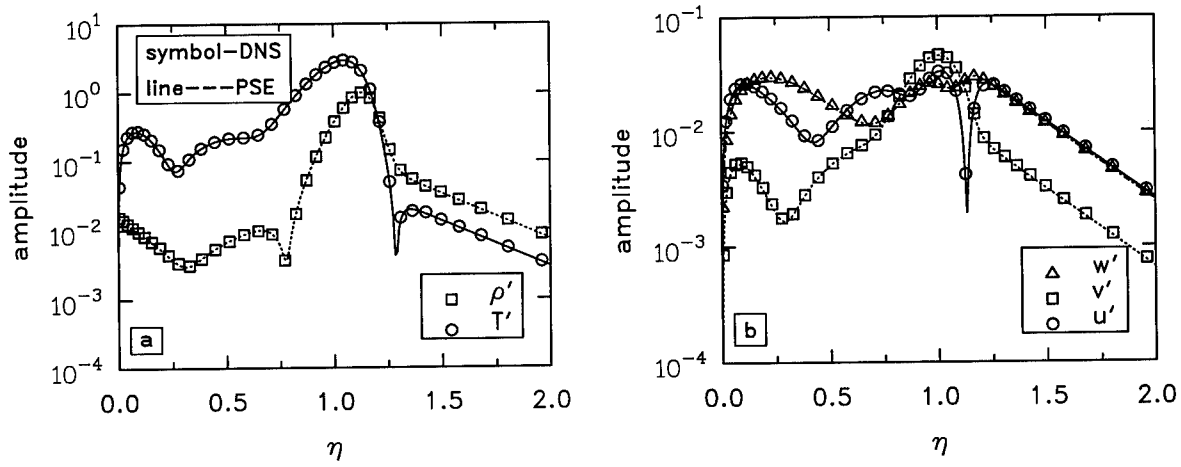


Figure 19. Case 4: Structure at $Re_L = 1291$ of (a) T' and ρ' and (b) u' , v' , and w' .

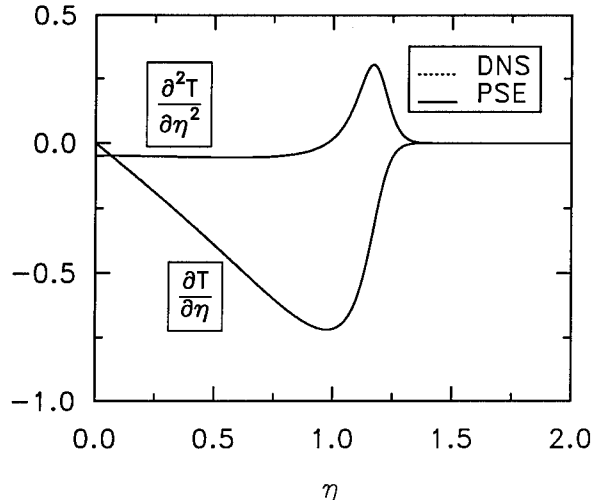


Figure 20. Case 4: Wall-normal derivatives of base temperature.

obtained from a similarity solution whose derivatives can be obtained semianalytically. These results reveal the extreme sensitivity of the stability of high-speed wall-bounded flows to changes in the base state and underscore the necessity of numerical methods of the highest accuracy for such problems.

Before concluding, we offer a few comments on the computational resources required by the present algorithm. DNS is, in general, an expensive research tool. Cases 3 and 4 of this section consumed approximately 40 and 150 hours, respectively, on a single processor of a Cray Y-MP. It is estimated that spatial DNS of the complete laminar-breakdown process for a high-speed boundary-layer flow will require at least 2000 Cray-2 hours and at least 256 megawords of memory. Needless to say, such a tool is not for routine use at the present time. Nevertheless, spatial DNS is invaluable as a means of validating less-expensive approximate methods (e.g., PSE and LES) and for building high-fidelity data bases of transitioning flows, from which transition modelers can construct simplified models. With continued algorithm refinements, supercomputer advancements, and massively parallel implementations, we believe spatial DNS of transition to turbulence will be practical and routine well within a decade.

6. Conclusions

A highly accurate algorithm has been developed for the direct numerical simulation (DNS) of forced, spatially evolving instability waves in high-speed wall-bounded flows. To minimize dissipation and dispersion errors, the fully explicit algorithm exploits both spectral collocation and high-order central compact-difference techniques. In its present form the algorithm allows for three-dimensional flow along two-dimensional or axisymmetric bodies. Of particular interest in this work are the flat-plate and the sharp-cone geometries.

Part 1 of this paper deals primarily with thorough validation of the DNS scheme by comparisons with results obtained from classical linear stability theory (LST) and from the parabolized stability equation (PSE) method. Test cases examine forced two-dimensional second-mode instability waves in Mach 4.5 flat-plate boundary-layer flows and three-dimensional second-mode waves in a Mach 6.8 flow along a sharp cone. From these validation studies, several insights emerge that pertain both to the numerical methods and to the physical problems addressed. First, for the Mach numbers of the test cases, the streamwise resolution needed to obtain good agreement with theoretical results was higher than anticipated. With sixth-order streamwise accuracy, approximately 12 and 16 grid points per wavelength were required in order to extract the growth rate of a monochromatic disturbance to three and four place accuracy, respectively. Second, for nonparallel flows, consistent inflow conditions for the DNS can be obtained from the PSE method, whereas inflow conditions derived from LST are fundamentally inconsistent due to the parallel-flow approximation of LST. Third, at these high Mach numbers, the stability of the boundary layers was found to be sensitive to

the slightest (almost imperceptible) change in the base state. Fourth, for low-amplitude (linear) disturbances the agreement between the PSE method and the DNS results was near perfect in terms of both the amplitude and the structure of the disturbances. Fifth, for large-amplitude (nonlinear) disturbances, agreement between the two methods was near-perfect for the fundamental and good for engineering purposes for the higher harmonics, with the tendency towards greater disagreement the higher the harmonic. Finally, the generally close agreement between DNS and PSE results convincingly demonstrates the potential of the PSE method as a reliable new tool for analysis of hydrodynamic stability in high-speed wall-bounded flows.

At present there is a great need for experimental studies of stability and transition in high-speed boundary-layer flows. Until such experiments are accomplished, the only available source of detailed flow-field information for high-speed transitional flows is DNS. The development and validation of the present DNS algorithm thus fills a void in the national capability in the area of transition research. Using this new tool, Part 2 of this work will examine in detail the laminar breakdown of a perturbed high-speed boundary-layer flow along a cone.

Acknowledgments

The authors wish to acknowledge the many colleagues whose insights, suggestions, or comments contributed to this work. Among these are Dr. Craig Streett, Dr. Shlomo Ta'asan, Dr. Saad Ragab, Dr. Harold Atkins, and Chris Kennedy. The authors are also grateful to Dr. Leslie Mack for his pioneering work in the stability of high-speed flows and for permission to use Figure 10.

References

- N.A. Adams and L. Kleiser. Numerical simulation of transition in a compressible flat-plate boundary layer. In *Transitional and Turbulent Compressible Flows—1993* (L.D. Kral and T.A. Zang, eds.). FED, Vol. 151. ASME, New York, 1993, pp. 101–110 (presented at the Fluids Engineering Conference, Washington, DC, June 20–24, 1993).
- A. Bayliss, L. Maestrello, P. Parikh, and E. Turkel. Wave phenomena in a high Reynolds number compressible boundary layer. In *Stability for Time Dependent and Spatially Varying Flows* (D.L. Dwyer and M.Y. Hussaini, eds.). Springer-Verlag, New York, 1985, pp. 188–205.
- C. Canuto, A. Quarteroni, M.Y. Hussaini, and T.A. Zang. *Spectral Methods in Fluid Dynamics*. Springer-Verlag, Berlin, 1988.
- M.H. Carpenter, D. Gottlieb, and S. Abarbanel. The stability of numerical boundary treatments for compact high-order finite-difference schemes. ICASE Report No. 91-71, 1991.
- C.-L. Chang. Unpublished personal communication, 1993.
- C.-L. Chang, M.R. Malik, G. Erlebacher, and M.Y. Hussaini. Compressible stability of growing boundary layers using parabolized stability equations. AIAA Paper 91-1636, 1991.
- D.F. DeSanto and H.B. Keller. Numerical studies of transition from laminar to turbulent flow over a flat plate. *J. Soc. Indust. Appl. Math.*, Vol. 10, No. 4, 1962, pp. 569–595.
- S.P.G. Dinavahi and C.D. Pruett. Analysis of direct numerical simulation data of a Mach 4.5 transitional boundary-layer flow. In *Transitional and Turbulent Compressible Flows—1993* (L.D. Kral and T.A. Zang, eds.). FED, Vol. 151. ASME, New York, 1993, pp. 147–153 (presented at the Fluids Engineering Conference, Washington, DC, June 20–24, 1993).
- W. Eissler and H. Bestek. Spatial numerical simulations of nonlinear transition phenomena in supersonic boundary layers. In *Transitional and Turbulent Compressible Flows—1993* (L.D. Kral and T.A. Zang, eds.). FED, Vol. 151. ASME, New York, 1993, pp. 69–76 (presented at the Fluids Engineering Conference, Washington, DC, June 20–24, 1993).
- N.M. El-Hady, T.A. Zang, and U. Piomelli. Dynamic subgrid-scale modeling for high-speed transitional boundary layers. In *Engineering Applications of Large Eddy Simulations—1993* (S.A. Ragab and U. Piomelli, eds.). FED, Vol. 162. ASME, New York, 1993 (presented at the Fluids Engineering Conference, Washington, DC, June 20–24, 1993).
- G. Erlebacher and M.Y. Hussaini. Numerical experiments in supersonic boundary-layer stability. *Phys. Fluids A*, Vol. 2, No. 1, 1990, pp. 94–104.
- H. Fasel, A. Thumm, and H. Bestek. Direct numerical simulation of transition in supersonic boundary layers: oblique breakdown. In *Transitional and Turbulent Compressible Flows—1993* (L.D. Kral and T.A. Zang, eds.). FED, Vol. 151. ASME, New York, 1993, pp. 77–92 (presented at the Fluids Engineering Conference, Washington, DC, June 20–24, 1993).
- N. Gilbert and L. Kleiser. Near-wall phenomena in transition to turbulence. In *Near-Wall Turbulence: 1988 Zoran Zaric Memorial Conference* (S.J. Kline and N.H. Afgan, eds.). Hemisphere, Washington, DC, 1990, pp. 17–27.
- B. Gustafsson. The convergence rate for difference approximations to mixed initial boundary-value problems. *Math. Comp.*, Vol. 29, No. 130, 1975, pp. 396–406.
- L. Kleiser and T.A. Zang. Numerical simulation of transition in wall-bounded shear flows. *Annu. Rev. Fluid Mech.*, Vol. 23, 1991, pp. 495–537.

L.D. Kral. Numerical Investigation of Transition Control of a Flat Plate Boundary Layer. Ph.D. thesis, University of Arizona, 1988.

S.K. Lele. Compact finite difference schemes with spectral-like resolution. Center for Turbulence Research Manuscript 107, Stanford University, April 1990.

L.M. Mack. Boundary-layer linear stability theory. In *Special Course on Stability and Transition of Laminar Flow* (R. Michel, ed.), AGARD Report No. 709, 1984, pp. 3.1–3.81.

L. Maestrello, A. Bayliss, and R. Krishnan. On the interaction between first and second-mode waves in a supersonic boundary layer. *Phys. Fluids A*, Vol. 3, No. 12, 1991, pp. 3014–3020.

L.L. Ng and G. Erlebacher. Secondary instabilities in compressible boundary layers. *Phys. Fluids A*, Vol. 4, No. 4, 1992, pp. 710–726.

L.L. Ng and T.A. Zang. Secondary instability mechanisms in compressible, axisymmetric boundary layers. *AIAA J.*, Vol. 31, No. 9, Sept. 1993, pp. 1605–1610.

J. Nordstrom. The influence of open boundary conditions on the convergence to steady state for the Navier–Stokes equations. *J. Comput. Phys.*, Vol. 85, 1989, pp. 210–244.

X. Normand and M. Lesieur. Direct and large-eddy simulations of transition in the compressible boundary layer. *Theoret. Comput. Fluid Dynamics*, Vol. 3, 1992, pp. 231–252.

T.J. Poinsot and S.K. Lele. Boundary conditions for direct simulations of compressible viscous flows. *J. Comput. Phys.*, Vol. 101, 1992, pp. 104–129.

C.D. Pruett. On the accurate prediction of the wall-normal velocity in compressible boundary-layer flow. *Internat. J. Numer. Methods Fluids*, Vol. 16, 1993, pp. 133–152.

C.D. Pruett and C.-L. Chang. A comparison of PSE and DNS for high-speed boundary-layer flows. In *Transitional and Turbulent Compressible Flows—1993* (L.D. Kral and T.A. Zang, eds.). FED, Vol. 151. ASME, New York, 1993, pp. 57–67 (presented at the Fluids Engineering Conference, Washington, DC, June 20–24, 1993).

C.D. Pruett and C.L. Streett. A spectral collocation method for compressible, non-similar boundary layers. *Internat. J. Numer. Methods Fluids*, Vol. 13, No. 6, 1991, pp. 713–737.

C.D. Pruett and T.A. Zang. Direct numerical simulation of laminar breakdown in high-speed, axisymmetric boundary layers. *Theoret. Comput. Fluid Dynamics*, Vol. 3, No. 6, 1992, pp. 345–367.

M. Rai and P. Moin. Direct numerical simulation of transition and turbulence in a spatially evolving boundary layer. AIAA Paper No. 91-1607, 1991.

K.F. Stetson and R.L. Kimmel. On the breakdown of a hypersonic laminar boundary layer. AIAA Paper 93-0896, 1993.

K.F. Stetson, E.R. Thompson, J.C. Donaldson, and L.G. Siler. Laminar boundary-layer stability experiments on a cone at Mach 8. Part 1: Sharp cone. AIAA Paper 83-1761, 1983.

C.L. Streett and M.G. Macaraeg. Spectral multi-domain for large-scale fluid dynamic simulations. *Appl. Numer. Math.*, Vol. 6, 1989/90, pp. 123–139.

K.W. Thompson. Time dependent boundary conditions for hyperbolic systems. *J. Comput. Phys.*, Vol. 68, 1987, pp. 1–24.

A. Thumm. Numerische Untersuchungen zum laminar-turbulenten Stroemungsumschlag in transsonischen Grenzschichtstroemungen. Ph.D. thesis, Universitaet Stuttgart, 1991.

A. Thumm, W. Wolz, and H. Fasel. Numerical simulation of spatially growing three-dimensional disturbance waves in compressible boundary layers. In *Laminar-Turbulent Transition. IUTAM Symposium, Toulouse, France, 1989* (D. Arnal and R. Michel, eds.). Springer-Verlag, Berlin, 1990, pp. 303–308.

L.N. Trefethen. Group velocity in finite difference schemes. *SIAM Rev.*, Vol. 24, No. 2, 1982, pp. 113–136.

R. Vichnevetsky. Invariance theorems concerning reflection at numerical boundaries. *J. Comput. Phys.*, Vol. 63, 1986, pp. 268–282.

F.M. White. *Viscous Fluid Flow*. McGraw-Hill, New York, 1974, pp. 347–350.

J.H. Williamson. Low-storage Runge–Kutta schemes. *J. Comput. Phys.*, Vol. 35, 1980, pp. 48–56.

T.A. Zang, C.-L. Chang, and L.L. Ng. The transition prediction toolkit: LST, SIT, PSE, DNS, and LES. Fifth Symposium on Numerical and Physical Aspects of Aerodynamic Flows, January 1992.

Attachment 2

SIMULATION OF CROSSFLOW INSTABILITY ON A SUPERSONIC HIGHLY SWEPT WING

Dr. C. David Pruett
Department of Applied Science
The College of William and Mary

Abstract

A suite of highly accurate numerical algorithms has been developed and validated for use in the simulation of crossflow instabilities on supersonic swept wings, an application of potential relevance to the design of the High-Speed Civil Transport (HSCT). Principal among these algorithms, and the primary focus of this report, is a direct numerical simulation (DNS) scheme embodied in the code CMPSBL, which solves the unsteady, three-dimensional compressible Navier-Stokes equations in orthogonal, body-fitted coordinates. The DNS algorithm is fully explicit in time and exploits a combination of spectral and high-order compact-difference techniques for spatial discretizations. A companion code WINGBL2, documented in a previous technical report, exploits spectral-collocation techniques to solve the compressible boundary-layer equations to provide an accurate basic state to the DNS. In addition, the algorithm INTBL uses spectral techniques to interpolate the boundary-layer solution onto the computational grid of the DNS. These algorithms are then used to examine the development of stationary crossflow instability on an infinitely long 77-degree swept wing in Mach 3.5 flow. Crossflow disturbances are generated by simulating spanwise-periodic roughness elements downstream of the computational inflow boundary. The results of the DNS are compared with the predictions of linear parabolized stability equation (PSE) methodology obtained with the code ECLIPSE (developed independently of this effort). In general, the DNS and PSE results agree closely, thereby providing a reasonable validation of both approaches. Specifically, both methods show the alignment of stationary crossflow vortices along inviscid streamlines as anticipated. Moreover, the methods agree well in the predicted spatial evolution of a small-amplitude (linear) crossflow mode and in the structure of this mode. Although further validation is warranted (for large-amplitude stationary and traveling crossflow disturbances), the present results demonstrate a new numerical capability relevant to a problem of practical importance.

1 Introduction

Understanding, predicting, and controlling laminar-turbulent transition remains the holy grail of aeronautics research despite more than a century of assault from the combined forces of theory, experiment, and computation. Recent advances on each of these fronts and in the areas of materials processing and micro-actuators (Ho and Tai [13]), however, have brought this elusive goal within sight, and there is renewed interest in laminar-flow control (LFC) technology.

Because surface friction and heat transfer increase dramatically as the boundary layer transitions from a laminar to a turbulent state, the design of efficient aerospace vehicles depends upon accurately predicting the transition location and the extents of the regions of laminar, transitional, and turbulent flows. Although, in the current economic environment, it is questionable whether laminar flow control (LFC) technology can be made commercially viable in the near future for subsonic aircraft, the potential economic benefit could be significant for supersonic transport aircraft such as the proposed High-Speed Civil Transport (HSCT). This is because maintenance of laminar flow over a substantial portion of the wing of the HSCT, for example, would not only reduce drag but would also reduce thermal loads on the structure.

The practical attainment of LFC technology will require fundamental understanding of the stability of three-dimensional boundary-layer flows. Examples of prototypical three-dimensional boundary-layer flows are flows past rotating cones and spheres, flow on a rotating disk, flows in corners, and flows over swept wings, the latter of which is of the most practical relevance.

Whereas the stability of two-dimensional flows has been studied extensively, researchers are only beginning to focus attention on three-dimensional boundary-layer flows. Theoretical and experimental results demonstrate that there exists a far greater variety of paths to transition for three-dimensional boundary layers than for two-dimensional flows. For example, in the case of the swept wing, the flow may be susceptible to Tollmien-Schlichting (TS) instability, Goertler instability (associated with the concavity of the lower surface; e.g., see Hall [12]), crossflow instability (the subject of the discussion to follow), and attachment-line instability (instability of the flow along the leading edge; e.g., see Joslin [17]). For the wing of the HSCT, to be specific, crossflow instability is likely to be the most “dangerous” in the sense of leading most rapidly to transition.

Crossflow instability was first identified in the 1940’s in experiments related to the Northrop flying wing. As stated by Reed and Saric [28] in their review paper, “Although unyawed wind-tunnel tests showed laminar flow back to 60 percent chord, yawed flight tests showed turbulent flow from the leading edge on both the upper and lower surfaces.” In flow over a swept wing, the inviscid streamlines form S-curves because the pressure gradients associated with body curvature accelerate or decelerate the flow in the direction perpendicular to the leading edge while leaving the velocity component parallel to the leading edge

virtually unchanged. The combination of curvilinear inviscid streamlines and the viscous no-slip condition at the wall generates a crossflow velocity perpendicular to the local inviscid streamline. The crossflow velocity is zero both at the wall and in the freestream (by definition), and thus, in between it experiences a maximum and a point of inflection. Maxima for crossflow velocities are typically on the order of 3-4 percent of the velocity in the direction of the streamlines.

Even though crossflow velocities are typically relatively small, the presence of the inflection point renders the flow susceptible to crossflow instability, which is of inviscid type. The instability manifests itself as co-rotating vortices that align themselves roughly along inviscid streamlines. The spacing between adjacent vortices is on the order of several δ^* , the boundary-layer displacement thickness. According to Mack [20], the instability exists for a whole band of frequencies, including zero. Curiously, linear stability theory predicts the most amplified disturbances to be traveling waves, whereas stationary crossflow instability is frequently observed in experiments, except close to laminar breakdown (Reed and Saric [28]). Choudhari and Streett [10] and Choudhari [9] have shown, on the basis of receptivity theory, that surface irregularities may favor the development of stationary crossflow modes by giving them much larger initial amplitudes than those of traveling crossflow waves.

Both theory and experiment concur that crossflow instability dominates on swept wings in regions of rapidly changing pressure. Other regions on the wing, however, may be dominated by TS-like instabilities (which we take to include the first-mode instability of compressible boundary-layer flow). According to Reed and Saric [28], a major unanswered question is “the interaction between crossflow vortices and TS waves.” It appears that crossflow vortices can modify the TS instability to enhance its growth rate. From experiments, it also appears that the crossflow instability is extremely sensitive to initial conditions, and it has even been suggested that the theory for crossflow instability is not well posed (Reed and Saric [28]).

In summary, transition on a swept wing is a highly sensitive and complex process. The transition location is affected by nonparallelism of the mean flow, pressure gradient, surface roughness, freestream turbulence, and body curvature. Moreover, these elements give rise to both inviscid crossflow modes and to TS-like instabilities, which may interact. It is unreasonable to ask any approximate theory to accommodate all of these diverse and interacting elements. As a result, the problem is well suited for numerical investigations using direct numerical simulation (DNS), for which a minimum of simplifying assumptions are made.

Crossflow instability on swept wings in incompressible flows has been investigated recently with a parabolized stability equation (PSE) approach by Malik et al. [21] and with DNS by Lin and Reed [19], Fuciarelli and Reed [11], Joslin and Streett [18], and Joslin [16]. The present work is believed to be the first investigation of crossflow instability on a supersonic swept wing by means of DNS. Direct simulation is computationally expensive; consequently, we believe that simulations are most fruitful when focused along with theoretical and experimental investigations on a single problem of practical importance. To that end, we have selected a test problem that parallels the quiet wind-tunnel experiment on a supersonic swept wing by Cattafesta et al. [3]. Moreover, our DNS results are compared

with results obtained by PSE methodology for compressible flows (e.g., Chang et al. [6]) in an attempt to cross-validate both methods for this difficult problem. For computational efficiency, we must limit consideration to quasi-three-dimensional (infinite-span) swept-wing flows. This assumption permits highly efficient spectral collocation methods to be exploited in the spanwise direction. The limitation of the computational model should be kept in mind in drawing conclusions relative to the experiment. We emphasize, however, that the full effects of streamwise surface curvature are incorporated into the DNS model, in contrast to most recent approaches.

The next section discusses the coordinate system and governing equations. Section 3 summarizes the numerical methodology. The computational test case is addressed in Section 4. Results are presented in Section 5, and Section 6 concludes with a few closing remarks.

2 Governing Equations

The flow is governed by the compressible Navier-Stokes equations in the form given in Eqs. (1)-(15) of Pruett et al. [26], which is appropriate for body-fitted coordinates on either axisymmetric or two-dimensional bodies. Here, we consider only two-dimensional (infinite in span) wing-like bodies. Let the wing be imbedded in a rectangular cartesian coordinate system (ξ, η, ζ) , with the wing cross section specified as $\zeta(\xi)$. Let (x, y, z) denote body-fitted coordinates such that x is the surface arc length normal to the attachment line, y is the spanwise coordinate (parallel to the attachment line), and z is the wall-normal coordinate. (The reader will note that, for consistency with the coordinates of Pruett et al. [26], the y and z coordinates are switched relative to the normal convention.) Accordingly, u , v , and w are the velocity components in the streamwise, spanwise, and wall-normal directions, respectively. The fundamental metric tensor has only one non-constant quantity s , which arises from streamwise curvature and is defined in Eq. (2) of Pruett et al. [26]. Moreover, by ρ , p , T , μ , and κ , we denote the density, pressure, temperature, viscosity, and thermal conductivity of the fluid, respectively. The viscosity μ is modeled by Sutherland's law, and $\kappa = \mu/Pr$, where Pr is the Prandtl number. For computational efficiency, the energy equation is cast in terms of the pressure, as given in Eq. (15) of Pruett et al. [26]. All flow variables, except pressure, are non-dimensionalized by post-shock reference values, denoted by subscript r . Pressure is scaled by $\rho_r^* u_r^{*2}$. Lengths are scaled by the boundary-layer displacement thickness δ^* at the (computational) inflow boundary. Throughout this work, dimensional quantities are denoted by asterisk.

3 Methodology

The conventional approach to (spatial) stability analysis, adopted here, consists of three basic steps: determination of a laminar base state whose stability is to be investigated,

perturbation of the base state by superposition of disturbances at or near the computational inflow boundary, and calculation of the spatial evolution of the disturbances. Each of these steps is addressed in turn below.

3.1 Base Flow

The base state is computed by the spectrally accurate boundary-layer code WINGBL2 of Pruett [25], which was specifically designed for the infinite-span swept-wing problem. The effects of streamwise curvature, streamwise pressure gradient, and wall suction/blowing are taken into account in the governing equations and boundary conditions. The boundary-layer equations are formulated both for the attachment-line flow and for the evolving boundary layer. The equations for the evolving flow are solved by an implicit marching procedure in the direction perpendicular to the leading edge, for which high-order (up to 5th) backward differencing techniques are used. In the wall-normal direction, a spectral collocation method based on Chebyshev polynomial approximations is exploited. Spectral accuracy is advantageous in that 1) the solution is highly accurate even for relatively coarse grids, 2) the boundary-layer profiles and their derivatives are extremely smooth (a necessity for stability analyses), and 3) interpolation to other grids can be accomplished with virtually no loss of accuracy.

A few comments in regard to point 3) above are in order. Because WINGBL2 is designed specifically for applications to stability analyses, DNS, and large-eddy simulation (LES), special attention has been paid to the process of interpolating data to other grids, for example, to a DNS grid. For this purpose, a companion code INTBL was written. In brief the procedure is as follows. In the output from WINGBL2, lengths are scaled by δ^* , which grows with x^* . The outer edge of the boundary layer typically lies between 2 and 4 displacement thicknesses from the wall. Let $z_e(x)$ denote the location of the boundary-layer edge. To interpolate to a grid uniform in z , for example, we first perform spectrally accurate interpolation in the interior region $0 \leq z \leq z_e$ coupled with analytic extrapolation outside the boundary layer ($z > z_e$). This step is followed by high-order (typically 5th) polynomial interpolation in x .

The analytic extrapolation in the far field is accomplished at each x by solving the ordinary differential equation that results from the continuity equation in the asymptotic limit $z \rightarrow \infty$. In many boundary-layer approximations, some curvature effects are neglected, in which case the continuity equation may be inexact. Indeed, it was determined that Eq. (7-100) on page 397 of Anderson et al. [1], on which the continuity equation for WINGBL2 was originally based, is inexact for compressible flow; an exact continuity equation was subsequently derived. That the continuity equation be exact is essential if the near-field solution and the far-field extrapolation are to merge continuously, as they must for DNS. The method proposed by Pruett [24] to extract wall-normal velocity accurately, adopted here also, permits an independent check of continuity. Typically WINGBL2 conserves continuity nearly to machine precision, as shown in Figs. 1 and 2.

The input to WINGBL2 consists primarily of three files that contain the wing geometry, the wing pressure distribution in the form of tabulated pressure coefficients, and the reference conditions. Cubic splines are used to interpolate as necessary between the tabulated values. The reference conditions are presumed to be downstream of leading-edge shocks.

3.2 Disturbances

The base flow is perturbed in the manner of Joslin [16], who simulated crossflow instability in incompressible flow on a swept wing. Disturbances are introduced by mass-preserving suction and blowing at the wall. Currently, we exploit steady suction/blowing in order to induce stationary crossflow modes. The suction/blowing strip spans the width of the wing, but is localized in x . (Henceforth, for brevity, we will refer only to the “suction” strip.) As noted by Joslin [16]: “This mode of disturbance generation would correspond to an isolated roughness element within the computational domain.” Joslin has found by numerical experimentation that the suction strip should not be located farther upstream than approximately 10 percent chord. Otherwise, the crossflow modes are not swept downstream. The spanwise wavenumber β of the disturbance strip is a fundamental parameter of the flow, as is the maximum amplitude of the wall velocity w_{wall} . Typically, very small normalized wall velocities (say, $w_{\text{wall}} = 10^{-4}$ or less) suffice to trigger stationary crossflow instability. The suction/blowing profile is a full sine wave in the spanwise direction; to ensure continuity of derivatives, the cube of a half sine function is used to shape the wall velocity in the streamwise direction.

3.3 DNS Methodology

For the present application, we exploit the highly accurate DNS methodology of Pruett et al. [26] with minor modifications. To summarize briefly, time is advanced fully explicitly by the third-order low-storage Runge-Kutta scheme of Williamson [30]. Spatial derivatives are approximated by a combination of spectral-collocation techniques and high-order compact-difference schemes. In the streamwise and wall-normal directions, we exploit fourth- and sixth-order compact-difference operators, respectively. In the spanwise direction, the flow is assumed to be periodic, making possible the use of a spectral collocation technique with Fourier exponential basis functions. The assumption of spanwise periodicity restricts the basic flows under consideration to quasi-three-dimensional; that is, all base-flow quantities, including the three velocity components, are assumed to be functions only of the streamwise and wall-normal coordinates. This is equivalent to assuming that the wing is of infinite span with constant cross-section.

The boundary conditions require some modification from those given in Pruett et al. [26]. For a well-designed wing, the streamwise component of velocity should be everywhere subsonic. Therefore, the streamwise velocity at the computational inflow boundary is subsonic,

and in the outer (Euler) region of the domain, there exists an upstream characteristic velocity. Accordingly, we specify the Riemann invariants along the inflow boundary. This inflow treatment, correct for inviscid flow, is not entirely satisfactory in the viscous layer, where all flow quantities should be specified (Poinsot and Lele [22]). The wall and far-field boundary treatments are the same as described in Pruett et al. [26], except that suction and blowing are introduced at the wall to induce the disturbance, as described previously. We currently exploit a buffer domain (Streett and Macaraeg [29]) in the vicinity of the outflow boundary, as was done successfully by Pruett et al. [26]. However, for this particular application, we are presently experiencing some reflection from the outflow boundary. It is not yet known whether the reflection is of numerical or physical origin (or both). Additional effort should be directed to diagnosis and refinement of the inflow and outflow boundary conditions.

The work of Pruett et al. [26] and the present work differ conceptually in that, for the latter, which is concerned with stationary crossflow instability, only the time-asymptotic solution is of interest. Time integration is accomplished solely as a means of relaxation toward the steady state. Physically, from the point at which a disturbance is introduced, a wave packet propagates (predominantly) downstream, depositing in its wake the stationary crossflow instability of interest. Once the leading wave packet has exited the domain, the flow settles to its perturbed steady state. Attainment of a steady state is assessed by computing the residuals of the time-independent compressible Navier-Stokes equations. In practice, in the context of fully explicit time advancement, the residual is simply the discrete update vector. Evolution of the global maximum residual for the calculation of the “Results” section is shown in Fig. 3. The largest residuals are associated with the continuity (ρ) and spanwise momentum (v) equations. The maximum residuals grow approximately exponentially in time as the leading wavefront propagates downstream at a nearly constant velocity, as implied by Fig. 4. Different formulations for the buffer domain may change the velocity of propagation in this region. For example, the buffer domain treatment that resulted in the least reflection also unfortunately significantly diminished the propagation velocity in the buffer region, necessitating a relatively long integration time. Following the exit of the leading wavefront from the domain (not shown), the residuals decay rapidly, provided the outflow boundary treatment is non-reflecting. Moreover, examination of the local residual field (also not shown) indicates that the flow is essentially stationary a short distance upstream of the trailing edge of the propagating wave packet. Finally, Fig. 5 shows the location of the maximum residual in terms of the wall-normal gridpoint index k . The initial outward movement of the residual is associated with a weak acoustic pulse that radiates from the receptivity region near the suction strip. Following the exit of this wave from the upper boundary, the maximum residual remains near $k = 40$, a distance of approximately $1.5\delta^*$ from the wall, until the wave encounters the buffer domain. The wall-normal location of maximum residual coincides closely with the maximum perturbation amplitude of the crossflow instability.

3.4 PSE Methodology

The PSE method, developed originally for incompressible flow, has been extended to compressible boundary layers by Bertolotti and Herbert [2] and by Chang and coworkers (See references [4] and [7]). The method is rapidly gaining favor as a powerful and efficient tool for analyzing the stability of spatially evolving boundary layers. The method treats both nonparallel boundary-layer effects and moderately nonlinear wave interactions. The method has recently been adapted for application to supersonic swept wings by Chang and coworkers. The theory is presented in Reference [6]; a user-friendly code ECLIPSE for industry applications has also been developed and is documented in Reference [5]. The reader is referred to these references for a thorough discussion of the theory and practice of PSE methodology.

4 Test Problem

As implied in the introduction, the computational experiment is an approximate analog to the quiet wind-tunnel experiment of Cattafesta et al. [3]. In this section, we compare and contrast the physical and numerical experiments.

4.1 The physical experiment

The reader is referred to Cattafesta et al. [3], which is summarized briefly here. A 15-inch-long model of a wing section with a leading-edge sweep angle $\psi = 77.1^\circ$ is being tested in NASA Langley's Mach 3.5 quiet wind-tunnel to investigate crossflow instability and transition. A three-dimensional view of the model is shown in Fig. 2 of Cattafesta et al. [3]. The model was designed originally to experience flow similar to that on the 70-degree swept wing of an F-16XL, which is undergoing flight experiments by NASA. The model cross section is geometrically similar to that of the first 6.25 percent chord of the wing glove on the modified F-16XL. However, the sweep angle on the wind-tunnel model was increased to 77 degrees to match the leading-edge-normal Mach number of the Mach 3.5 wind-tunnel experiment to that of the Mach 2.4 flight experiment, for which the normal Mach number is 0.78.

Because crossflow-dominated transition is quite sensitive to controlled and random influences, it was deemed necessary to conduct the experiment in a quiet facility. In the physical experiment, the freestream unit Reynolds numbers were varied from 1.5 to 8.0 million per foot by varying the tunnel stagnation pressure, and the angle of attack was incremented from -2 to 5 degrees. In support of the experiment, Euler and Navier-Stokes calculations were conducted, as were N -factor studies using the stability code COSAL (Iyer et al. [15]). As in most theoretical studies of crossflow instability, traveling waves were predicted to have the highest growth rates; peak N -factors were observed for frequencies in the range of 40

to 60kHz. The transition front on the model was estimated on the basis of recovery factors obtained from surface thermocouples. More recently, temperature-sensitive paint has been used to more finely resolve the transition front. The measured and predicted transition fronts correlated approximately for $N = 14$. However, regions on the model with microscopic surface scratches showed the telltale streaks of stationary crossflow vortices.

4.2 The numerical experiment

Data for the numerical experiment were inferred from an Euler calculation of the flow on the wing model by Iyer [14], for which the freestream conditions were

$$M_\infty = 3.5 \quad (1)$$

$$T_\infty = 173.9^\circ \text{ R} \quad (2)$$

$$Re_1 = 2.6 \times 10^6 \text{ per ft.} \quad (3)$$

$$\alpha = 0.145^\circ \quad (4)$$

Fig. 6 shows isobars on the upper and lower surfaces of the model for the freestream conditions given above. Near the aft stations on the wing, the wing sections are similar (Cattafesta et al. [3]), and the isobars are nearly parallel, which suggests that the flow can be approximated as quasi-three-dimensional (although Cattafesta et al. caution against this). Accordingly, we consider a wing section perpendicular to the leading edge at a station 1.091 ft. along the leading edge, as shown in Fig. 7. The chord length c_n^* normal to the leading edge at the section of interest is 0.2496 ft. The surface pressure coefficients interpolated from the Euler grid to the wing section are shown in Fig. 8. The surface pressure coefficients were then used as input data for the boundary-layer code WINGBL2 (described earlier) to derive the base state. Some additional interpretation of the Euler data, however, was necessary to provide post-shock reference conditions to the boundary-layer code. From the Euler data, the post-shock Mach number at the point of maximum wingspan was taken to be 3.29. Because of the outward turning of the flow through the shock, the effective wing sweep angle ψ_{eff} increased by a few degrees over the physical value. Finally, the post-shock reference temperature was adjusted to force agreement between the Euler and boundary-layer stagnation temperatures. These self-consistent post-shock reference values are summarized as follows:

$$M_r = 3.29 \quad (5)$$

$$T_r = 189.6^\circ \text{ R} \quad (6)$$

$$u_r = 2220.4 \text{ f/s} \quad (7)$$

$$p_r = 64.06 \text{ psia} \quad (8)$$

$$\psi_{\text{eff}} = 80.81^\circ \quad (9)$$

From the geometry, reference values, and pressure coefficients, the boundary-layer solution was computed based on the approximation of isentropic post-shock flow. The boundary-layer and Euler solutions for the edge Mach number and edge temperature are compared in Figs. 9 and 10, respectively. The small disagreement between the two solutions can be attributed to two sources. First, although the shock is weak, shock strength varies in azimuth due to the asymmetry of the body. Consequently, the post-shock flow is not strictly isentropic. Second, of course, the base flow is not perfectly two-dimensional. Nevertheless, the close agreement between the two solutions suggests that the simplifying assumptions are reasonable.

Growth of the boundary-layer displacement thickness, obtained from WINGBL2, is presented in Fig. 11. The favorable pressure gradient induces a boundary layer that grows linearly, except during the most rapid acceleration near the leading edge. The boundary-layer solution is compared at two stations, $x_c \equiv \xi^*/c_n^* = 0.0$ and $x_c = 0.173$, in Figs. 12 and 13, which show velocity and temperature profiles, respectively. By definition, of course, the streamwise velocity vanishes along the attachment line, which corresponds (nominally) to $x_c = 0.0$. Figure 14 shows the solution also at $x_c = 0.173$, but in a coordinate system oriented along the inviscid streamline. In the rotated coordinate system, u_t^* and u_c^* denote the tangential and crossflow velocities, respectively. Note the inflectional nature of the crossflow velocity (the component perpendicular to the inviscid streamline). The crossflow Reynolds number, defined in Reed and Saric [28], is shown as a function of x_c in Fig. 15. The maximum crossflow Reynolds number is attained at approximately 20 percent chord and decreases gradually thereafter.

Finally, the boundary-layer solution is interpolated onto the DNS grid by the interpolation code INTBL described previously. The computational domain for the DNS spans approximately from 1 to 70 percent chord in streamwise extent and from the wall to $z = z^*/\delta^* = 25$ in wall-normal extent. At the inflow boundary, $\delta^* = 0.00053$ ft. An algebraic mapping is used in the wall-normal direction to cluster points close to the wall. A second (linear) mapping is used to remove the major effects of the boundary-layer growth shown in Fig. 11, so that the boundary layer remains of nearly constant thickness in the scaled coordinate $z^*/\delta^*(x^*)$. N -factor studies by Chang [8], who used PSE methodology, determined that a stationary crossflow mode of spanwise wavelength $\lambda_y^* = 10$ mm (0.0328 ft.) was strongly amplified. Accordingly, the fundamental spanwise wavenumber was chosen to be $\beta \equiv \beta^*\delta^* = 2\pi\delta^*/\lambda_y^* = 0.1018$. The width of the computational domain was one spanwise wavelength; that is, $1 \times \lambda_y^* = 0.0328$ ft. The suction strip spanned from 6.7 to 9.6 percent chord, and $w_{\text{wall}} = 10^{-4}$.

5 Results

The DNS calculation was made with a resolution of $577 \times 4 \times 97$ in the streamwise, spanwise, and wall-normal directions, respectively. The streamwise and wall-normal resolutions were based on the DNS experience of Joslin [16] and of Pruett and Chang [27]. The spanwise resolution was sufficient to resolve only the mean and a single crossflow mode; hence, dealiasing was exploited (in Fourier space) in the spanwise direction to remove energy in the first harmonic of the spanwise fundamental.

To establish the crossflow disturbances throughout the domain required an integration in time to approximately $t = 1800$, at which time the leading wavefront had encountered the outflow boundary. Because the present outflow conditions are not completely satisfactory, a fraction of the incident energy was reflected by the boundary and contaminated the upstream solution. Hence, the computation was halted prior to the exit of the leading wavefront from the domain. Fig. 16 shows the evolution of the maximum of the (dealiased) perturbation spanwise velocity as a function of the streamwise coordinate. Superimposed on the plot is the amplitude of the v component of the crossflow instability as predicted by linear PSE methodology. The initial amplitude of the PSE result is arbitrarily scaled for the purpose of comparison. In the vicinity of the suction strip, where receptivity is enhanced, spatial transients are observed. Downstream of the suction strip, apparently a stationary crossflow mode is established, which grows in close agreement with the prediction of linear PSE. The leading wave packet is broad and spans approximately $0.35 \leq x_c \leq 0.7$ at termination of the calculation. Moreover, by comparison with the linear PSE result, it appears that the leading wave packet experiences amplitudes one to two orders of magnitude larger than the crossflow instability that is deposited by its passing. Thus, despite the initially low amplitude of the disturbance, strong nonlinearities are encountered as the leading wavefront passes. Indeed, in a previous simulation with a different buffer-domain treatment, in which the wavefront completely exited the computational domain, nonlinearities and their associated Lighthill stresses were strong enough in the wave-packet region to generate significant acoustic energy, as shown in Fig. 17. Following passage of the wavefront, the acoustic radiation vanished.

Figure 16 suggests that a linear crossflow mode has been established in the DNS calculation in the region $0.10 \leq x_c \leq 0.35$. Further confirmation of this is evidenced in Fig. 18, which compares the amplitude of the fundamental spanwise Fourier harmonic of the DNS calculation with the amplitude of the crossflow mode predicted by the PSE method at the station $x_c = 0.22$. For the comparison, the PSE and DNS results are each normalized so that the maximum spanwise perturbation velocity is unity. The predictions of the two methods agree very well for all perturbation components. Consequently for the DNS calculation, the principal effect of the receptivity of the flow to the simulated roughness element is the generation of a linear crossflow mode immediately downstream of the suction strip, an expected result.

Fig. 19 depicts the alignment of the crossflow vortices immediately downstream of the suction strip in the DNS calculation. The disturbances are made visible as contours of con-

stant disturbance density in a plane approximately 1.5 displacement thicknesses from the wall. By slicing Fig. 19 in a specific spanwise plane, the vortex alignment angle can be estimated on the basis of the ratio of the wavelengths in the spanwise and the streamwise directions. Whereas the dimensional spanwise wavelength is fixed, the streamwise wavelength λ_x^* varies, as shown in Fig. 20. Relative to the x axis, the vortex alignment angle is $\tan^{-1}(\alpha_r^*/\beta^*)$, where the streamwise wavenumber $\alpha_r^* = 2\pi/\lambda_x^*$. Shown in Fig. 21 are the vortex alignment angles as computed by linear stability theory (which assumes the flow to be locally parallel) and by the (nonparallel) PSE method. For comparison, the angle of the local inviscid streamline relative to the z axis is also shown. The inviscid streamline angle is derived from the boundary-layer solution as $\tan^{-1}(v_e^*/u_e^*)$. The vortex angle at $x_c = 0.2$ as derived from the DNS results is also shown and agrees closely with the PSE result. Both the DNS and PSE approaches clearly show the tendency of crossflow vortices to align nearly along inviscid streamlines. The maximum deviation in the streamline and vortex alignment angles is approximately three degrees at $x_c = 0.13$.

6 Conclusions

- Direct numerical simulation of crossflow instability in compressible flows on swept wings is computationally intensive. The simulation discussed in the previous section required 100 hours of CPU time on a Cray Y-MP, despite relatively coarse streamwise and spanwise resolution. Several factors contribute to this expense. First, long-time integration is required to establish the instability. Whereas the use of implicit or semi-implicit methods of time advancement could reduce the computational expense by allowing longer time steps, such savings are not guaranteed. Joslin [16] implies that the time step needed to suppress temporal transients and numerical error is considerably less than that permitted by the stability of his semi-implicit approach. Second, because even small disturbances quickly generate a large-amplitude leading wave packet, fine grid resolution is needed to resolve nonlinearities, even if the goal is to investigate linear disturbances.
- At the present stage of development, additional effort is needed to refine both the inflow and outflow boundary conditions. It is not presently known whether the reflections experienced at the outflow boundary are physical or numerical in origin; however, given our previous experience with boundary difficulties (Pruett et al. [26]), we believe the problem can be rectified given sufficient attention.
- Despite the limitations of the numerical experiment, the qualitative and quantitative agreement between the DNS and PSE results is good. The DNS confirms that the crossflow modes predicted to be unstable by PSE are indeed unstable. Moreover, the rate of growth, the vortex orientation angles, and the modal structures predicted by the two methods are shown to agree closely. Although more validation is warranted, particularly of strongly nonlinear interactions, we believe that, given the agreement

between the PSE and DNS methods, PSE methodology can be used reliably and inexpensively to investigate stationary crossflow instabilities on swept-wing configurations relevant to the design of the HSCT.

- An unexpected observation was the radiation of acoustic energy from the (highly non-linear) developing wavefront as the crossflow instability was being established. Although this phenomenon is likely an artifact of the method used to generate disturbances, it underscores the capability of the DNS algorithm and suggests that the method could readily be adapted to applications in the area of aeroacoustics.

Acknowledgements

The author wishes to acknowledge the financial support of NASA and AFOSR, under contract NAS1-19656 and grant F49620-95-1-0146, respectively. The author is especially grateful to Dr. Chau-Lyan Chang for providing PSE results, to Dr. Venkit Iyer for computing the Euler solution, and to Drs. Craig Streett and Ron Joslin for wisdom and counsel in regard to the special problems encountered in simulating crossflow instability.

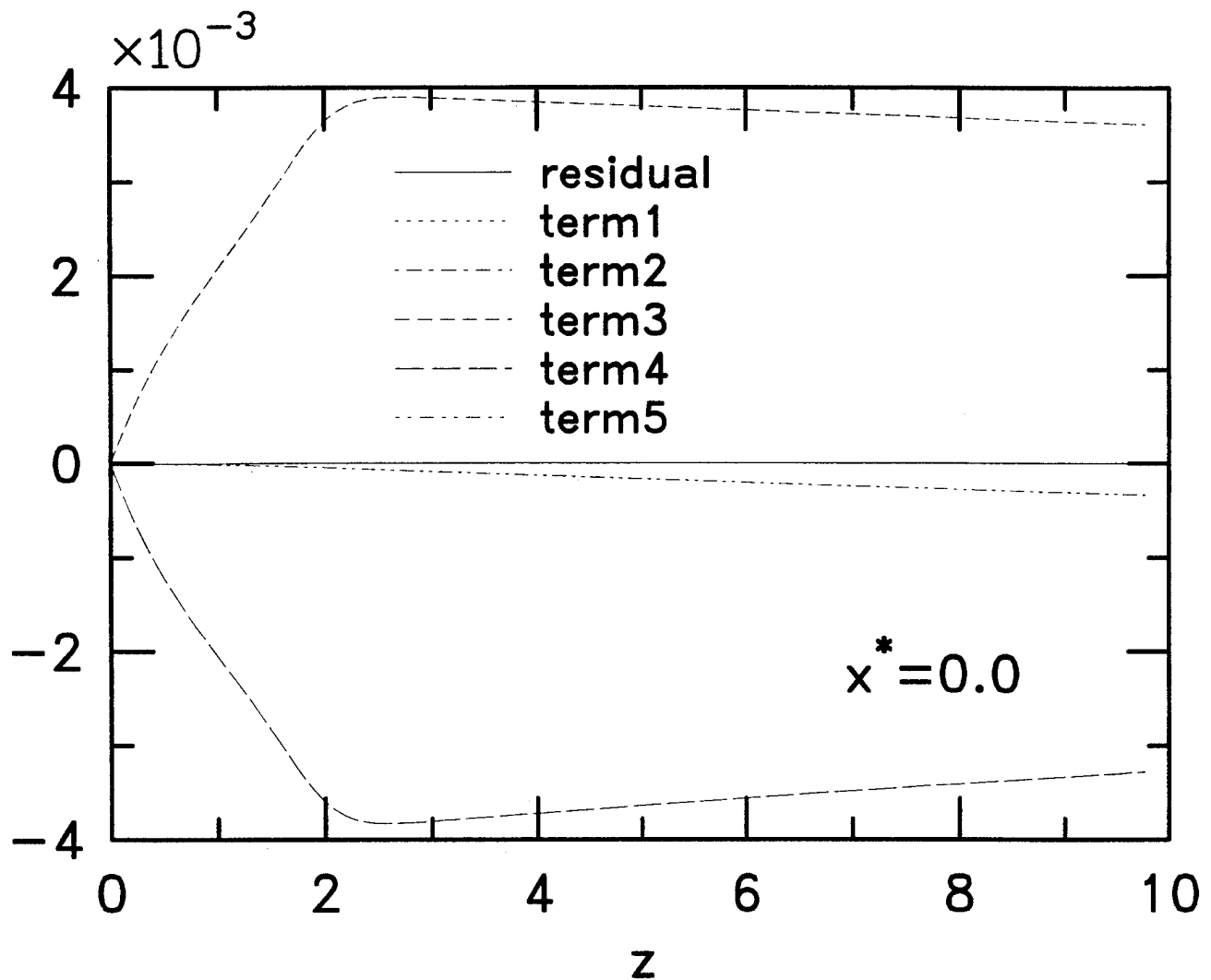
References

- [1] D. A. Anderson, J. C. Tannehill, and R. H. Pletcher, *Computational Fluid Mechanics and Heat Transfer*, Taylor and Francis, New York, 1984, pp. 220, 396-398.
- [2] F. Bertolotti and Th. Herbert, "Analysis of the Linear Stability of Compressible Boundary Layers Using the PSE," *Theoret. Comput. Fluid Dynamics*, Vol. 3, No. 2, 1991, pp. 117-124.
- [3] L. N. Cattafesta III, V. Iyer, J. A. Masad, R. A. King, and J. R. Dagenhart, "Three-Dimensional Boundary-Layer Transition on a Swept Wing at Mach 3.5," AIAA Paper No. 94-2375, 1994.
- [4] C.-L. Chang, M. R. Malik, M. Y. Hussaini, and G. Erlebacher, "Compressible Stability of Growing Boundary Layers Using Parabolized Stability Equations," AIAA Paper No. 91-1636, 1991.
- [5] C.-L. Chang, "ECLIPSE: An Efficient Compressible Linear PSE Code for Swept-Wing Boundary Layers," High Technology Report No. HTC-9503, 1995.
- [6] C.-L. Chang, M. R. Malik, and H. Vinh, "Linear and Nonlinear Stability of Compressible Swept-Wing Boundary Layers," AIAA Paper 95-2278, 1995.
- [7] C.-L. Chang and M. R. Malik, "Non-parallel Stability of Compressible Boundary Layers," AIAA Paper No. 93-2912, 1993.
- [8] C.-L. Chang, personal communication, 1995.
- [9] M. M. Choudhari, "Roughness-Induced Generation of Crossflow Vortices in Three-Dimensional Boundary Layers," *Theoret. Comput. Fluid Dynamics*, Vol. 6, No. 1, 1994, pp. 1-30.
- [10] M. M. Choudhari and C. L. Streett, AIAA Paper No. 90-5258, 1990.
- [11] D. A. Fuciarelli and H. L. Reed, "Stationary Crossflow Vortices," *Phys. Fluids A*, Vol. 4, No. 9, 1992, p. 1880.
- [12] P. Hall, "The Goertler Vortex Instability Mechanism in Three-Dimensional Boundary Layers," *Proc. R. Soc. London Ser. A*, Vol. 399, 1985, pp. 135-152.
- [13] C.-M. Ho and Y.-C. Tai, "Manipulating Boundary-Layer Flow with Micromach-Based Sensors and Actuators," presented at the 12th U.S. National Congress of Applied Mechanics, Seattle, Washington, June 27-July 1, 1994.
- [14] V. S. Iyer, personal communication, 1994.
- [15] V. S. Iyer, R. Spall, and J. Dagenhart, "Computational Study of Transition Front on a Swept Wing Leading-Edge Model," *J. of Aircraft*, Vol. 31, No. 1, 1994.

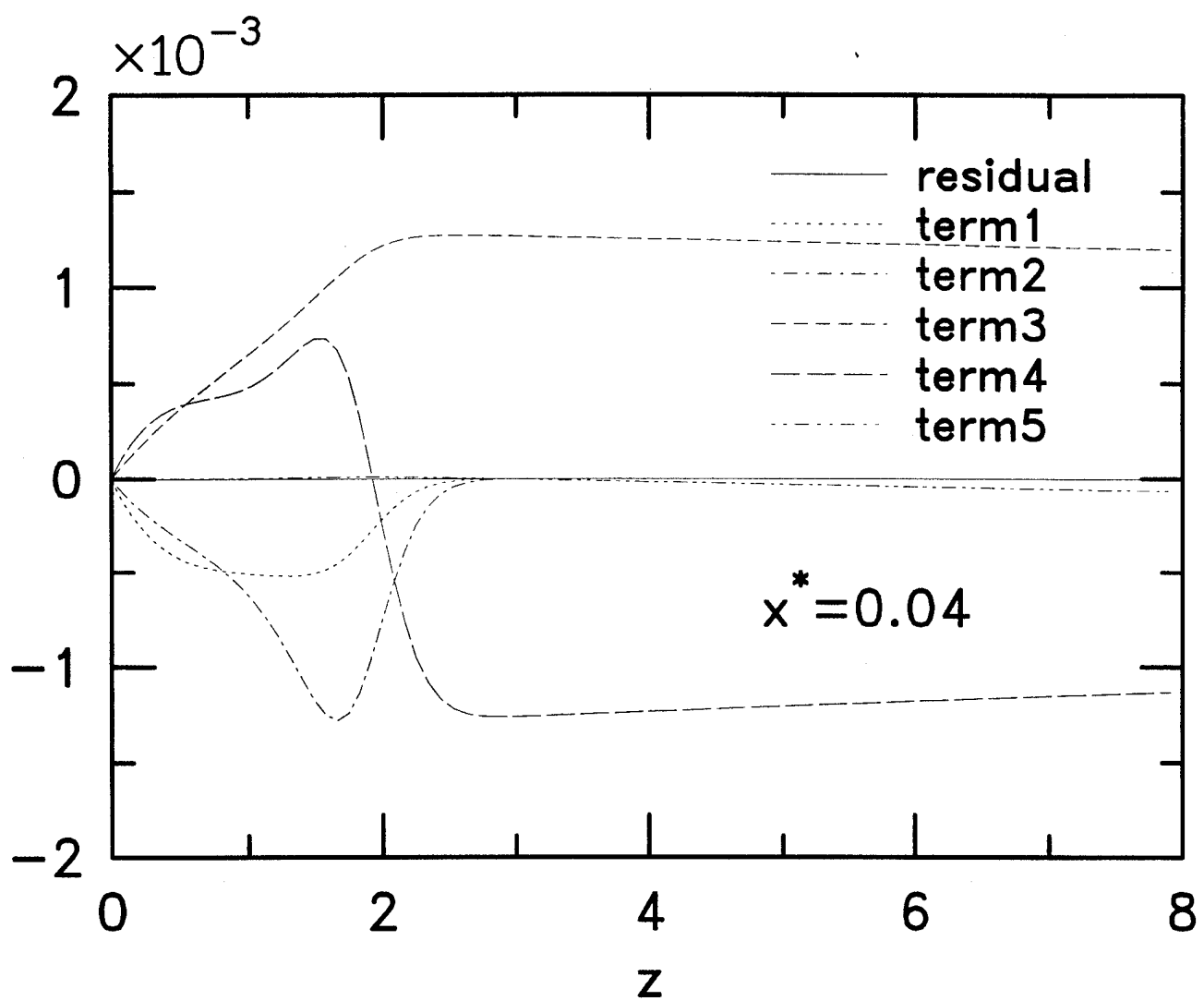
- [16] R. D. Joslin, "Evolution of Stationary Crossflow Vortices in Boundary Layers on Swept Wings," *AIAA J.*, Vol. 33, No. 7, 1995, pp 1279-1285.
- [17] R. D. Joslin, "Direct Simulation of Evolution and Control of Three-Dimensional Instabilities in Attachment-Line Boundary Layers," *J. Fluid Mech.*, Vol. 291, 1995, pp. 369-392.
- [18] R. D. Joslin and C. L. Streett, "The Role of Stationary Crossflow Vortices in Boundary-Layer Transition on Swept Wings," *Phys. Fluids A*, Vol. 6, No. 10, 1994, pp. 3442-3453.
- [19] R.-S. Lin and H. L. Reed, "Navier-Stokes Simulation of Stationary Crossflow Vortices on a Swept Wing," *Bulletin of the American Physical Society*, Vol. 36, No. 10, 1991, p. 2631.
- [20] L. M. Mack, "Boundary-Layer Stability Theory," in *Special Course on Stability and Transition of Laminar Flow*, ed. R. Michel, AGARD Report No. 709, 1984, pp. 3.1-3.81.
- [21] M. R. Malik, F. Li, and C.-L. Chang, "Crossflow Disturbances in Three-Dimensional Boundary Layers," *J. Fluid Mech.*, Vol. 268, 1994, pp. 1-36.
- [22] T. J. Poinsot and S. K. Lele, "Boundary Conditions for Direct Simulations of Compressible Viscous Flows," *J. Comput. Phys.*, Vol. 101, 1992, pp. 104-129.
- [23] C. D. Pruett and Craig L. Streett, "A Spectral Collocation Method for Compressible, Non-similar Boundary Layers," *Int. J. Numer. Meth. Fluids*, Vol. 13, No. 6, 1991, pp. 713-737.
- [24] C. D. Pruett, "On the Accurate Prediction of the Wall-Normal Velocity in Compressible Boundary-Layer Flow," *Int. J. Numer. Meth. Fluids*, Vol. 16, 1993, pp. 133-152.
- [25] C. D. Pruett, "A Spectrally Accurate Boundary-Layer Code for Infinite Swept Wings," NASA Contractor Report 195014, 1994.
- [26] C. D. Pruett, T. A. Zang, C.-L. Chang, and M. H. Carpenter, "Spatial Direct Numerical Simulation of High-Speed Boundary-Layer Flows—Part I: Algorithmic Considerations and Validation," *Theoret. Comput. Fluid Dynamics*, Vol. 7, No. 1, 1995, pp. 49-76.
- [27] C. D. Pruett and C.-L. Chang, "Spatial Direct Numerical Simulation of High-Speed Boundary-Layer Flows—Part II: Transition on a Cone in Mach 8 Flow," *Theoret. Comput. Fluid Dynamics*, to appear.
- [28] Helen L. Reed and William S. Saric, "Stability of Three-Dimensional Boundary Layers," *Annu. Rev. Fluid. Mech.*, Vol. 21, 1989, pp. 235-284.
- [29] C. L. Streett and M. G. Macaraeg, "Spectral Multi-Domain for Large-Scale Fluid Dynamic Simulations," *Appl. Numer. Math.*, Vol. 6, 1989/90, pp. 123-139.

[30] J. H. Williamson, "Low-Storage Runge-Kutta Schemes," *J. Comput. Phys.*, Vol. 35, 1980, pp. 48-56.

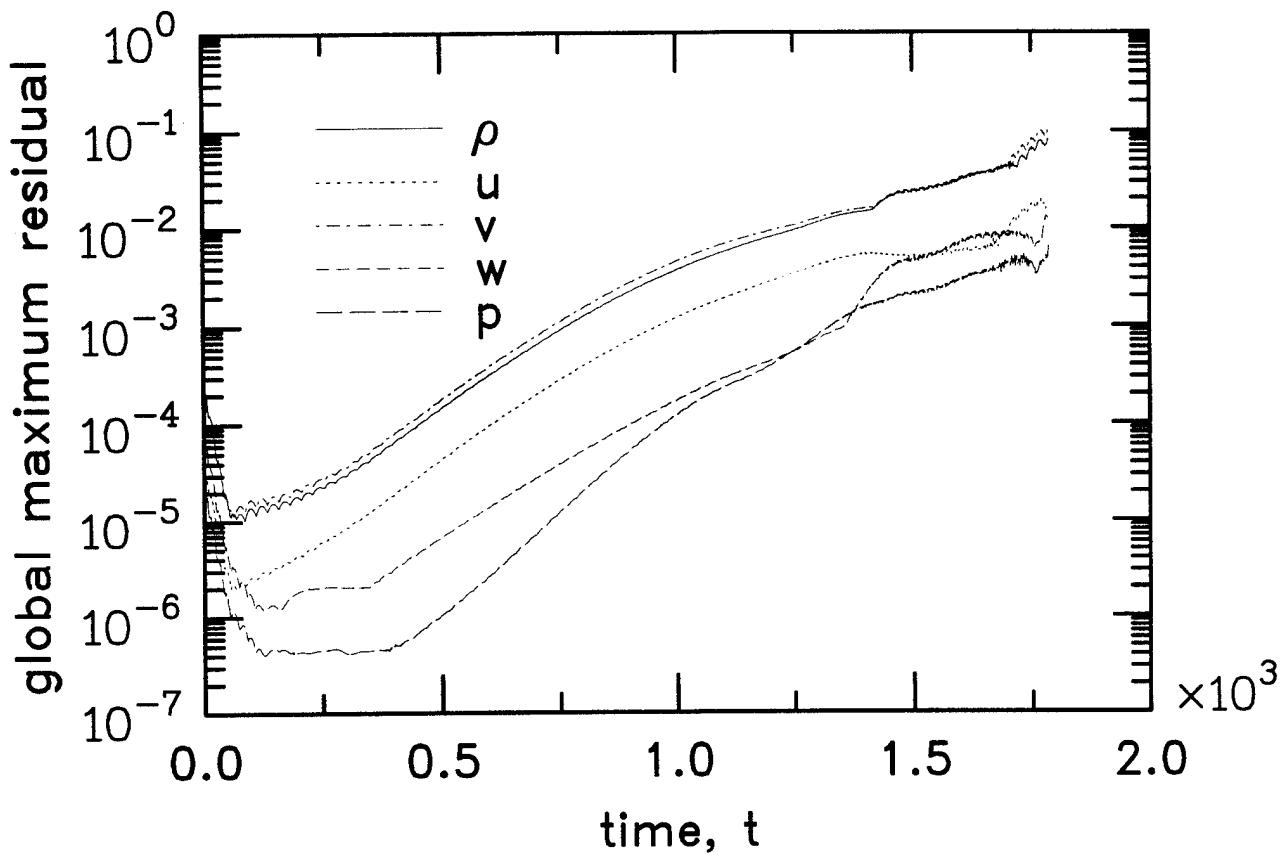
Figures



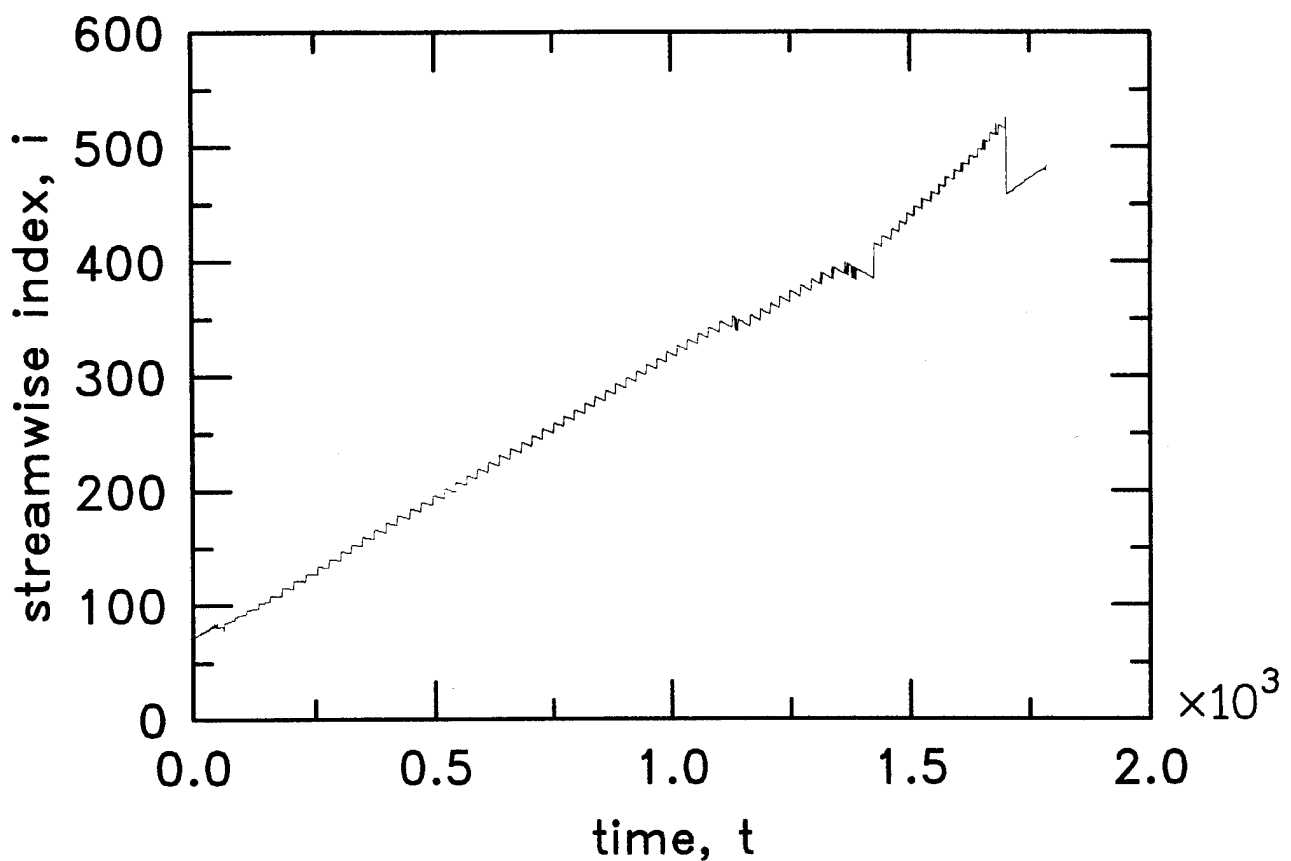
1. Individual terms of continuity equation and total residual at attachment line.



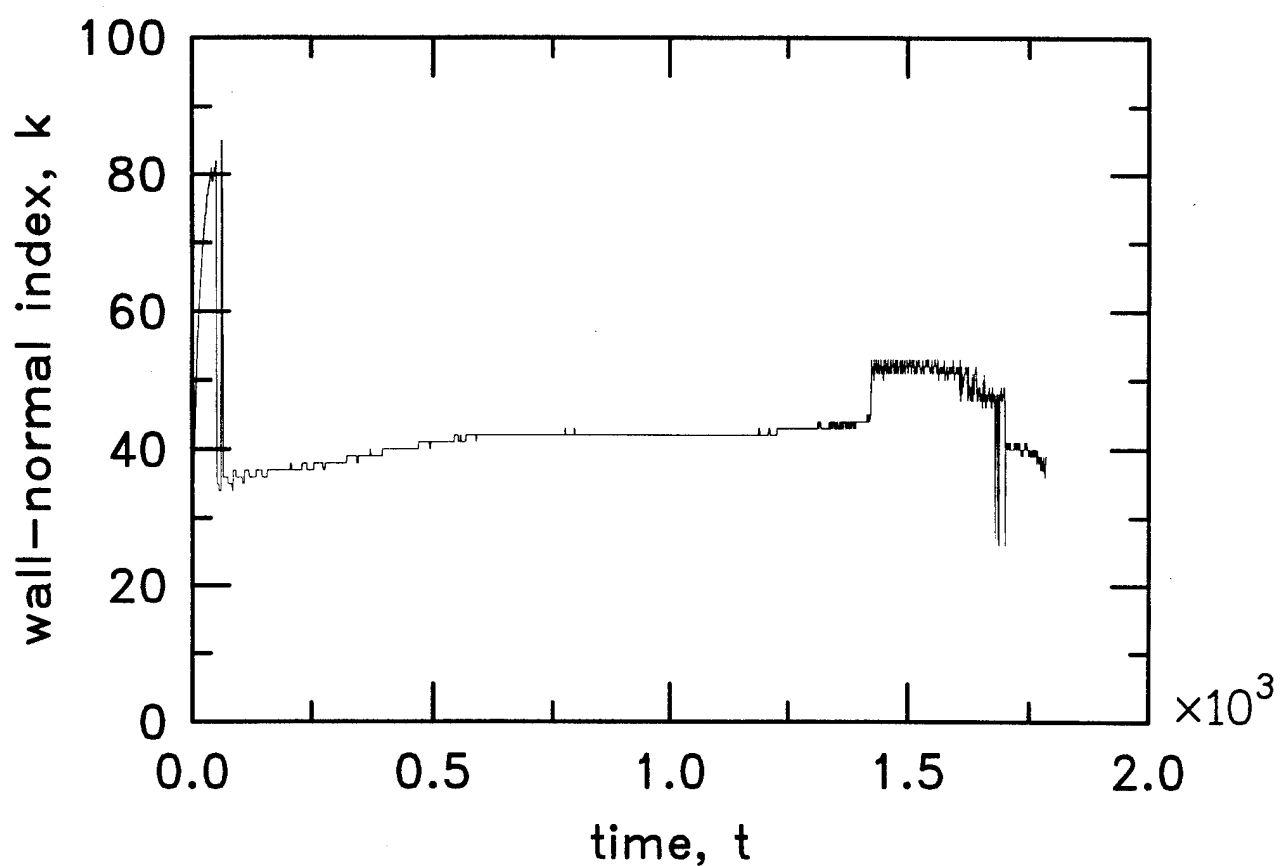
2. Individual terms of continuity equation and total residual at $x^* = 0.04$ ft.



3. Temporal evolution of global maximum residuals of time-independent compressible Navier-Stokes equations.

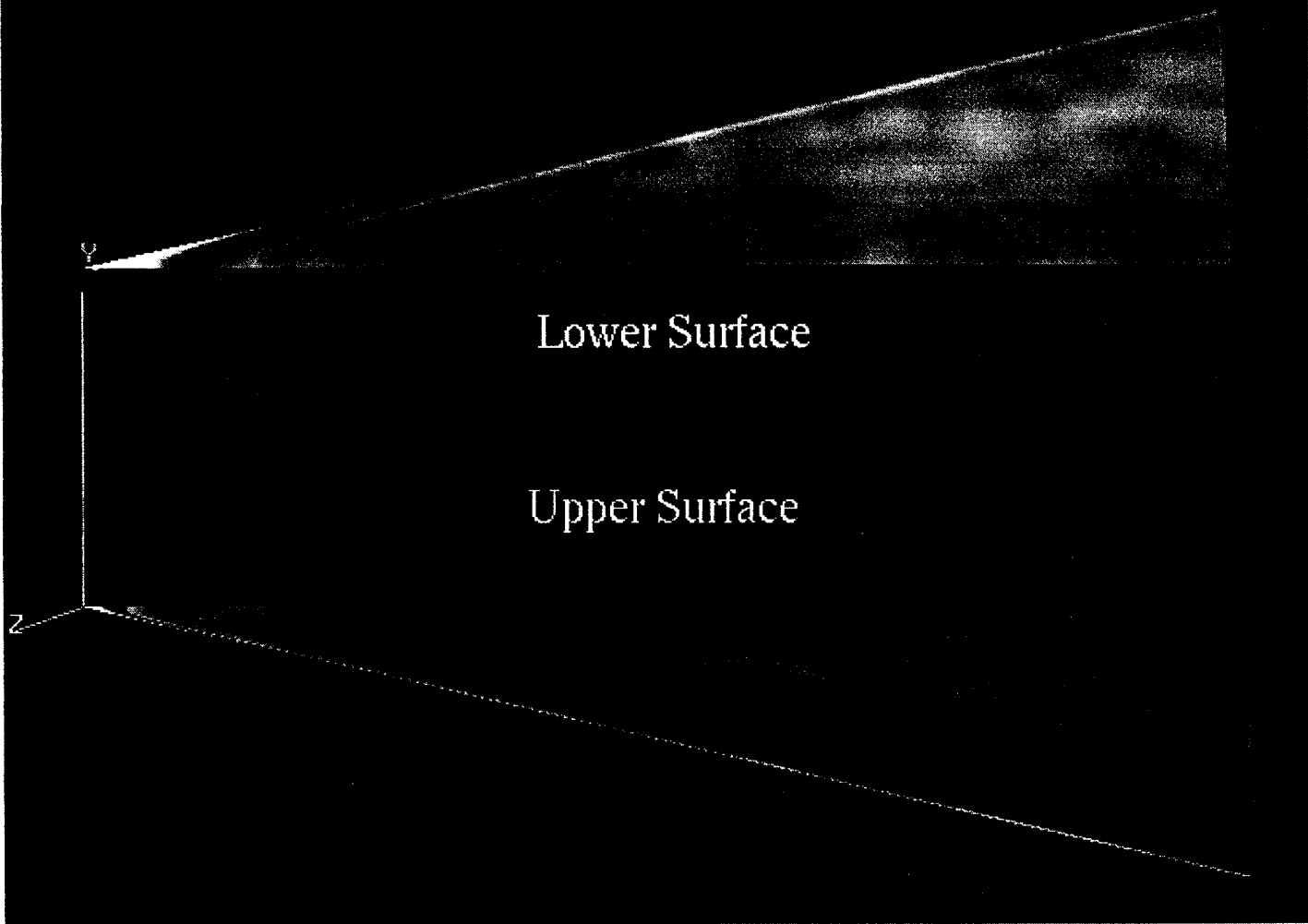


4. Streamwise index of global maximum residual versus time.

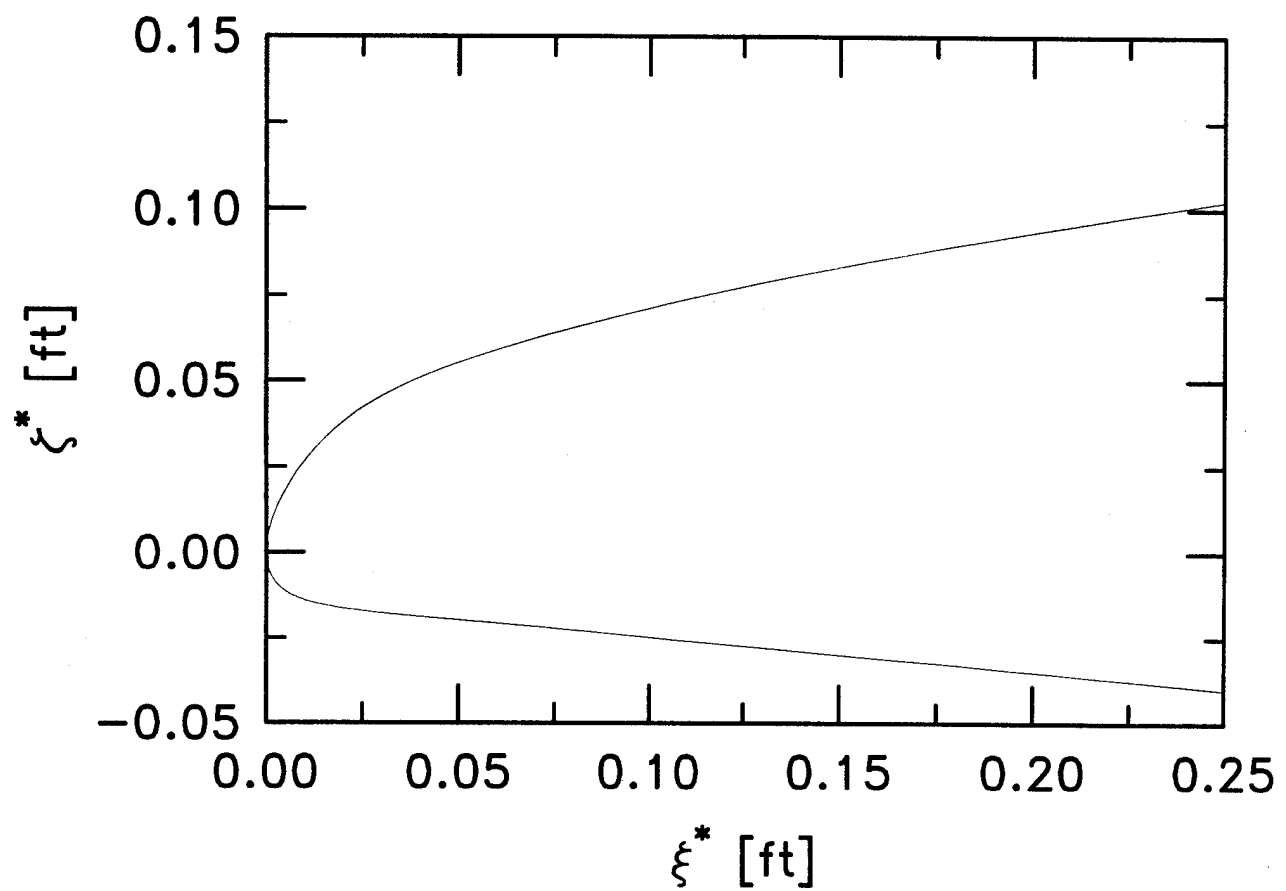


5. Wall-normal index of global maximum residual versus time.

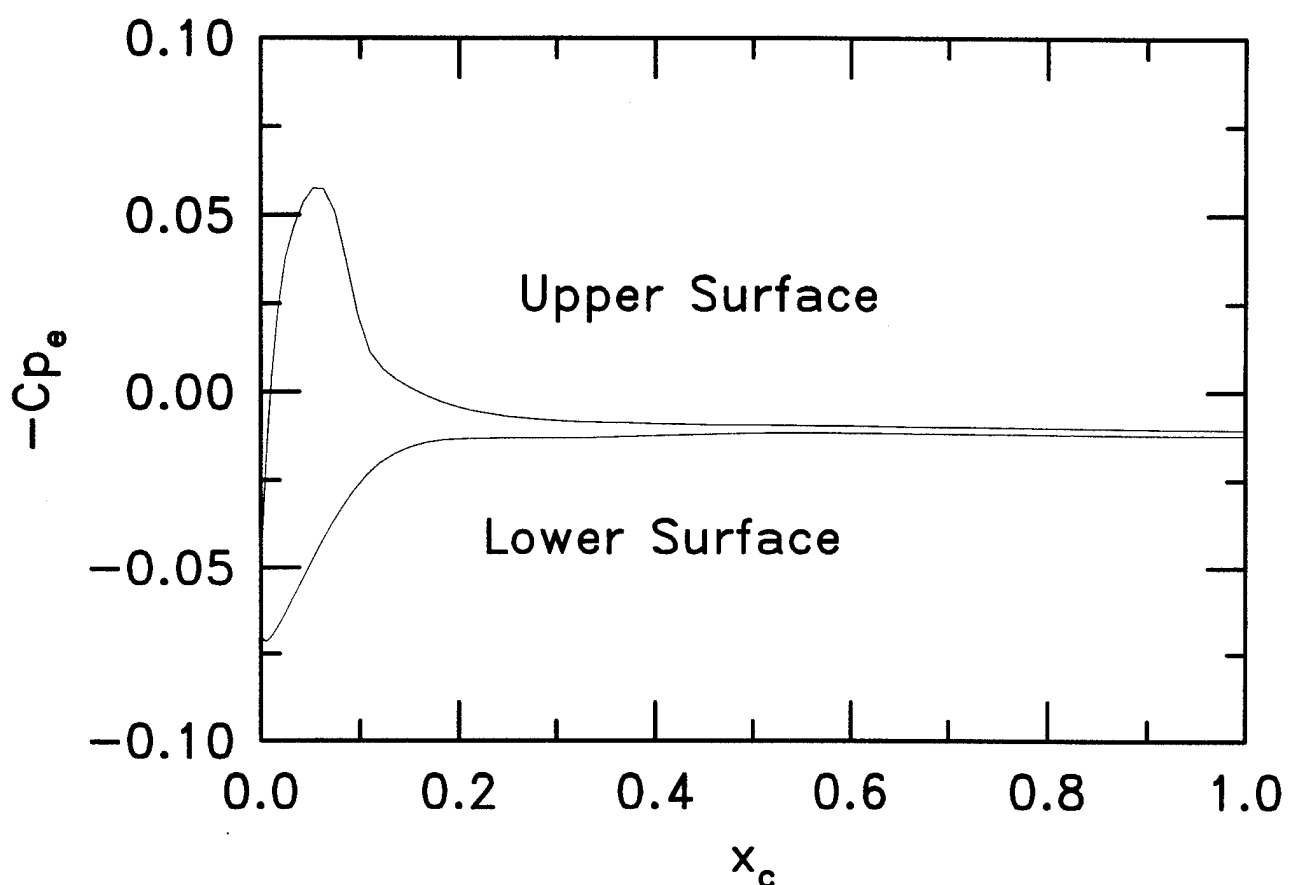
77-Degree Swept Wing in Mach 3.5 Flow Surface Pressure Coefficient



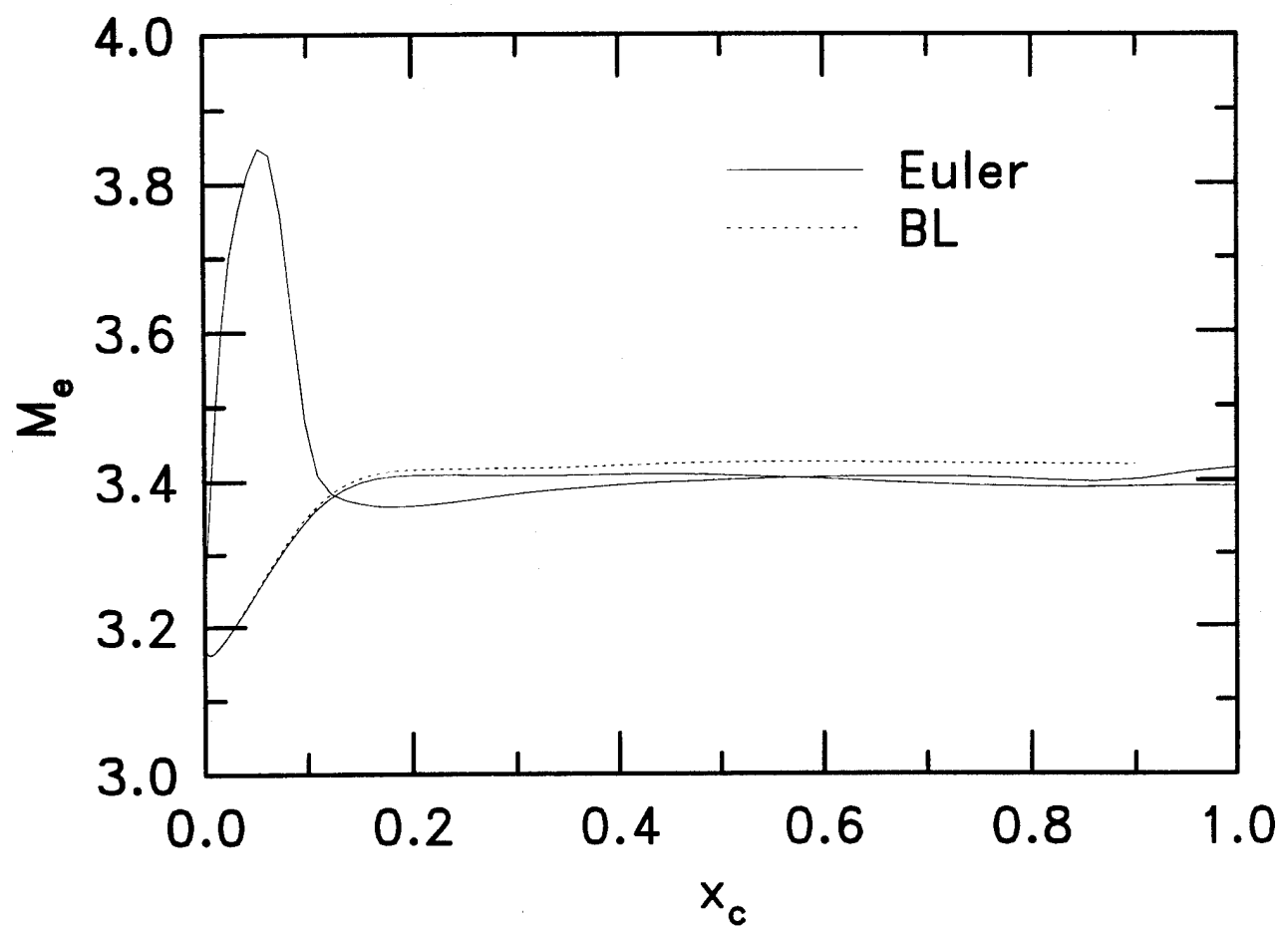
6. Euler solution displaying isobars of constant pressure on upper and lower surfaces of wing model of Cattafesta et al. [3]



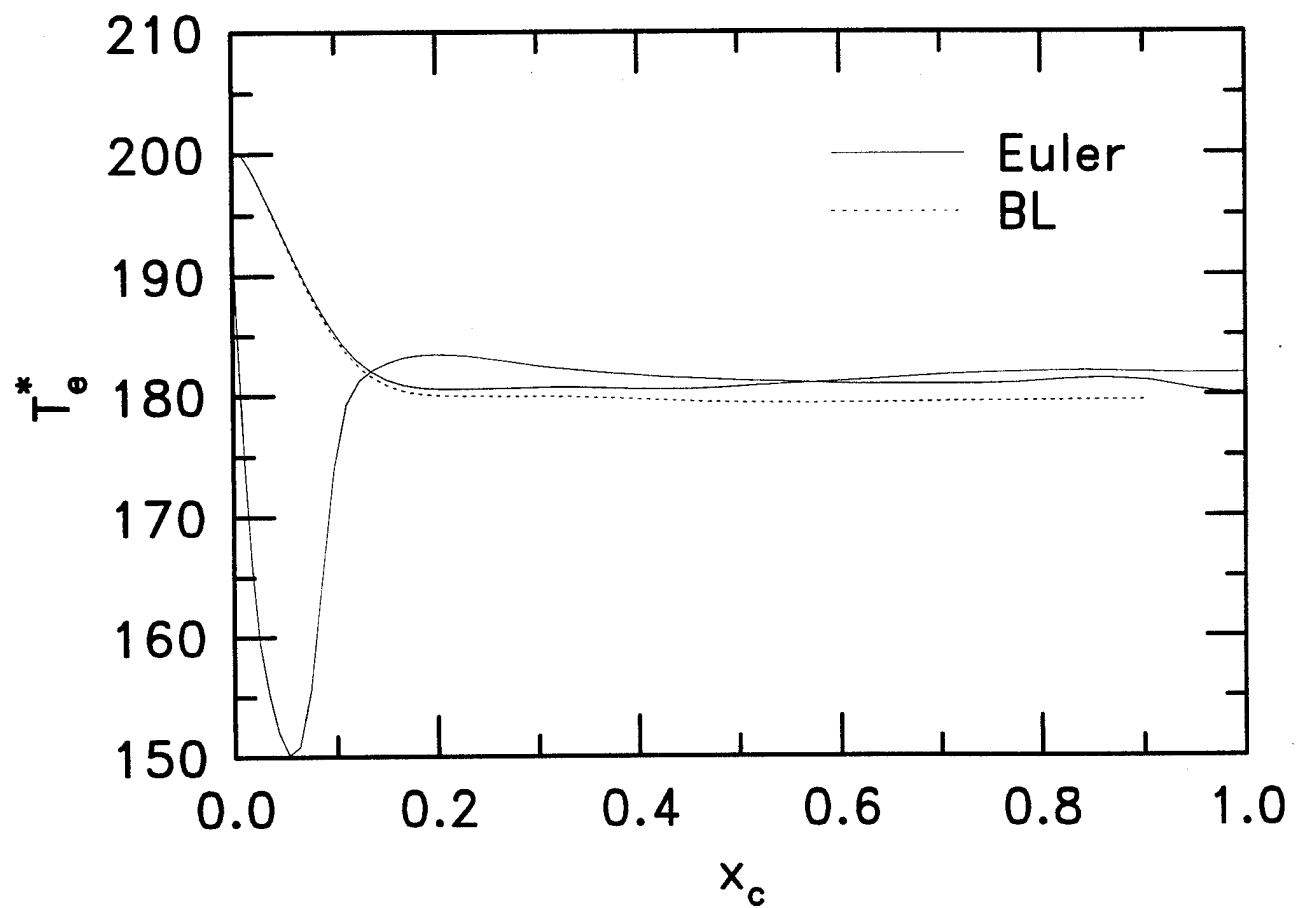
7. Wing section perpendicular to leading edge.



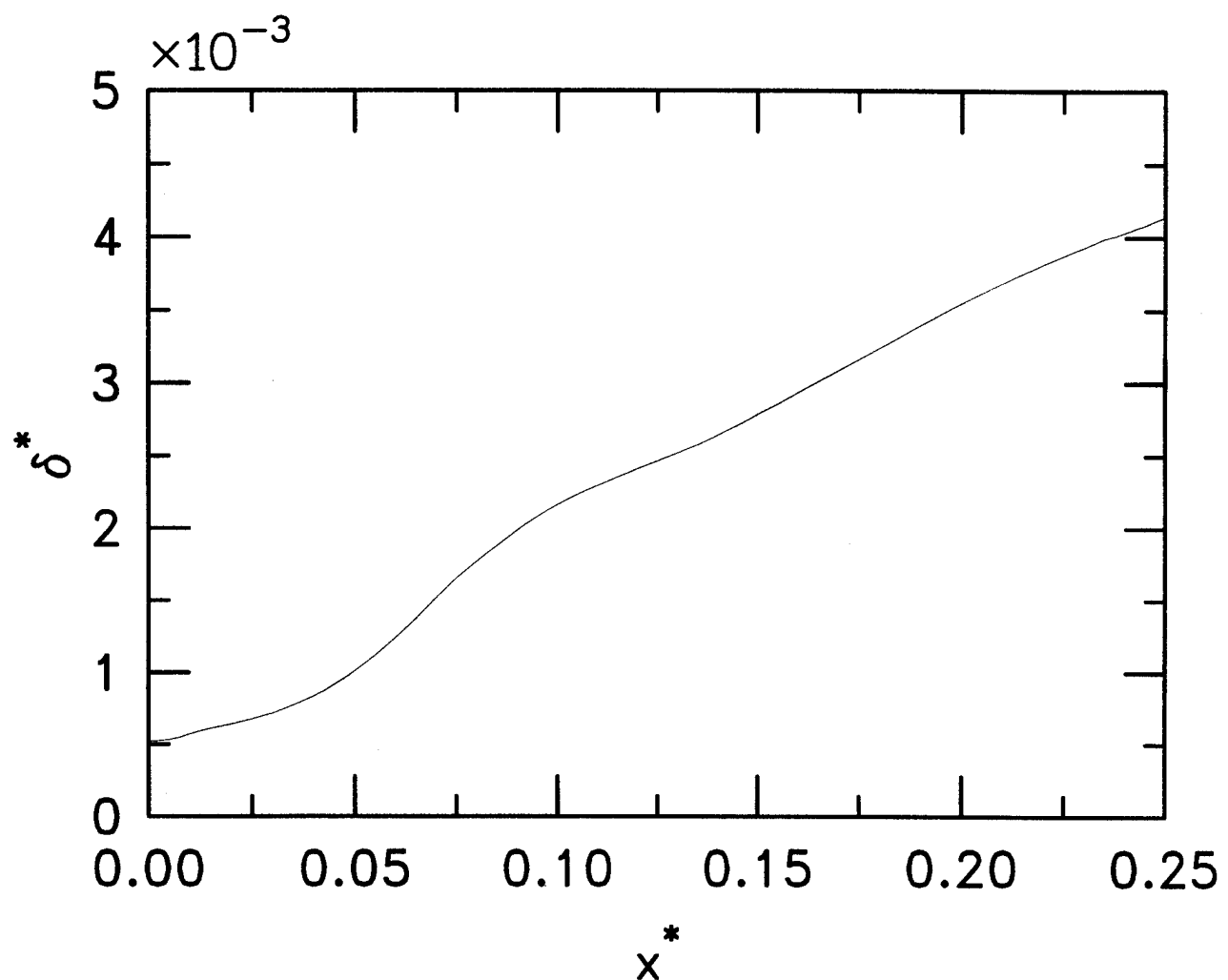
8. Surface pressure coefficients for wing section of Fig. 7.



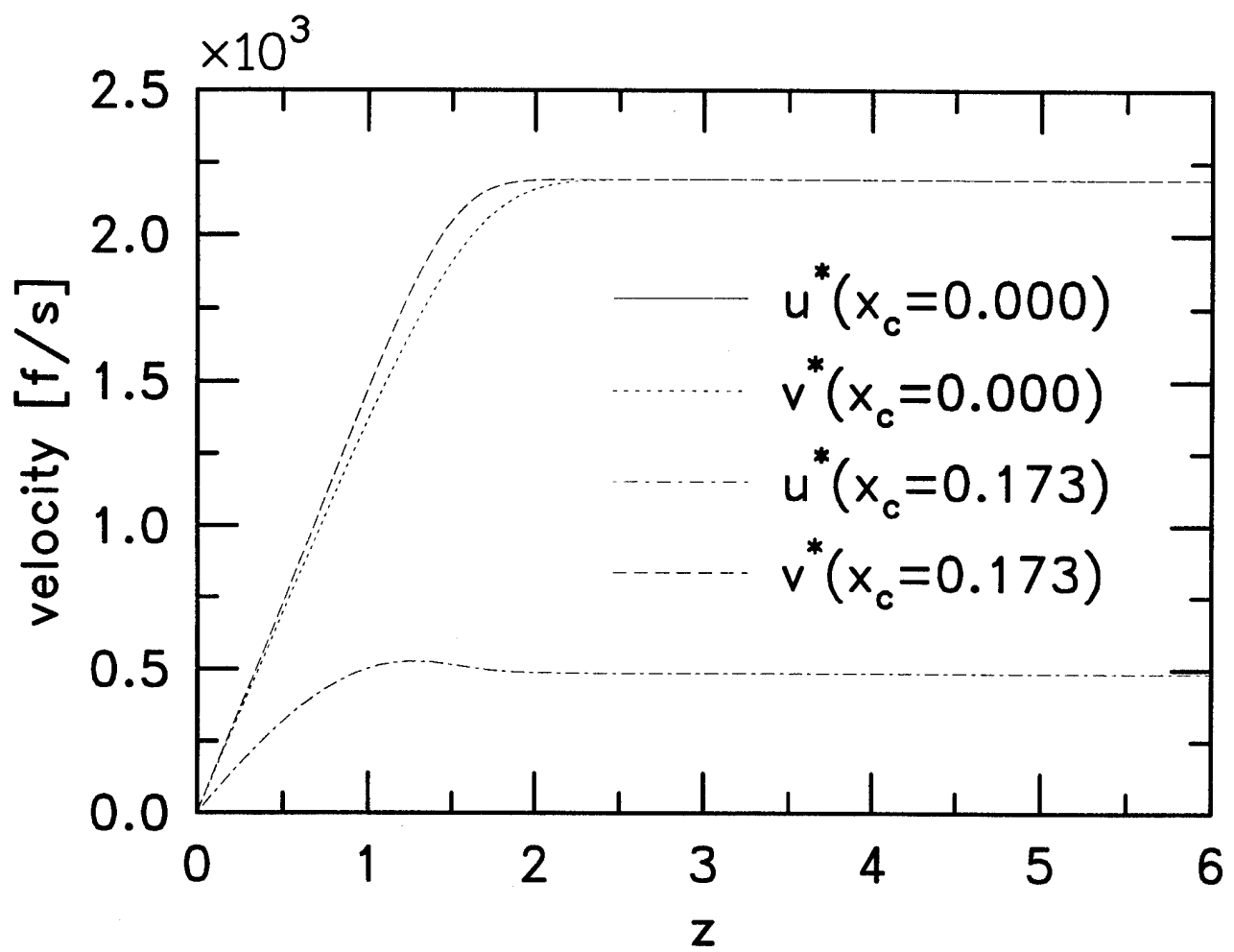
9. Edge Mach-number distribution for wing section of Fig. 7.



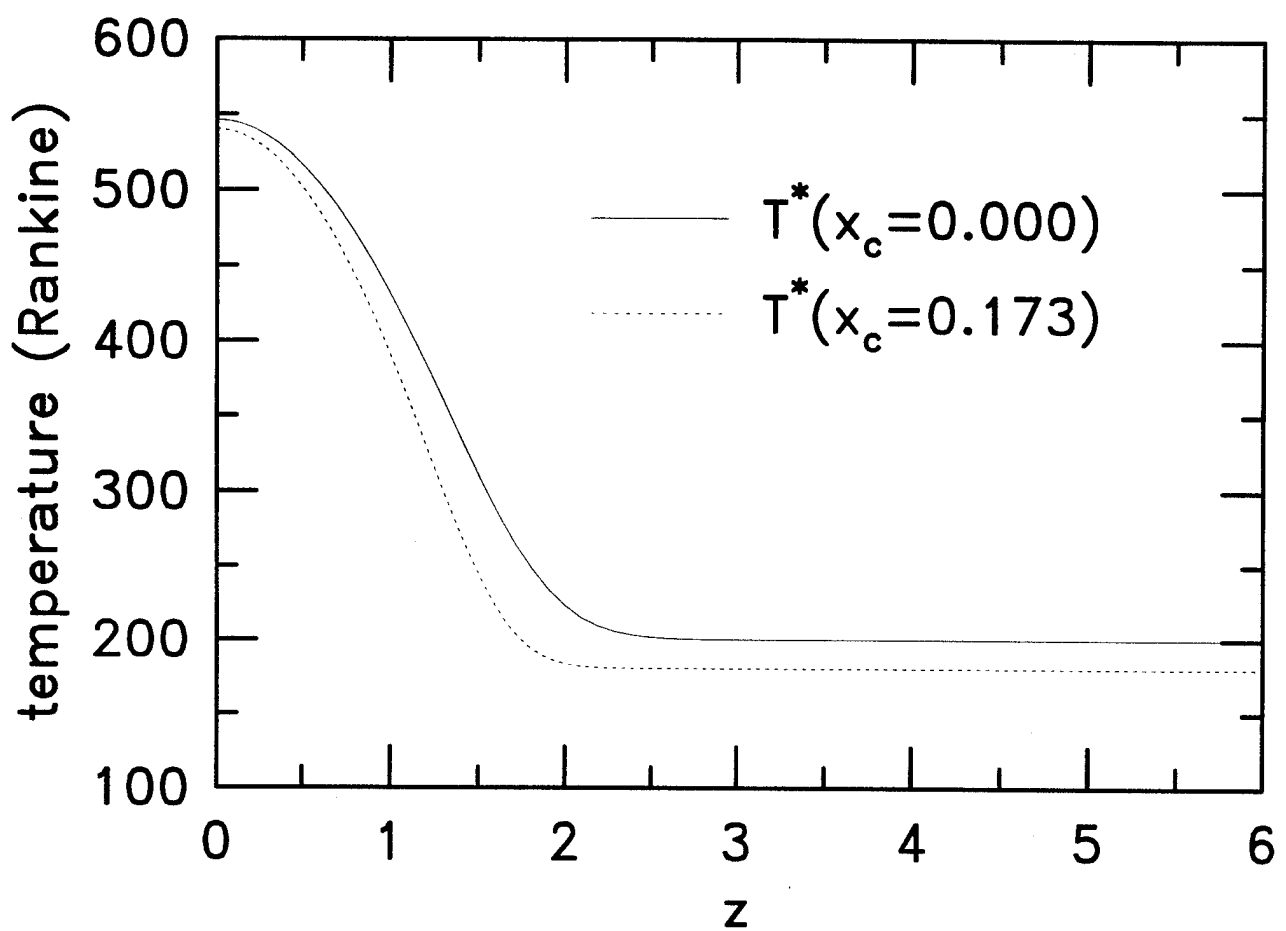
10. Edge temperature distribution for wing section of Fig. 7.



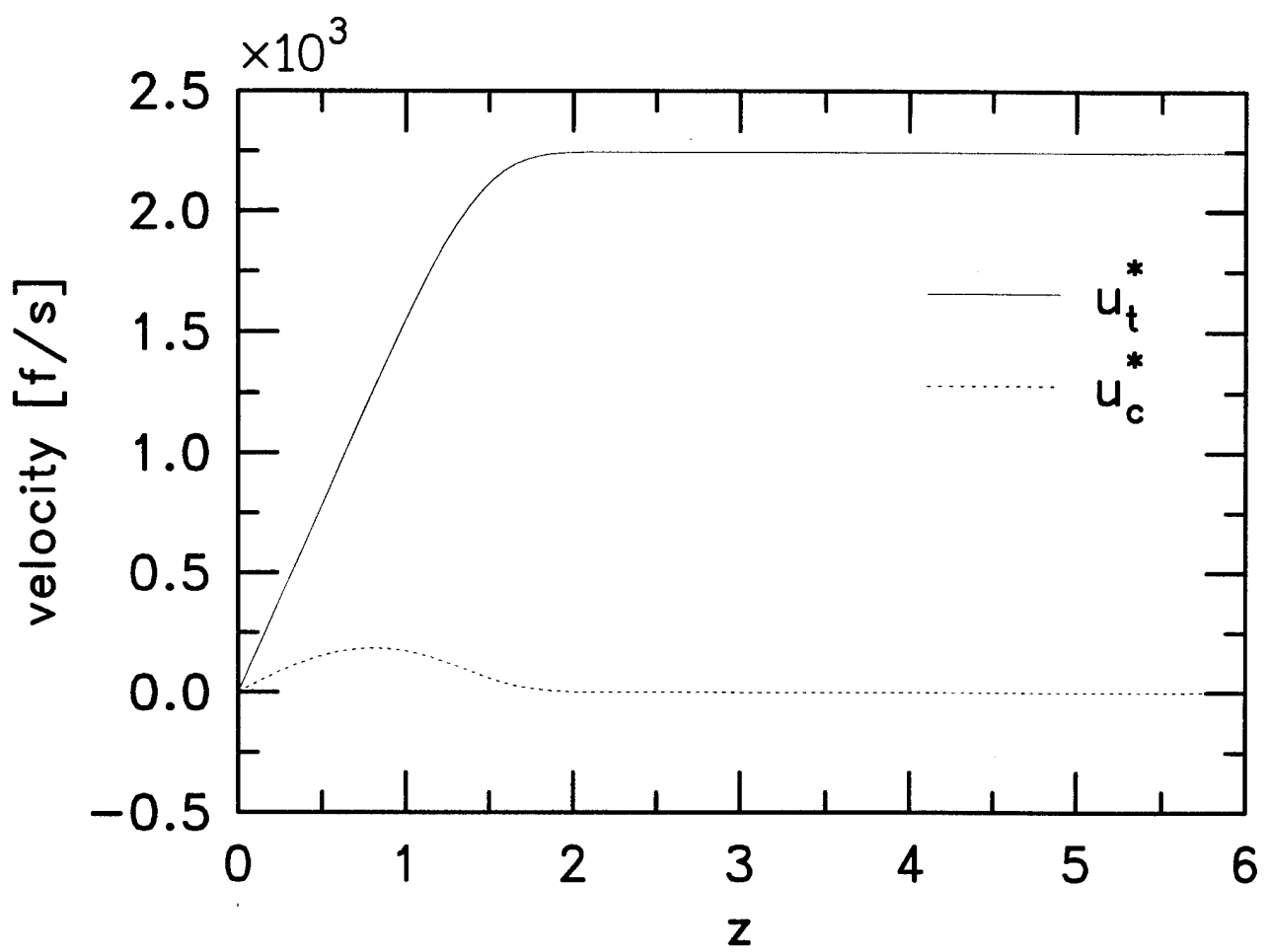
11. Evolution of boundary-layer displacement thickness on upper surface of wing section of Fig. 7.



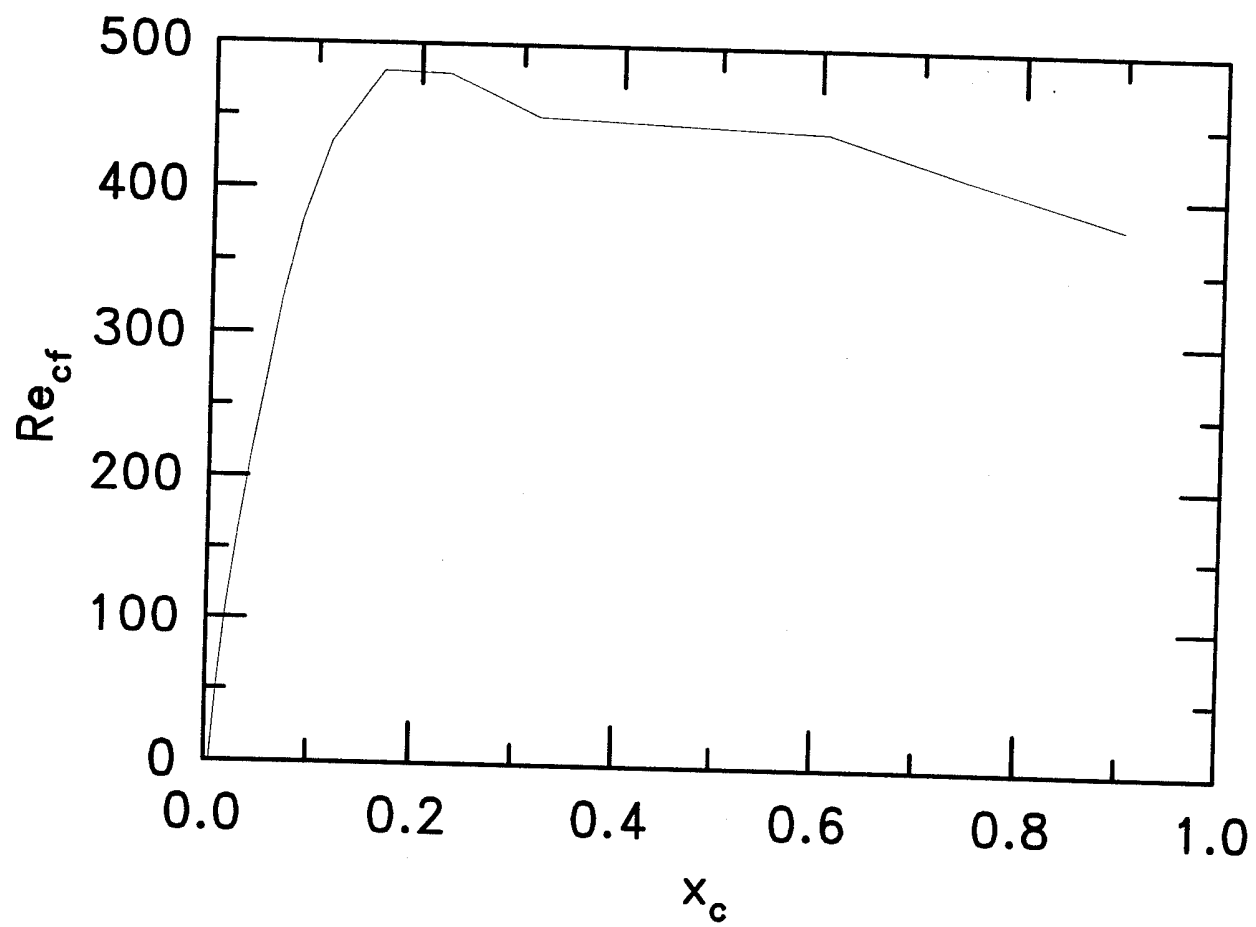
12. Wall-normal distributions of streamwise and spanwise velocities at attachment line and at $x_c = 0.173$ on upper wing surface.



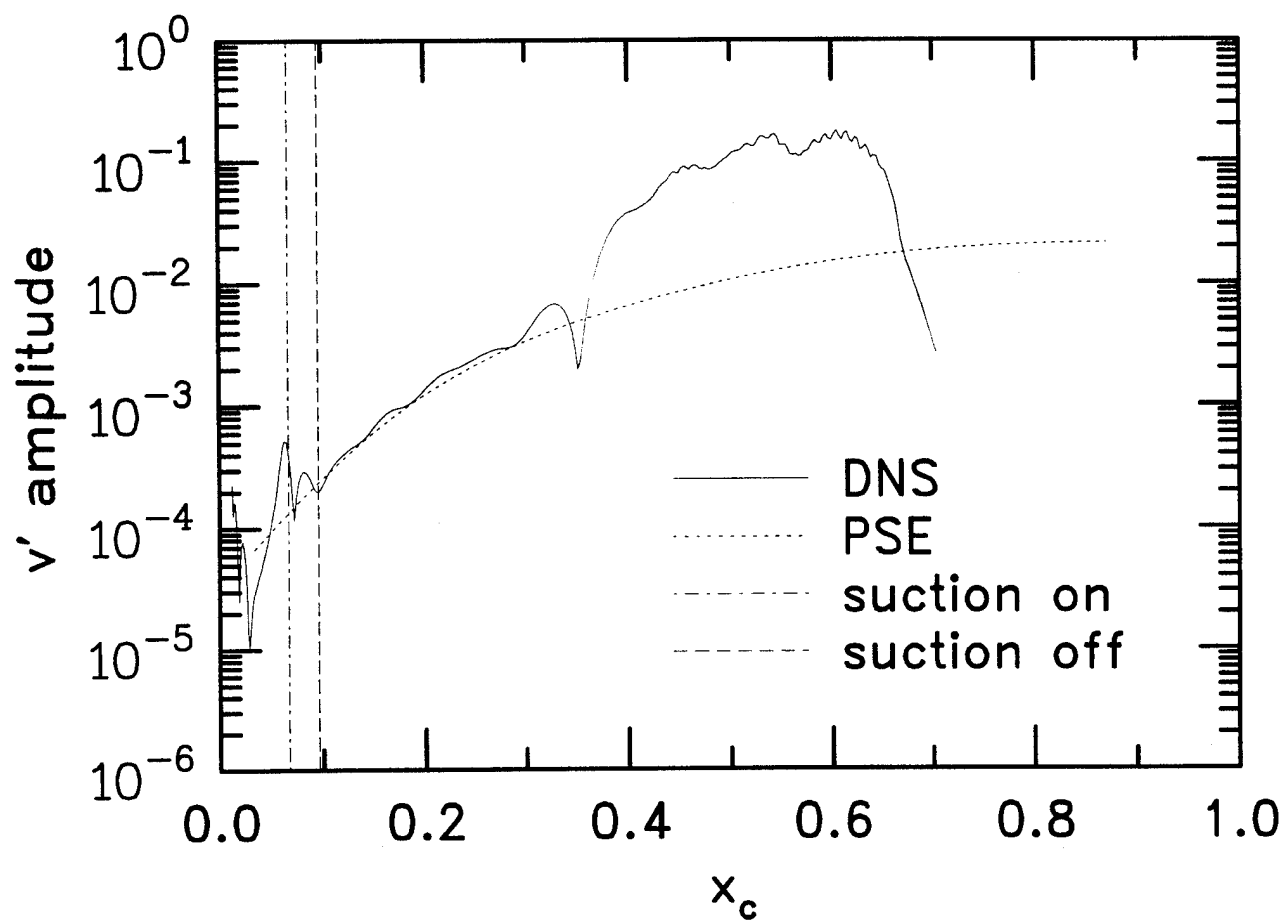
13. Wall-normal distribution of temperature at attachment line and at $x_c = 0.173$.



14. Comparison of tangential and crossflow velocities at $x_c = 0.173$ on upper wing surface.



15. Streamwise evolution of crossflow Reynolds number on upper wing surface.

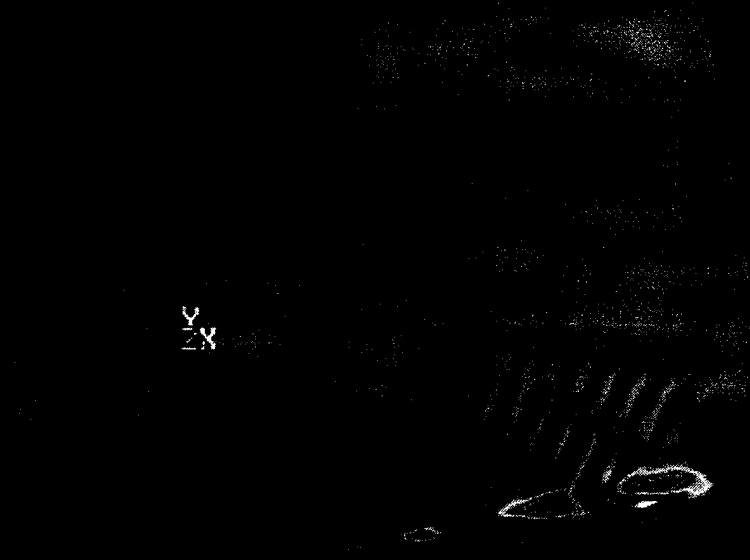


16. Streamwise evolution of maximum of fundamental of spanwise velocity perturbation.

77-Degree Swept Wing

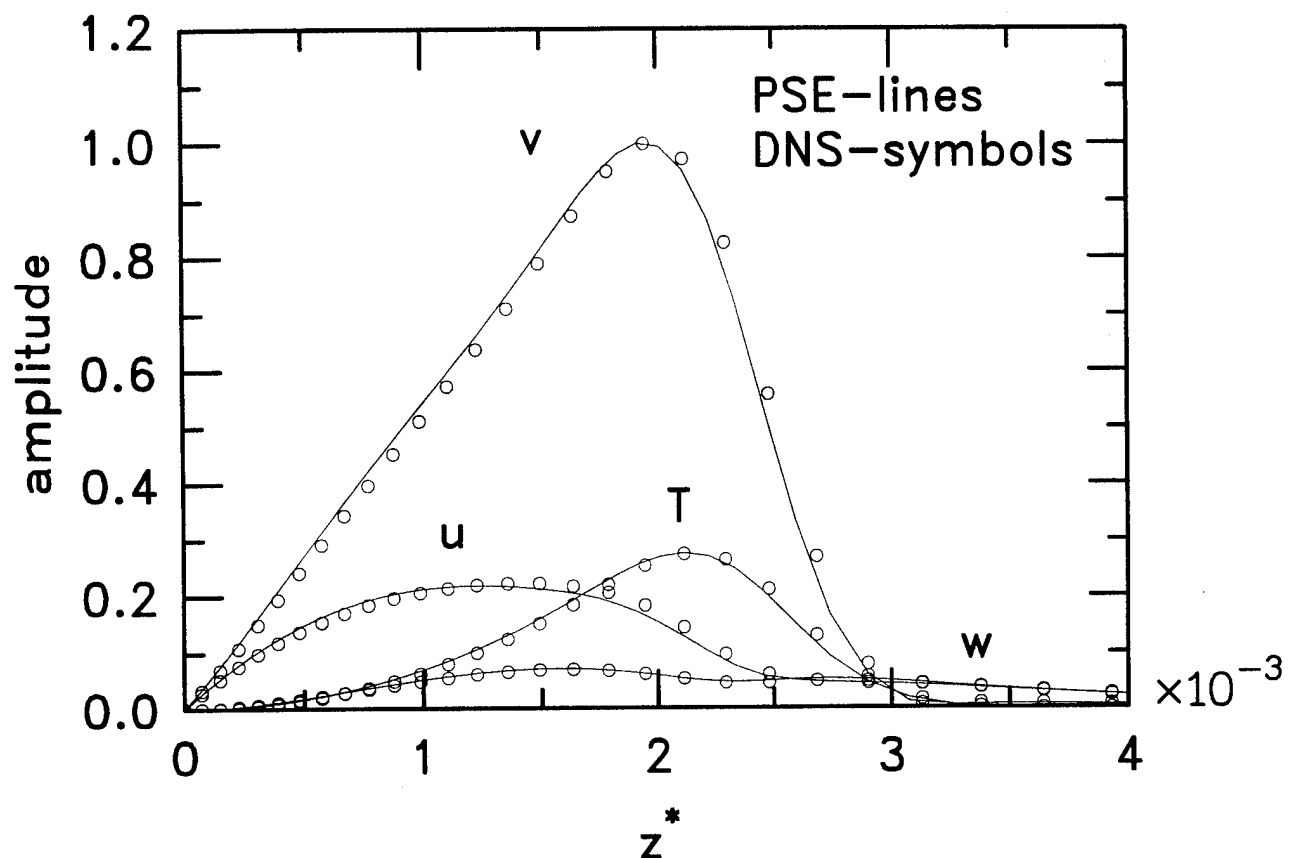
Mach 3.29

Disurbance Density

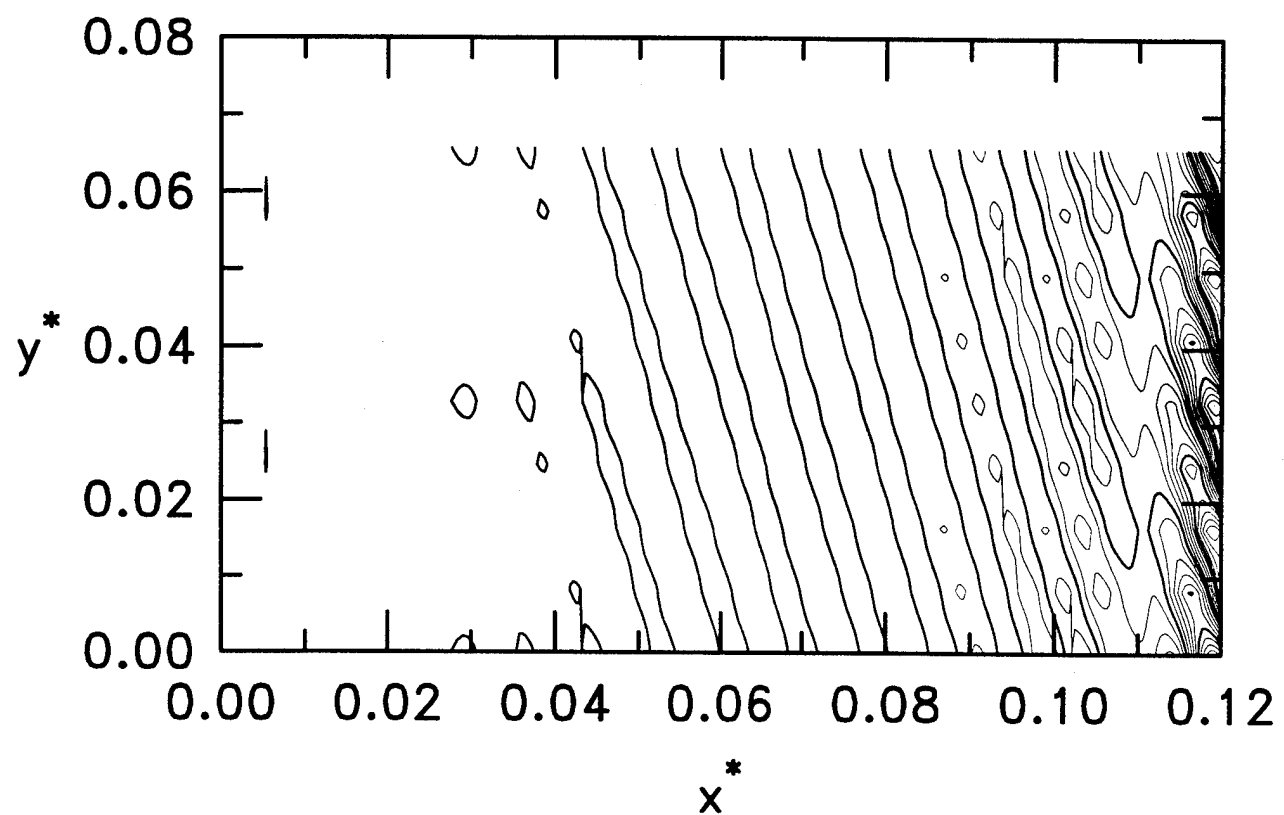


Acoustic Radiation
from Developing Wavefront

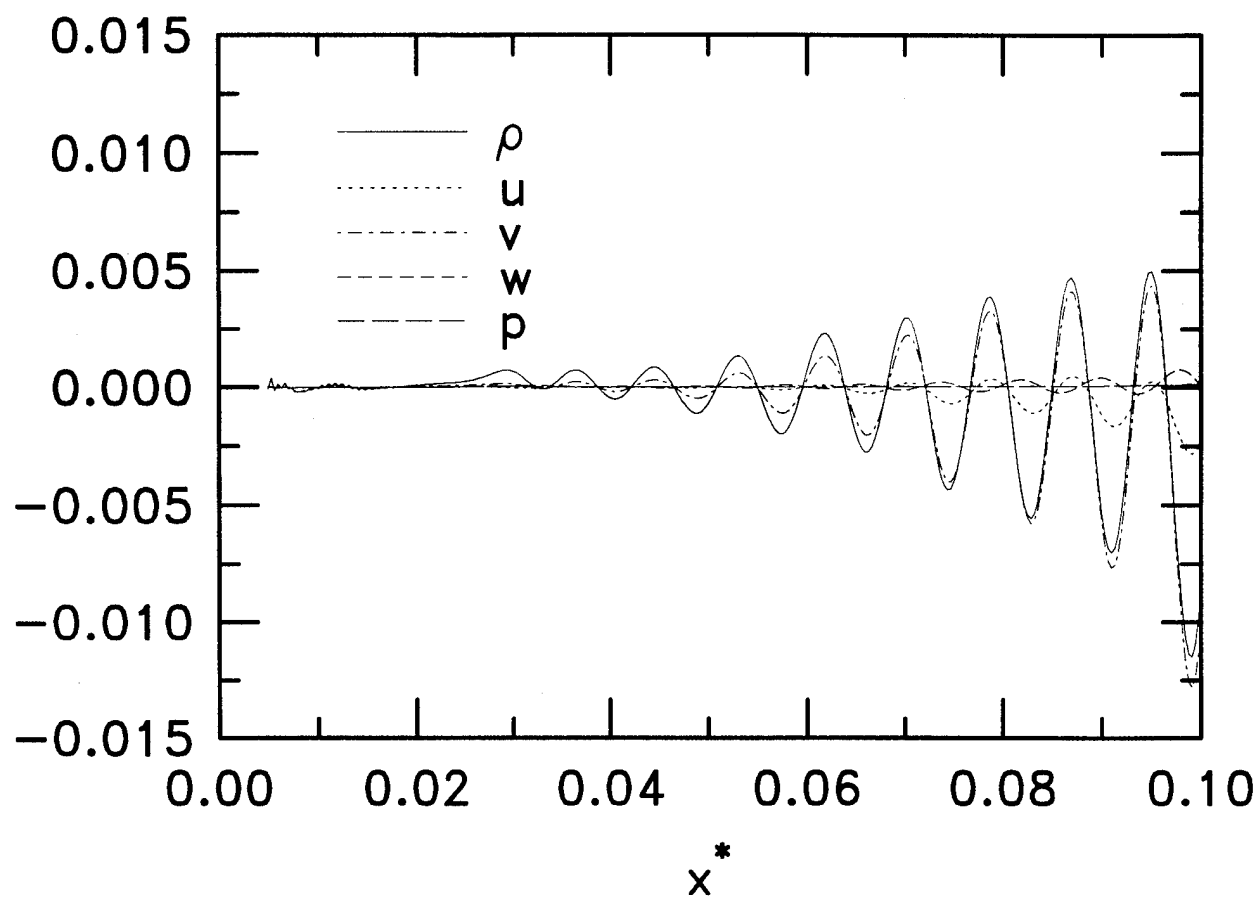
17. Contours of constant disturbance density in computational plane normal to both leading edge and wing surface showing acoustic energy generated by strong nonlinearity in wave-packet region.



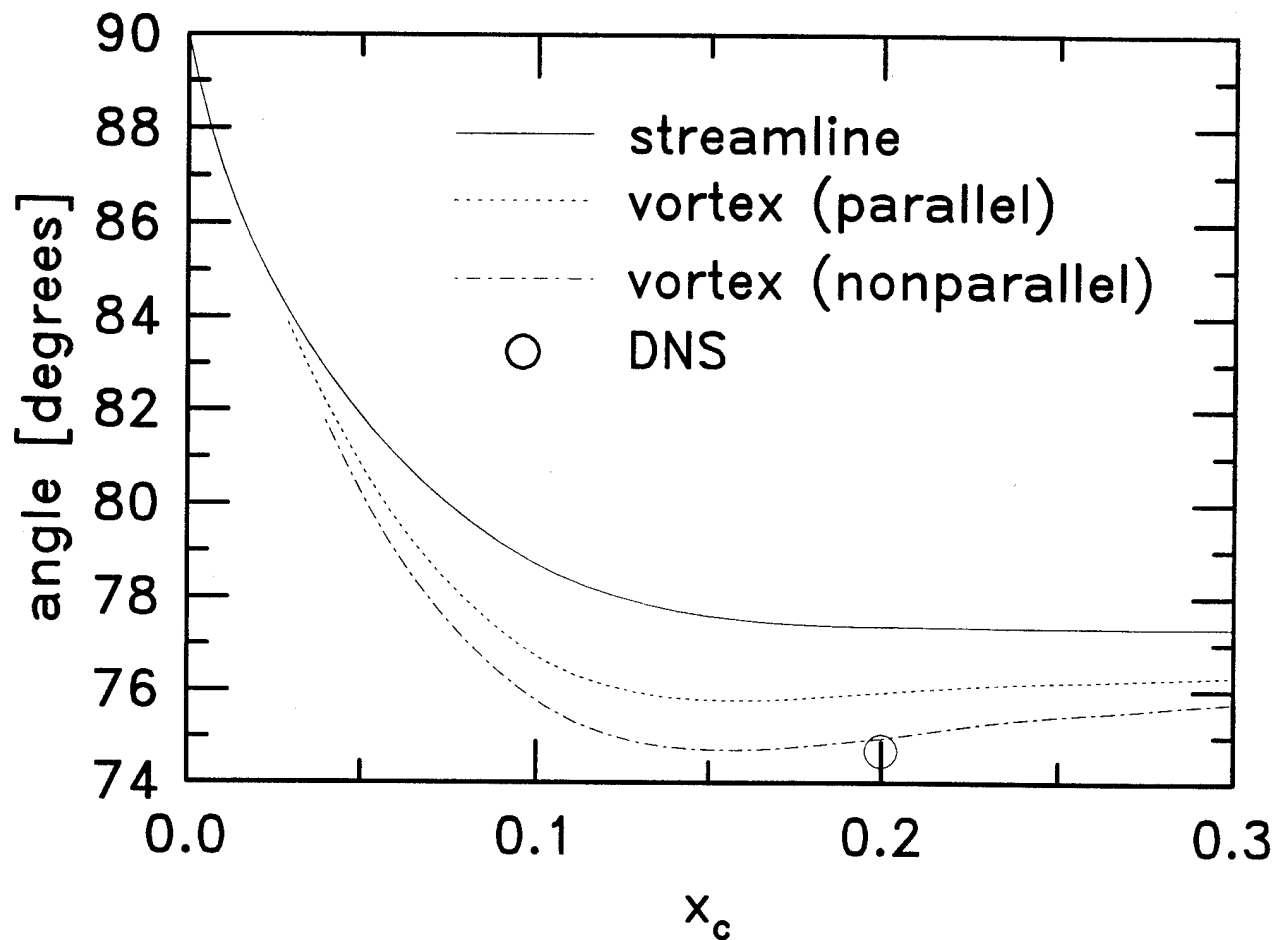
18. Comparison of amplitude distributions of components of fundamental spanwise Fourier component of DNS calculation with PSE-derived crossflow disturbance at $x_c = 0.22$. In each case, results are normalized so that maximum spanwise perturbation velocity is unity. (Even indexed DNS values omitted.)



19. Contours of constant perturbation density in surface approximately 1.5 displacement thicknesses from wall showing alignment of crossflow vortices. Computational domain is replicated once in span for aesthetics.



20. Projection of perturbation density field of Fig. 19 onto selected spanwise plane showing streamwise wavelength of dominant crossflow mode.



21. Comparison of vortex-alignment angle and inviscid-streamline angle relative to x -axis showing orientation of crossflow mode in direction of inviscid streamlines.